MULTI-COMPARTMENTAL MODELING OF HIV-1 CRYPTIC VIREMIA

by

Erwing Fabian Cardozo

A dissertation submitted to the Faculty of the University of Delaware in partial fulfillment of the requirements for the degree of Doctor of Philosophy in Electrical and Computer Engineering

Spring 2014

MULTI-COMPARTMENTAL MODELING OF HIV-1 CRYPTIC VIREMIA

by

Erwing Fabian Cardozo

Approved: _____
Kenneth E. Barner, Ph.D.
Chair of the Department of Electrical and Computer Engineering

Approved: _____
Babatunde A. Ogunnaike, Ph.D.
Dean of the College of Engineering

Approved: _____
James G. Richards, Ph.D.
Vice Provost for Graduate and Professional Education

I certify that I have read this dissertation and that in my opinion it meets the academic and professional standard required by the University as a dissertation for the degree of Doctor of Philosophy.

Signed: _____

Ryan M. Zurakowski, Ph.D.
Professor in charge of dissertation

I certify that I have read this dissertation and that in my opinion it meets the academic and professional standard required by the University as a dissertation for the degree of Doctor of Philosophy.

Signed: _____

Michael J. Piovoso, Ph.D.
Member of dissertation committee

I certify that I have read this dissertation and that in my opinion it meets the academic and professional standard required by the University as a dissertation for the degree of Doctor of Philosophy.

Signed: _____

Abhyudai Singh, Ph.D.
Member of dissertation committee

I certify that I have read this dissertation and that in my opinion it meets the academic and professional standard required by the University as a dissertation for the degree of Doctor of Philosophy.

Signed: _____

Mark Mirotznik, Ph.D.
Member of dissertation committee

I certify that I have read this dissertation and that in my opinion it meets the academic and professional standard required by the University as a dissertation for the degree of Doctor of Philosophy.

Signed: _____

Nii Attoh-Okine, Ph.D.
Member of dissertation committee

ACKNOWLEDGEMENTS

I first would like to thank God. I would not be here without His love and careful instructions.

I want to specially thank my amazing wife Brenda. I am very fortunate to have an adorable, loving and wise person at my side. She has made easier the most difficult times. I am also in immense debt to my parents Ines and Fernando for their selfless care and love. Despite the distance, they never ceased to encourage me. I am also very grateful to my brothers Jose and Mauricio, and my sister Nathalia for their love and support.

Also, I would like to thank my graduate advisor Dr. Ryan Zurakowski for be an outstanding mentor to me. He gave me the exceptional guidance and freedom to complete my research, such that I had to do no less than working hard to reach a proficiency level that he could rely on. I also would like to thank to my dissertation committee. Special thanks to Dr. Michael Piovoso for his careful insights and continuous encouragement in each stage of this process, also to Dr. Abhyudai Singh and Dr. Nii Atto-Okine for all the academic advice and support, and Dr. Mark Mirotznik for all the remarkable comments and suggestions to my work.

Finally, I would like to thank all my friends and my colleagues in Dr. Zurakowskis lab and. Specially, I want to thank Cesar, Sergio, Irene, Claudia, Hoover and Laura for all the support and inspiration all these years.

TABLE OF CONTENTS

LIST OF TABLES

LIST OF FIGURES

ABSTRACT

Combination Antiretroviral Therapy (cART) can suppress plasma HIV below the limit of detection in normal assays. Recently reported results suggest that viral replication may continue in some patients, despite undetectable levels in the blood. It is broadly reported that latently infected cells are the main cause of this persistence under cART. It has been suggested that the appearance of the circularized episomal HIV DNA artifact 2-LTR, following treatment intensification with the integrase inhibitor raltegravir, is a marker of ongoing viral replication. These 2-LTR episomes are assumed to be formed from the virus DNA copies that could not be integrated in the DNA of the CD4+ T Cells caused by raltegravir. Other work has suggested that lymphoid organs may be a site of reduced antiviral penetration and increased viral production. Given the fact that raltegravir does not affect viral load in peripheral blood, the main hypothesis of viral persistence through ongoing replication is that the process is happening in anatomical reservoirs related to poor penetration of reverse transcriptase and protease inhibitors.

This thesis proposes a mathematical model to investigate whether lymph nodes can function as sanctuary sites for ongoing viral replication and investigates the patterns of 2-LTR formation expected after raltegravir application, incorporating spatial dynamics to previous models. It also describes the mechanisms by which this could be possible, and the conditions needed to generate the transient behavior of both measured 2-LTR and HIV viremia in the blood after administering raltegravir in patients on apparently suppressive cART regimens as shown in recent studies. A multi-compartmental differential equation is described taking into account the dynamics of infected and uninfected CD4+ T cells, free virus, and cells containing 2-LTR circles. The sanctuary site is modeled with limited penetration of the antiviral drugs.

Experimental data and previously published distributions are used to estimate the reaction and diffusion parameters and HIV and T-cells rates in a Monte-Carlo simulation of the model to determine what parameter values are consistent with the observed 2-LTR transient behavior. This thesis analyzes the effect of different suboptimal penetration of drug in cART, the anatomical reservoir size on cryptic viremia for hyperplastic follicles inside lymph nodes and its possible effect in the formation of viral blips and 2-LTR circles in the blood. Using previous 2-LTR circles data, this thesis presents how these conditions have to be meet in order to have 2-LTR formation in PBMC. Furthermore, through a Bayesian MCMC analysis this thesis aims to find how much T cells recirculation time could affect previous estimation of 2-LTR circles half-life. Based on that, it finally presents that measurable 2-LTR peaks might be correlated to total infection in the body, but with different patterns of drug penetration combinations and reservoir size for each peak.

Chapter 1

INTRODUCTION

1.1 Human Immunodeficiency Virus

Human Immunodeficiency Virus (HIV) is a roughly spherical retrovirus that infects CD4+ T cells, causing acquired immunodeficiency syndrome (AIDS). AIDS is characterized by the breakdown of the adaptive immune system, leading the patient vulnerable to opportunistic infections. The adaptive immune system is a complex and self-regulated network of specialized cells with the aim to protect the human body from foreign agents (antigens). HIV infects and decreases the number of CD4+ T cells, a crucial set of cells in the adaptive immune system, leading to failure in the immune response.

CD4+ 'helper' T cells are a class of T cells that express the surface molecule CD4. These cells, after they migrate from the thymus, interact with antigen presenting cells with information of foreign agents. If an antigen is detected, CD4+ T cells are activated promoting immune response.

HIV has an envelope with high affinity with the CD4 surface molecule in the helper T cell. Inside the envelope, the virus has two identical RNA strands, enclosed in a protein capsid. These RNA copies encode the necessary information for the production of enzymes, structural and regulatory proteins facilitating the replication of the virus.

After the virus successfully binds to the cellular membrane, the HIV RNA strands are released into the cell. When the viral genome enters into the cell, four general steps occur as presented in figure 1.1: (1) The reverse transcriptase protein copies from the RNA strands to make a complementary DNA (cDNA). (2) This cDNA

is translocated into the nucleus of the cell and integrated into the host cell genome. (3) After that, the virus uses the protein machinery of the cell to produce new viral RNA transcripts which are transported to the cytoplasm to produce new viral proteins, that (4), leads to the assembly and production of many new virions. Given that this infection process takes advantage of the T cell machinery, it degrades the host cell leading it into a half-life of around 1 day. Thus, the number of CD4+ T cells decays rapidly producing chronic immunodeficiency, and, if no treatment, death.

1.2 Combined Antiretroviral Therapy

Very early, individual drug treatment inhibiting one of the HIV life-cycle steps, starts a fight against HIV infection. However, studies found that HIV has a rapid turnover and high mutation rate, producing a higher diverse population of the virus than previously thought. This diversity increases significantly the likelihood of resistance to any one-drug antiviral treatment, forcing a multi-drug treatment as the modern strategy used to control HIV infection. This treatment called combined antiretroviral therapy (cART) employs a cocktail of three or more drugs designed to interfere with various different steps in the HIV life cycle [52, 77]. Currently recommended cART consists of three drug regimen inhibiting reverse transcription and virus production as depicted in figure (1.1). The regimen includes either two nucleoside/nucleotide analog reverse transcriptase inhibitor (NTRI) and one non-nucleoside/nucleotide analog reverse transcriptase inhibitor (NNTRI), or two nucleoside/nucleotide analog reverse transcriptase inhibitor (NTRI) and one protease inhibitor (PI) [77]. This approach has been successful in the sense that it has transformed HIV infection from a death sentence to a manageable disease.

Using a multiple drug regimen increases the mutational barrier to escape while suppressing the overall virus replication rate. Multiple mutations are necessary to confer resistance to the drugs, making it extremely unlikely for resistant viruses to be generated by random chance. Despite this great advance in the treatment, cART cannot eliminate the virus. As figure 1.2 depicts, residual virus is being detected by

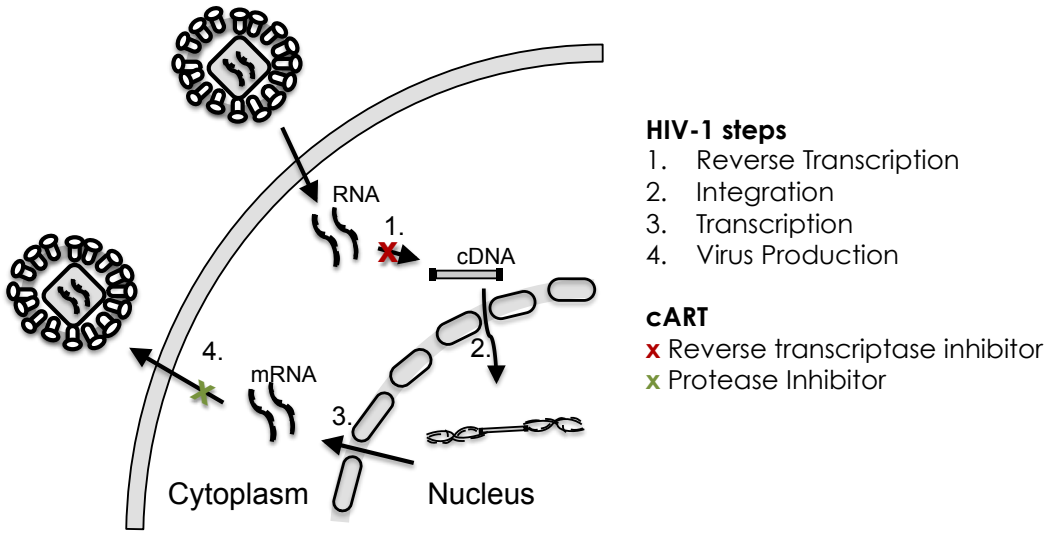

Figure 1.1: HIV-1 replication cycle and cART. Representation of HIV-1 infection of a T cell in four general steps, and how cART can inhibit them.

ultra-sensitive viral load assays [26], in patients under cART, with even intermittent episodes of transient viremia ('viral blips') in some patients. Thus, rapid viral rebound is experienced in patients when treatment is interrupted. [33].

1.3 Ongoing Replication and 2-LTR Formation

Reactivation of viral reservoirs in latently infected CD4+ T cells is the main source of HIV-1 persistence in patients under cART [29, 81, 17, 30]. However, the existence of *de novo* infection of active T-cells during suppressive therapy has recently been suggested as another possible source of residual viremia [16, 73, 11, 30]. Such ongoing replication would occur in anatomical reservoirs, possibly inside the lymph nodes [45, 67, 30], where there is evidence of poor antiviral penetration and resulting in viral replication [35, 72, 34].

Potential evidence of ongoing replication in remote compartments is the presence in peripheral blood of circular episomal HIV DNA artifacts, which are formed during failed viral infection events [73, 11, 72]. Because these circles contain a unique

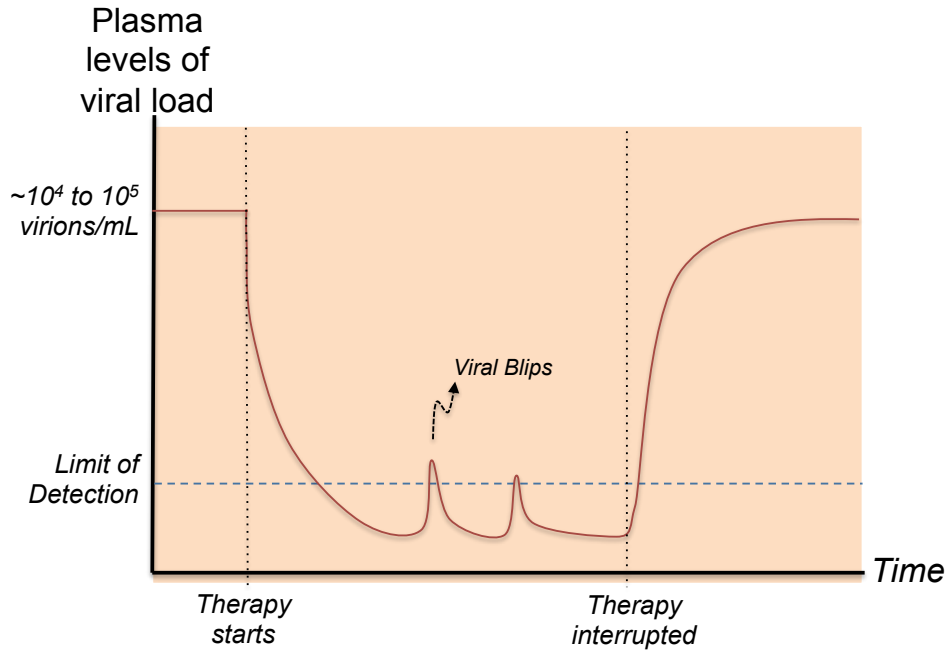

Figure 1.2: HIV-1 persistence. After initiation, cART suppresses plasma viral load below the limit of detection. However, the virus persists, and viral blips can be present in some patients. With very few exceptions, after cART is interrupted, all patients present viral rebound.

region with two adjacent copies of the viral long-terminal repeat (LTR), the boundary region of the HIV genome, they are known as 2-LTR circles. These 2-LTR circles are formed when host cell DNA repair enzymes modify linear viral cDNA that has failed to integrate into the host cell DNA. In the study by Buzon et al., 29% of the apparently fully-suppressed HIV-positive patients on cART were observed to have transient increases in CD4+ T cells containing HIV 2-LTR following intensification with raltegravir (RAL), the first integrase inhibitor to receive FDA approval. In the study, they enrolled HIV seropositive patients on suppressive cART for around 1 year. From them 45 were separated to continue cART with raltegravir (see figure 1.3). 2-LTR circles were detected in 13 of the 45 patients. Given that raltegravir specifically prevents the integration of linear viral cDNA in targeting cells, and that linear cDNA is a product of

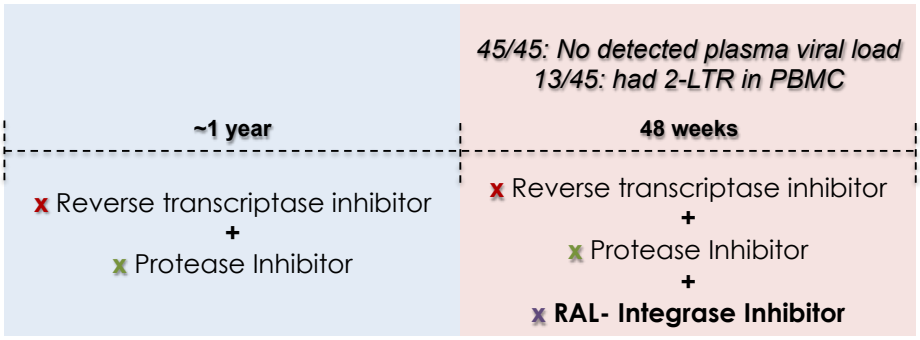

Figure 1.3: Buzon's study design. In the study, after 1 year under cART, the treatment in 45 patients was intensified with RAL and measurements were made for 48 weeks. In every patient, plasma viral load was below the limit of detection. However, in 13 of them, a transient behavior of 2-LTR circles in blood was found.

a recent infection event (see figure 1.4), this evidence strongly supports the hypothesis that the episomal HIV-1 genomes are biomarkers of recent virus replication [11, 72, 71].

In support of this hypothesis, a genotypic study, compared episomal DNA with proviral DNA in longitudinal samples per million of blood mononuclear cells (PBMC) from patients under raltegravir intensification of cART. The study showed marked differences between the viral genetical profiles, suggesting that episomal and proviral sequences came from different anatomical compartments [10]. A similar study, analyzing the envelope regions from episomes and proviruses in PBMC during cART interruptions, reports genetic similarities between rebounding virus and the episomes. However, the rebounding virions were different relative to the proviruses in the experiment, suggesting that the virus may rebound from anatomical reservoirs [72]. This evidence strongly supports 2-LTR circles as surrogates of recent viral replication in anatomical compartments.

1.4 Mathematical Model of 2-LTR Formation

Previously, a reduced model was proposed for the formation of 2-LTR in [47] with excellent fit to the data described in the Buzon study [11]. The model defines

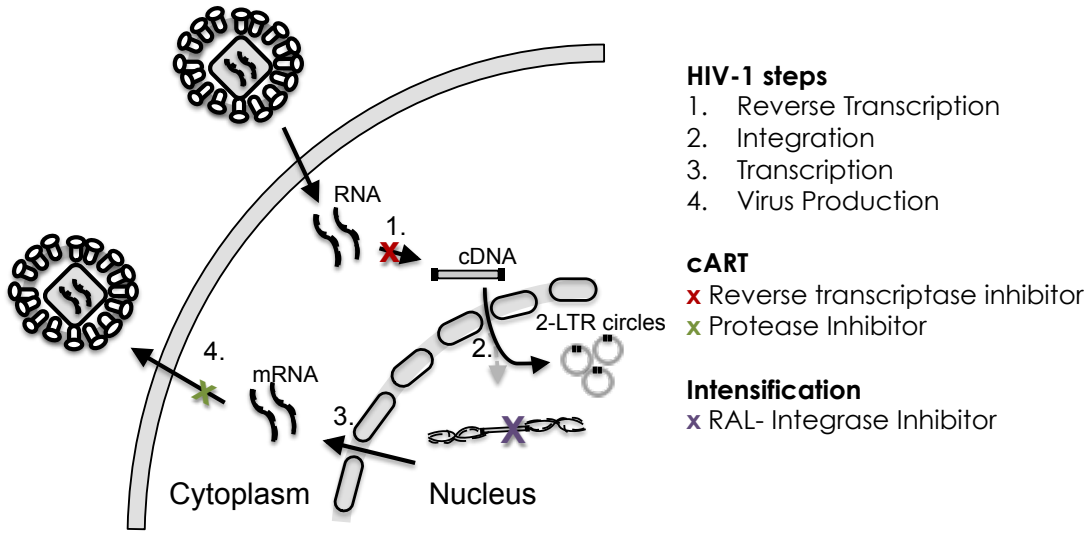

Figure 1.4: RAL intensification and 2-LTR formation. When raltegravir is applied in patients under treatment, 2-LTR circles can be only formed if RAL inhibit the integration of a recent de-novo infection of a T-cell by the virus.

the dynamics of active infected T cells $\mathbf{y}$ and 2-LTR containing cells $\mathbf{c}$ in the absence and presence of raltegravir (RAL). The model considers two sources for active cells, de novo replication events $aR\mathbf{y}$ affected by raltegravir $\eta_{II}\mathbf{u_{II}}$ and the activation of long-lived infected cells $\mathbf{y}_e$. On the other hand, the formation of 2-LTR is presented as proportional to the infection rate $aR\mathbf{y}$ but with different rates prior to raltegravir $\phi k_{II}(1-\eta_{II}\mathbf{u_{II}})$ and when raltegravir is applied $k_{II}\eta_{II}\mathbf{u_{II}}$. The decay rate of infected cells and 2-LTR containing cell are represented by a and δ. Thus the equations have the form,

$$\begin{aligned} \dot{\mathbf{y}} &= (1-\eta_{II}\mathbf{u_{II}})aR\mathbf{y} - a\mathbf{y} + \mathbf{y_e} \\ \dot{\mathbf{c}} &= \phi k_{II}(1-\eta_{II}\mathbf{u_{II}})aR\mathbf{y} + k_{II}\eta_{II}\mathbf{u_{II}}aR\mathbf{y} - \delta\mathbf{c}. \end{aligned} \tag{1.1}$$

Here R represents the reproductive ratio under cART. If the replication is happening, R has values close to one. k_{II} is the probability of integration failure by raltegravir per million of blood mononuclear cells (PBMC), and ϕk_{II} refers to the same probability but when the virus entry is not interrupted by raltegravir. When fitted to the data in Buzon

et al. [11] of the 13 patients with 2-LTR transient response after RAL intensification, the infection success ratio R was in the range $(0.99, 1)$ consistent with the hypothesis of ongoing replication in a reservoir, in this subset of patients. This reduced model showed also a dramatic qualitative difference in the expected behavior of measured 2-LTR following raltegravir intensification. If the primary source of new infection events was the activation of latently infected cells ($R < 1$), consistent with controlled viremia, the 2-LTR response to raltegravir intensification should be monotonically increasing, as the plot in red in figure 1.5. If the primary source of new infection were a stable cycle of successful infection and lysis of target cells ($R \sim 1$), the 2-LTR response to raltegravir intensification would be a sharp, transient increase, as was seen in [11] (in blue in figure 1.5). The estimated decay rate δ for the 2-LTR had a median of 0.47 days^{-1}, in congruency with previous estimations in-vivo [82, 57]. Given the previous results, if replication rates were homogenous, this would result in measurable plasma viremia; as this was not seen, the replication resulting in the formation of 2-LTR episomes must be occurring in a spatially remote sanctuary site [47]. While several studies have failed to show evidence of ongoing cycles of HIV-1 infection, due to the lack of plasma viral load changes under the conditions described in Buzon et al. [35, 34, 74], the absence of significant changes in plasma HIV-1 is not inconsistent with the existence of ongoing replication in compartments with limited communication with the plasma [35, 34, 14, 74]. There is evidence that viral replication is compartmentalized, isolated by potential barriers between plasma and certain tissues and organs [22, 53]. This compartmentalization could also explain the lack of observed sequence evolution in HIV [28, 3], as the samples taken from the blood may not reflect replication occurring in other compartments.

1.5 Lymphoid Tissue as Sanctuary Site

The results of the previous section are only biologically feasible if there exist sites within the body that allow ongoing viral replication. These sites must have the spatial dynamics that provide the balance of isolation and connectivity needed to allow

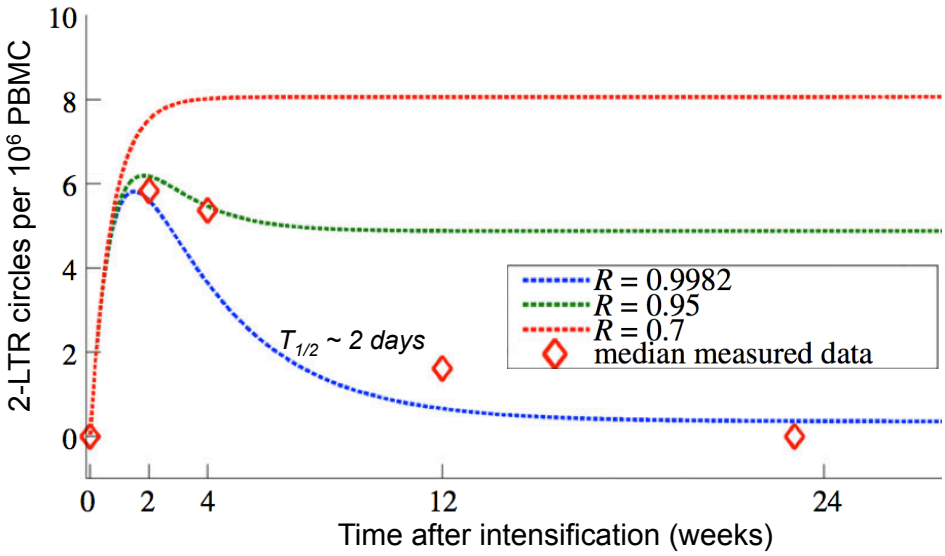

Figure 1.5: 2-LTR Buzon study data fitting. The 2-LTR circles transient behavior data is only possible to be fitted for the model when the values of R are equal to 1 (in blue), meaning that ongoing replication is happening. When R is smaller than 1, the only behavior, obtained by the activation of latent cells is a monotonic one, (Data taken from [47]).

ongoing viral replication that cannot be seen in the blood, but revealed through the production of 2-LTR products measurable in the blood (see figure 1.6). These sites would have to be sufficiently isolated from the blood that reduced concentrations of the antiviral drugs can be maintained. They would also have to be sufficiently isolated that neither virus nor infected cells produced in the sites are likely to survive the time required to diffuse into the blood. They would, however, need to be sufficiently connected that the cells containing 2-LTR circles created in the site do survive long enough to be measured in the blood. Furthermore, they need to be connected enough that the drug raltegravir can penetrate the site in concentrations adequate to cause the observed reduction in virus production. For the reasons discussed above, lymph nodes, specifically the follicle region, could potentially satisfy these requirements. Lymph nodes (LNs) have been suggested as sanctuary sites, compartments where antiretroviral

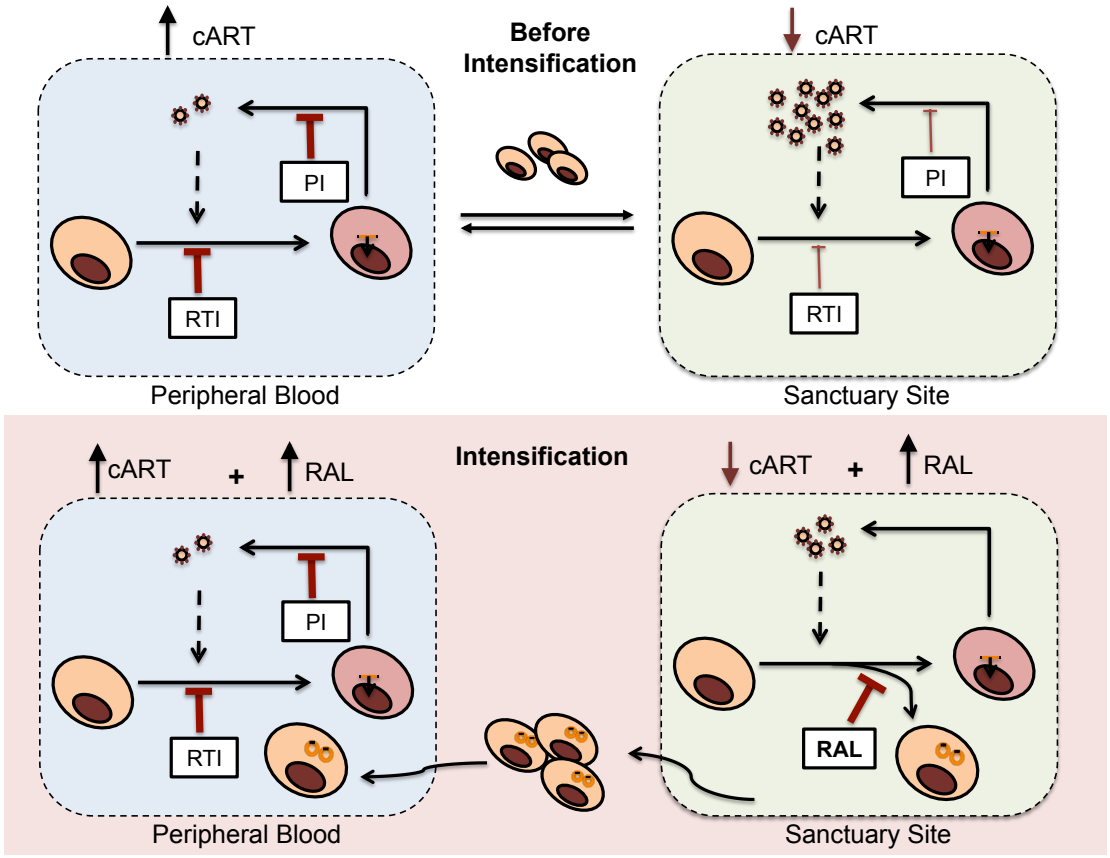

Figure 1.6: Drug sanctuary site hypothesis. If 2-LTR circles are present in the blood, but the plasma viral load is low, if ongoing replication is happening, a drug sanctuary is a plausible hypothesis. This hypothesis presents that drug distribution is suboptimal in some tissues allowing viral replication. However, RAL can penetrate this sanctuary, allowing 2-LTR formation there. Therefore, 2-LTR measurements represents those in T-cells coming from the sanctuary.

drugs are inefficient or do not have penetration [45, 62, 44]. LNs are small bean shaped secondary organs that belong to the lymphatic system. Their principal goal is to allow encounters between T cells and antigen presented cells to activate an immune response when antigens are present. Follicles and paracortex in the lymph nodes are known to serve as a preferred location for HIV replication [31]. Studies with patients treated with cART for more than one year, described long-term persistence of HIV-1 structural

proteins and glycoproteins in the germinal centers of lymph nodes despite undetectable plasma HIV-1 replication, suggesting the additional role of lymph nodes as anatomical reservoirs [67, 78]. Systemic analysis of SIV-infected Rhesus macaques receiving cART for 1 year also found high levels of vRNA in the lymph nodes [40].

By modeling the interactions between the fluid, well-mixed blood and fluid lymph and a semi-solid, diffusive lymphoid follicle based sanctuary site, we aim to determine whether it is feasible that lymphoid follicle sanctuary sites are producing the pattern of 2-LTR and viral load blood measurements seen experimentally. Many of the spatial diffusion rates of the cells, viruses, and drugs within the lymphoid follicle regions have been measured experimentally; others can be adequately estimated using basic physical principles.

1.6 Goals and Organization

In this dissertation, we propose a model-based study articulating the possible mechanisms of ongoing replication occurring in lymphoid follicle sanctuary sites and investigate the patterns of 2-LTR formation expected after raltegravir application and viral blips. Using the model this dissertation has the goal to answering the following questions:

1. Could sub-optimal drug penetration in inflamed lymph nodes sustain de-novo viral replication in patients under cART and produce patterns of transient 2-LTR circles in PBMC after raltegravir intensification?
2. What would be the reservoir size and drug penetration to sustain de-novo viral replication inside lymph nodes in patients under cART?
3. How correlated is 2-LTR maximum value in PBMC with total recent de-novo infection?
4. Is neglecting re-circulation of T-cells overestimating the measured 2-LTR half-life in-vivo?
5. Could cryptic viremia produce viral blips patterns?

The organization of the dissertation to answer these questions is outlined in the following way. In chapter 2, we present a mathematical model to examine whether

lymph nodes can function as sanctuary sites for ongoing viral replication, incorporating the spatial dynamics neglected in [47]. A spatial differential equation is described taking into account the dynamics of infected and uninfected CD4+ T cells, free virus, and cells containing 2-LTR circles. The sanctuary site is modeled with limited penetration of the antiviral drugs. Based on several assumptions, we simplify the reaction-diffusion equations describing the dynamics into a set of compartmental diffusively-coupled ordinary differential equations.

In chapter 3 we present the reproductive ratio of the virus in each compartment, prior to raltegravir intensification if the compartment were isolated and its relation with suboptimal drug penetration. We use this ratio as a measure to determine lower bound conditions for cryptic viremia under cART before intensification and for 2-LTR transient results after intensification. We describe the mechanisms by which this could be possible, and the conditions needed to generate the transient behavior of both measured 2-LTR and low HIV viremia in the blood after administering raltegravir in patients on apparently suppressive cART regimens as shown in [11]. Monte-Carlo simulation of the model using previously published distributions of the model parameters is performed to determine what parameter values are consistent with the observed 2-LTR transient behavior. In this simulation an unevenly-fixed drug penetration is assumed.

In chapter 4 we develop an analysis of the stability properties of the diffusively coupled system. Using this analysis we present a way to characterize cryptic viremia inside lymph nodes. A similar Monte-Carlo simulation of the model of the previous chapter is performed. In this chapter, however, conditions for cryptic viremia are expanded including combination size with drug penetration ratios inside the lymph node. Moreover, the chapter includes a description of different possible 2-LTR decay rates and quantitative comparison between Buzon et al. data and simulations of 2-LTR circles in the main compartment. Finally, we present that measurable 2-LTR circles maximum values are correlated to the total infection in the body but with different patterns of drug penetration and reservoir size for each peak.

In chapter 5 we describe, through a Bayesian MCMC analysis, how neglecting T cells recirculation could affect prior estimation of 2-LTR circles half-life. We analyze the bias introduced by the model mismatch by identifying the parameters of the simple model presented above using simulated data generated from the best fits of the compartmental model the INTEGRAL data. The data from the INTEGRAL study presented the 2-LTR circles behavior of a set of patients with raltegravir insensification of cART after a year of treatment. The simulated data follows two sampling schedules, and it is corrupted by the measurement noise process described in [49]. The identified parameter values are then correlated to the parameter values used to generate the simulated data. Finally, we performed a comparison of the median of the posterior distribution for the 2-LTR decay rate and the median of that rate value to create the virtual data.

In chapter 6 we present how viral blips could be related to cryptic viremia. We do a theoretical analysis of the model to find conditions than guarantee that the system does not present cryptic viremia, and thus, has an initial state of the system. Then we characterize the occurrence, duration, amplitude and final value of the viral blip in terms of how the diameter of the lymph nodes changes. We show that these changes in the diameter affect mainly the connectivity between compartments leading to transient episodes of viremia in the main compartment representing the blood.

Finally in chapter 7 we present summary conclusions of all the previous chapters and discuss various directions for future research.

1.7 Impact and Significance

The production of a novel viral mutant is a random event, with a chance of occurrence that depends on the number of point mutations needed and the intrinsic mutation rate for HIV. The activation of latent reservoirs will not contribute to the evolution of resistance, as those cells do not produce any novel mutations during activation. If HIV-1 de-novo infection is happening in sanctuary sites, viral replication will certainly contribute to the production of novel viral mutants. Therefore, the detection

of this cryptic viremia has high relevance in practice. In this work, we present a solid foundation theory for the relation of 2-LTR formation and recent infection in sanctuary sites. The results of this work will contribute for the development of clinically useful method for detecting and quantifying cryptic viremia using 2-LTR circles and raltegravir intensification following the procedure proposed in [47] . Thus, detecting cryptic viremia in clinical settings will enable management regimen changes if necessary, and will also allow for minimally invasive comparative testing of the efficacy of antiviral drugs in preventing or eliminating cryptic viremia. Moreover, this work also contribute in the analysis of the bias introduced by the model mismatch by identifying the parameters of the simple model using simulated data generated from the compartmental model. This has significant implications for the durability of antiviral therapy, and for any attempts to functional cures for HIV infection.

Chapter 2

SPATIAL MODEL OF CRYPTIC VIREMIA AND 2-LTR FORMATION

2.1 Introduction

When viral cDNA fails to integrate into host CD4+T cells, episomal artifacts including linear unintegrated DNA, 1-LTR circles, and 2-LTR circles form. 2-LTR formation can only happen following a successful reverse transcription event. Previous studies have shown no significant viral change in the blood after raltegravir intensification in patients under cART. If the 2-LTR production is arising from interrupted rounds of successful infection, this implies that the 2-LTR containing T-cells come from an anatomical compartment diffusively remote from the blood. The model we propose assumes that the paracortex/follicle within lymph nodes are anatomical compartments with reduced drug efficacy, from which T-cells with 2-LTR recirculate after raltegravir is applied. The main objective is to determine whether this hypothesis is consistent with the observed dynamics of 2-LTR following raltegravir intensification.

The re-circulation and motility of T-cells has been broadly studied. As depicted in figure 2.1, re-circulation includes the entry into the lymph node, the motility inside and the exit from the paracortex of the node. There are two main entries for lymphocytes into the lymph nodes, through high endothelial venules (HEV) and the afferent lymphatic vessels (AL) in the sub-capsular sinus. The HEV route is preferred over the AL for T -cells so that in the absence of infection, up to $\sim$ 2 percent of T-cells are recruited via HEVs from the recirculating pool per day [79]. This preferred way for T-Cells to enter the lymph nodes is highly selective and efficient. A guided cascade facilitates the crossing of the lymphocytes through the HEV's wall. Inside the paracortex of the lymph node, the cells follow a random walk in a cord-like arrangement

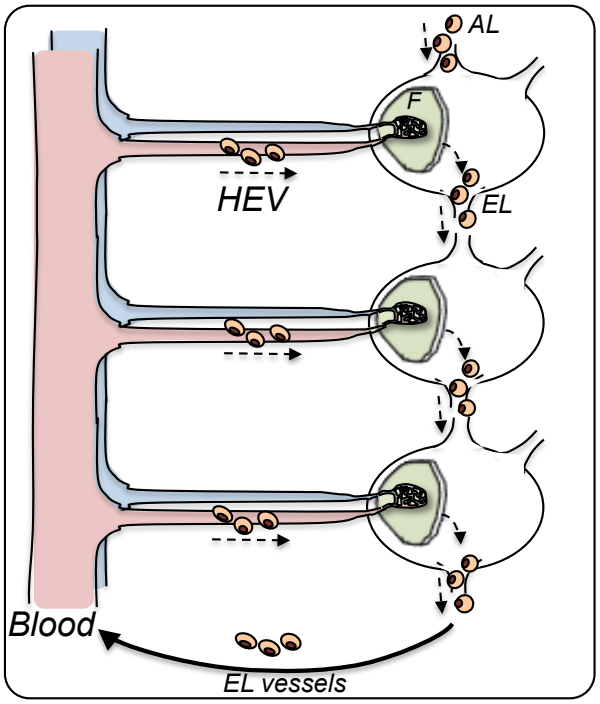

Figure 2.1: Recirculation of T cells. T cells enter the LNs from the blood via high endothelial venules (HEV) and from the interstitial fluid or other LNS via Afferent lymphatic vessels (AL). After some time inside the LNs (this time depends if they encounter antigens), they are back to the recirculation through efferent lymphatic vessels (EL).

of concentric layers of fibroblastic reticular cells (FRCs). Each paracortical cord is between 10 and 15 μm in length, and the T-cells has been reported to have an average 3D velocity of $\sim 15\frac{\mu m}{min}$ and a motility coefficient about $50-100\frac{\mu m^2}{min}$ [53, 79, 36, 7]. The random walk permits the interaction of T-cells with dendritic cells needed to recognize antigens [79, 36]. In uninflamed lymph nodes, the T cells will explore a particular lymph node for between 6 and 18 hours [54, 79], though cytokine signals in inflamed lymph nodes can make this considerably longer [36]. If naive lymphocytes do not encounter antigens, they eventually leave the paracortex by the cortical sinus and the lymph node through efferent lymphatics. The total recirculation time is estimated to be between 52 and 69 hours on average [65]

Several different approaches have been used to model lymph nodes [53, 43, 5, 50], but none with the purpose of explaining ongoing viral replication. Some researchers have explained HIV dynamics in compartments, but none has accounted for 2-LTR formation as a marker of low level replication [12, 70]. Here, we present in detail the assumptions and description of a multi-compartmental model of the viral dynamics in the blood and the lymph nodes paracortex/follicle sites. The model includes the transport of cells and virus between compartments and extends the single-compartmental model in [47] to include spatial dynamics of 2-LTR containing cells and how hey are formed in the blood. Furthermore, we present a description of the parameters and the assumption made for their values.

2.2 Development of the Spatial Model

The model represents the conditions for the formation of 2-LTR in T-cells due to HIV dynamics both inside the lymphoid follicles and the blood as well as the motility of the CD4+ T cells among them. We used the basic model of HIV dynamics with its associated assumptions [64, 60, 80, 66, 39]. Furthermore, we include the assumptions that the two sources of 2-LTR formation in T-cells are the intrinsic one unenhanced by raltegravir and the one caused by the application of raltegravir formulated in [47] and used in [14]. Several assumptions of the recirculation and motility of the T-cells and HIV in the initial compartmental model are proposed in [14]. Firstly, the recirculation of T-cells from the inner sites of the lymph nodes to the lymphatic vessels and the blood is diffusion-like. Second, the motility of T-cells inside the lymphoid follicles is also analogous to diffusion, moving in apparently random walk fashion [53]. Third, HIV is only transported in/out the lymphoid follicles inside infected T-cells [55]. Fourth, HIV moves inside the lymphoid follicles by diffusion. Fifth, T-Cells and virions move rapidly enough such that the Lymphoid Follicle is well-described by concentric homogenous spherical domains. Finally, we assume the blood and lymphatic vessels can be jointly described by a single, well-stirred compartment.

Based on these assumptions, we simplify the reaction-diffusion equations describing the dynamics into a set of compartmental diffusively-coupled ODEs as in [9, 8, 27]. The system has the following configuration: one main compartment representing the blood, the HEVs and the lymphatic vessels and N secondary compartments representing all the lymph nodes paracortex/follicle sites in human body. These N compartments have no connections between them but only with the main compartment as Figure 2.2 depicts. Reaction-diffusion dynamics is assumed to dominate within each of the N secondary spherical compartments. The method of lines is used to spatially discretize each of the N spherical compartments, and spherical symmetry is exploited, allowing the spheres to be subdivided into $n-1$ concentric spherical shells where only the most external one is connected with the blood compartment. The different shells are denoted by the subscript i. Since all N compartments have the same geometrical configuration, this result in an ODE model of $4n$ equations.

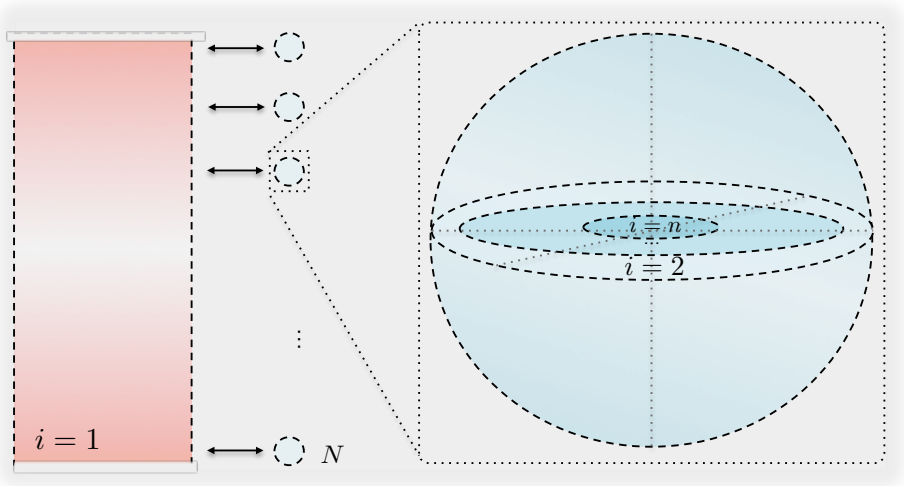

Figure 2.2: Configuration of compartments. On the left, the main compartment representing the blood, HEVs and lymphatic vessels. In the middle, the N secondary spherical compartments representing the lymph nodes paracortex/follicle sites and, on the right, the formulation of each sphere as $n-1$ concentric homogeneous shells.

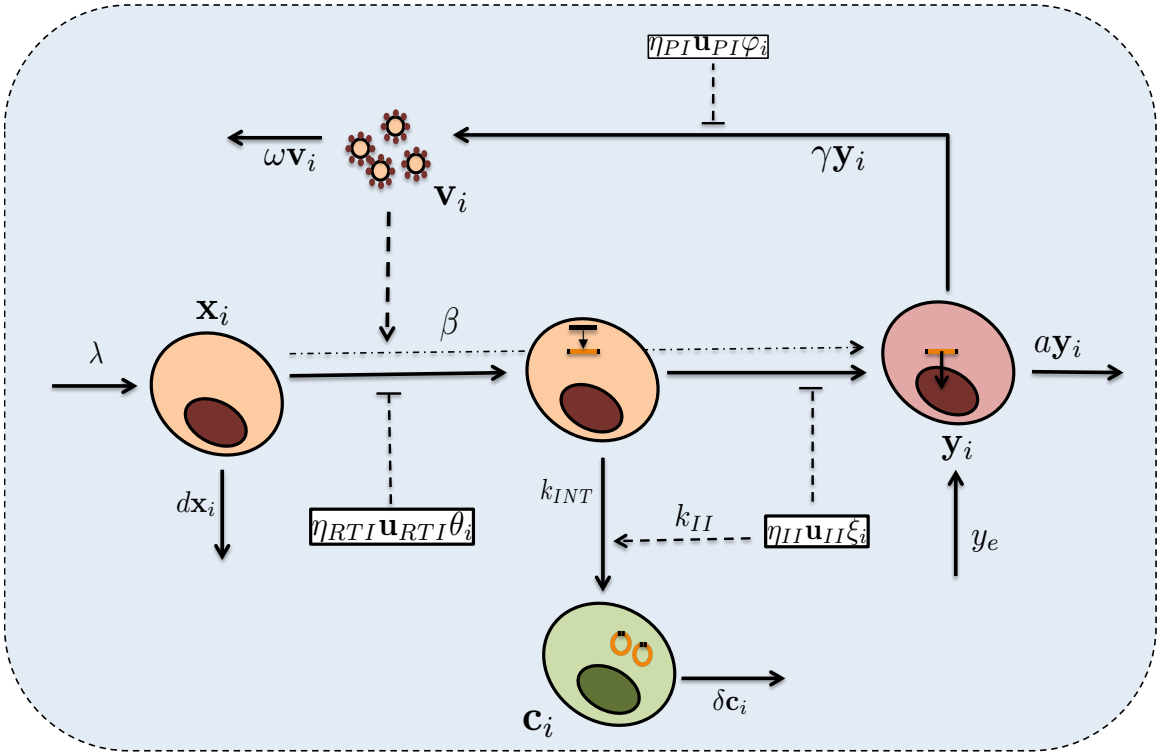

Figure 2.3: Illustration of the model. Description of the HIV life cycle, the formation of 2-LTR circles in T-cells and the influence of the drug in each compartment and the variables that represent each element.

As depicted in Figure 2.3, in each compartment CD4+ T target cells $\mathbf{x}_i$, are produced at a rate λ, decay at a rate $d\mathbf{x}_i$ and are infected at a rate $\beta\mathbf{x}_i\mathbf{v}_i$. The rate is reduced by the activity of reverse transcriptase inhibitors (RTI) $\mathbf{u}_{RTI}$ and integrase inhibitors (II) $\mathbf{u}_{II}$ with maximum effectiveness of η_{RTI} and η_{II}. We hypothesize that the efficacy of the drug depends on the domain; therefore, we include a spatial dependence drug penetration distribution θ_i and ξ_i for RTI and II respectively. Exogenous sources, particularly the activation of latent infected T-cells, contribute to create actively infected cells at a rate $\mathbf{y}_e$. The infected cells $\mathbf{y}_i$ die at a rate $a\mathbf{y}_i$ and produce virions at a rate $\gamma\mathbf{y}_i$. This viral production is interrupted by protease inhibitors $\mathbf{u}_{PI}$ with

maximum efficiency η_{PI} (the activity of protease inhibitors results in the production of non-infectious particles, which are neglected in this model). The activity of this drug is also assumed to vary spatially by a factor φ_i. Free virus exponentially decays at a rate $\omega \mathbf{v}_i$. Viral entry leads to the formation of linear unintegrated HIV DNA at a rate inhibited by the activity of RTI drugs. In the case of no integrase inhibitor intensification ($\mathbf{u}_{II} = 0$), DNA copies may fail to integrate into the host cell genome at a small intrinsic rate ϕk_{II} resulting in the formation of cells with 2-LTR $\mathbf{c}_i$. In the case of intensification with integrase inhibitors ($\mathbf{u}_{II} = 1$), this rate of 2-LTR production is increased to $k_{II}\eta_{II}\mathbf{u}_{II}\xi_i$ in this compartment, with a concomitant decrease in the intrinsic rate to avoid the possibility of counting the same 2-LTR formation event twice. The 2-LTR containing cells decay at a rate $\delta \mathbf{c}$.

Communication between the compartments is modeled as diffusion, where $\mathcal{N}_i$ represents the set of the adjacent layers of i, $D_{i,j}^{(\cdot)} = \frac{D_{(\cdot)i,j}}{l}\frac{A_{i,j}}{V_i}$ with $A_{i,j}$ representing the surface area between each layer in the sphere, V_i the volume of the layer, and $\frac{D_{(x)i,j}}{l} = \frac{D_{(y)i,j}}{l} = \frac{D_{(c)i,j}}{l}$ and $\frac{D_{(v)i,j}}{l}$ the effective diffusivity of target, infected, 2-LTR containing T-cells and HIV virions between layers.

The first compartment ($s = 1$) represents the blood and free-flowing lymph, and connects with all the N spherical sites. As a result, the equations for the first compartment have a special form, which may be written as:

$$\begin{aligned}
\dot{\mathbf{x}}_1 &= \lambda - d\mathbf{x}_1 - \beta \mathbf{x}_1 \mathbf{v}_1 (1 - \eta_{RTI}\mathbf{u}_{RTI}\theta_1)(1 - \eta_{II}\mathbf{u}_{II}\xi_1) \\
&\quad + N D_{1,2}^{(x)}(\mathbf{x}_2 - \mathbf{x}_1) \\
\dot{\mathbf{y}}_1 &= \beta \mathbf{x}_1 \mathbf{v}_1 (1 - \eta_{RTI}\mathbf{u}_{RTI}\theta_1)(1 - \eta_{II}\mathbf{u}_{II}\xi_1) - a\mathbf{y}_1 + \mathbf{y}_e \\
&\quad + N D_{1,2}^{(y)}(\mathbf{y}_2 - \mathbf{y}_1) \\
\dot{\mathbf{v}}_1 &= \gamma(1 - \eta_{PI}\mathbf{u}_{PI}\varphi_1)\mathbf{y}_1 - \omega \mathbf{v}_1 + N D_{1,2}^{(x)}(\mathbf{v}_2 - \mathbf{v}_1) \\
\dot{\mathbf{c}}_1 &= \beta \mathbf{x}_1 \mathbf{v}_1 (1 - \eta_{RTI}\mathbf{u}_{RTI}\theta_1)(\phi k_{II}(1 - \eta_{II}\mathbf{u}_{II}\xi_1) + k_{II}\eta_{II}\mathbf{u}_{II}\xi_1) \\
&\quad - \delta \mathbf{c}_1 + N D_{1,2}^{(c)}(\mathbf{c}_2 - \mathbf{c}_1).
\end{aligned} \tag{2.1}$$

For the remaining $n-1$ spherical shell compartments (representing the reaction-diffusion dynamics within the LF site), the equations may be written as:

$$
\begin{aligned}
\dot{\mathbf{x}}_i &= \lambda - d\mathbf{x}_i - \beta \mathbf{x}_i \mathbf{v}_i (1 - \eta_{RTI} \mathbf{u}_{RTI} \theta_i) \\
&\quad \times (1 - \eta_{II} \mathbf{u}_{II} \xi_i) + \textstyle\sum_{j \in \mathcal{N}_i} D^{(x)}_{i,j} (\mathbf{x}_j - \mathbf{x}_i), \\
\dot{\mathbf{y}}_i &= \beta \mathbf{x}_i \mathbf{v}_i (1 - \eta_{RTI} \mathbf{u}_{RTI} \theta_i)(1 - \eta_{II} \mathbf{u}_{II} \xi_i) - a \mathbf{y}_i \\
&\quad + y_e + \textstyle\sum_{j \in \mathcal{N}_i} D^{(y)}_{i,j} (\mathbf{y}_j - \mathbf{y}_i), \\
\dot{\mathbf{v}}_i &= \gamma (1 - \eta_{PI} \mathbf{u}_{PI} \varphi_i) \mathbf{y}_i - \omega \mathbf{v}_i \\
&\quad + \textstyle\sum_{j \in \mathcal{N}_i} D^{(v)}_{i,j} (\mathbf{v}_j - \mathbf{v}_i). \\
\dot{\mathbf{c}}_i &= \beta \mathbf{x}_i \mathbf{v}_i (1 - \eta_{RTI} \mathbf{u}_{RTI} \theta_i) \\
&\quad \times (\phi k_{II} (1 - \eta_{II} \mathbf{u}_{II} \xi_i) + k_{II} \eta_{II} \mathbf{u}_{II} \xi_i) - \delta \mathbf{c}_i \\
&\quad + \textstyle\sum_{j \in \mathcal{N}_i} D^{(c)}_{i,j} (\mathbf{c}_j - \mathbf{c}_i).
\end{aligned}
\tag{2.2}
$$

2.3 Parameters

To obtain realistic conditions for the 2-LTR dynamics seen in blood assuming lymph nodes paracortex/follicle acting as sanctuary sites, the parameters for viral dynamics, 2-LTR formation, drug penetration, and diffusion/geometry values have to be defined. The parameters include the local reaction rates and the diffusion rates between compartments.

2.3.1 HIV reaction rates

The proliferation and clearance rates of target CD4+ T-cells λ and d, the death rate of infected cells a, the density dependent infection and virion production rates β and γ respectively, and the reservoir contribution rate y_e were selected from the values obtained by parameter identification in [48] generated by a Bayesian Markov-Chain Monte Carlo technique. This study estimates the parameters from data taken from HIV patients who had 3 to 5 treatment interruptions cycles each. These data produced a posterior distribution of parameter values, including drug efficacy, conditioned on the observed data.

2.3.2 2-LTR formation rates

The parameters for the 2-LTR formation include K_{II}, ϕ, and δ. K_{II} and is the product of a scaling factor which describes the volume that contains 10^6 PBMC (Peripheral Blood Mononuclear cells) and non-dimensional factors that relate the fraction of integration events that fail after raltegravir is applied. From [21, 32] we assume that a volume in the range $[270 - 910]\,\frac{\mu L}{10^6 PBMC}$ is high likely to have interruptions of integration events by raltegravir (very close to 1). ϕ is the ratio between intrinsic and raltegravir enhanced likelihood of cDNA integration failure. δ is the decay rate of observed 2-LTR *in vivo*. We base the previous values from the estimation obtained in [47] using data from [11] and the values estimated from previous studies [21, 57, 68, 82].

2.3.3 Diffusion

To determine the diffusion parameters in the model depend on the diameter of the spherical compartment and the values for effective diffusivity of the T-cells and the virus. Studies have shown that hyperplastic lymphoid follicles can be as large as 1mm in diameter [61]. Thus, we vary the site diameter around this value to determine the effect site size has on the 2-LTR transient behavior. Effective diffusivity of T-cells between the main compartment and the paracortex/follicle site $\frac{D_{(x)_{1,2}}}{l}$, $\frac{D_{(y)_{1,2}}}{l}$ and $\frac{D_{(c)_{1,2}}}{l}$, we note that without infection, one mouse lymph node recruits approximately 2% of the T-cells from recirculating pool per day, and the average diameter of a mouse LN is 1mm [43, 76]. Diffusion into the lymph node is given by the equation $\frac{D_{x_{b,LN}}}{l}\frac{A_{b,LN}}{V_{LN}}\mathbf{x_b} = 0.02\mathbf{x_b}$, where $\frac{D_{x_{b,LN}}}{l}$ is the effective diffusivity between the blood and one mouse lymph node, and $A_{b,LN}$ and V_{LN} the surface area and volume of the mouse lymph node respectively. Thus, $\frac{D_{x_{b,LN}}}{l}$ must be approximately $\frac{1}{300}\frac{mm}{day}$, which we use as the estimated value of $\frac{D_{(x)_{1,2}}}{l}$, $\frac{D_{(y)_{1,2}}}{l}$ and $\frac{D_{(c)_{1,2}}}{l}$.

The effective diffusion of T-cells between layers within the lymphoid paracortex/follicle is the average value of the experimentally observed motility coefficient of T-Cells within lymphoid follicles of $0.1\frac{mm^2}{day}$ [53, 79, 36, 7] divided by the length of each layer $l = \frac{r}{n-1}$, where r is the radius of the paracortex/follicle site.

The effective diffusion of the virus approximately is assumed to be zero between the main compartment and the spherical sites and that the virus is carried into them only by T-cells. This is because the separating boundary is known to act as a molecular sieve for particles smaller than an HIV particle [79]. The effective diffusivity between compartments is assumed to follow the derivation in [46, 56] for a spherical virus. Assuming the diameter of HIV equal to 120 nm a diffusion coefficient of $0.43\frac{mm^2}{day}$ is calculated and divided by the width of each layer, $l = \frac{r}{n-1}$ to obtain the effective diffusivity.

2.3.4 Sanctuary sites and Drug Penetration

The drug penetration distribution in each compartment is not well understood, and we investigate multiple possibilities. We assume that each drug has a penetration of 100% in the first compartment, and for θ_i and φ_i we assume a geometric sequence with ratio $\frac{1}{2}$ while for ξ_i a geometric ratio equal to 1 and has a value of 0.7 for compartment 1 to n.

These equations for drug efficacy are consistent with reduced diffusion of the drug into the sanctuary site, and assume that the intracellular half-life of the drugs is shorter than the time spent in the sites by the T Cells. For the nominal parameters used in this study, the median time spent by a T Cell in the sanctuary site depends on the site diameter, and ranges between 1.5 days for site diameters of 0.1 mm up to 15 days for site diameters of 1 mm (see appendix A). These times are compatible with the experimentally determined times discussed previously [54, 79, 36], and also provides a mechanism for the longer times associated with lymphoid inflammation. These times are also longer than the half-lives of all of the antiviral drugs [6], though a few drugs, such as the non-nucleoside reverse transcriptase inhibitors or the nucleotide analogue tenofovir, have half-lives comparable to the time spent in smaller lymph nodes. Other mechanisms besides diffusion may also result in reduced concentrations and/or efficacies of the antiretrovirals in the lymphoid follicles; the model could be modified to account for alternative mechanisms through modification of the equations ξ_i, θ_i and φ_i.

Chapter 3

BASIC REPRODUCTIVE RATIO AND CRYPTIC VIREMIA

3.1 Introduction

Basic reproductive ratio has been broadly used to characterize the capacity of the virus to sustain replication. Here we present how this concept can be used in multi-compartmental modeling to find conditions for cryptic viremia.

If the compartments were isolated, then, prior to integrase inhibitor application, each compartment has a basic reproductive ratio,

$$\hat{R}_{0_i} = \frac{\beta\lambda\gamma}{da\omega} \times (1 - \eta_{RTI}\mathbf{u}_{RTI}\theta_i) \times (1 - \eta_{PI}\mathbf{u}_{PI}\varphi_i). \tag{3.1}$$

Here, $\hat{R}_{0_i}$ relates each phase of the HIV cycle, drug efficiency and drug penetration in each compartment with the form of equation (3.1). When the value of $\hat{R}_{0_i}$ is greater than 1, the virus grows exponentially, and when it is smaller than 1 the virus decays exponentially. Note that the smaller the values of θ_i or φ_i, the larger the initial growth rate of the virus in the compartment.

Since we assume 100% penetration in compartment 1, $\hat{R}_{0_1} < 1$ is guaranteed. Consequently, the region between the third and the n^{th} compartment composes the true sanctuary site, with drug efficacy sufficiently low to enable persistent virus replication. The compartment diffusively furthest from the plasma has the smallest drug effectiveness. This last compartment has an extremely low drug efficacy and $\hat{R}_{0_{s>2}} > 1$. The second compartment composes a transition region, with reduced drug efficacy relative to the main compartment and in consequence $\hat{R}_{0_2} \sim 1$.

Since the drug distribution is assumed to decrease with compartment, the $i = 2$ compartment has the highest drug activity in the sphere and thus the smallest $\hat{R}_{0_i}$.

Consequently, if there is viral replication in compartment $i = 2$, this implies the presence of viral replication in all compartments $i > 2$. Thus, we can use $\hat{R}_{0_2}$ as a measure to determine lower bound conditions for cryptic viremia under cART before intensification and for 2-LTR transient results after intensification.

We show that the observed patterns of 2-LTR and virus dynamics following raltegravir intensification can be reproduced by our model if the sanctuary sites are sufficiently large and the drug efficacy within the sites is sufficiently small. We show that, in the absence of these conditions, fundamentally different patterns of measured 2-LTR and virus in the blood are predicted following raltegravir intensification.

3.2 Monte-Carlo Simulation

Based on the models of equations (2.1) and (2.2), two Monte-Carlo simulations characterize the conditions under which HIV replication and the 2-LTR transient behavior (the initial rise follow by a fall of the episomes) is possible, subject to random variation of the HIV reaction and diffusion parameters within the prior distributions described in Tables 3.1 and 3.2.

The first simulation seeks to determine the minimum value of $\hat{R}_{0_2}$ for which the 2-LTR transient behavior in blood is observed. In this simulation we randomly generated 1,000 set of parameters for virus and T-cell rates from the posterior distributions estimated in [48]. We made the simulations for a fixed volume value of 30 mL, for all N spherical sites tissue, with each site having diameters of 0.5, 1, 1.5 or 2 mm. For each set of parameters the simulations were run after 600 days when each variable have reach its steady state, and thus take those values to obtain the cryptic viremia conditions results.

Using the results of the first simulation, the second examines the change in the transient peak value of 2-LTR in the blood as the total tissue volume of the N compartments and the individual sphere diameter of lymph nodes varies. In this second simulation, we run a 80,000-trial Monte-Carlo simulation using the priors previously described with total tissue volume and individual sphere diameter drawn from the

uniform distributions $30-499$ mL and $0.1-2$ mm respectively. We applied raltegravir in the simulation after 600 days, and use the simulated time series to do the analysis.

Table 3.1: HIV Dynamics parameters. Parameters for HIV an T cells rates in log-scale except for ω, taken from the maximum likelihood ranges in [48].

Parameters	Value	Units
$log_{10}(\lambda)$	$(1.54, 2.88)$	$log_{10}\left(\frac{cells}{\mu L \times day}\right)$
$log_{10}(d)$	$(-1.35, -0.34)$	$log_{10}\left(\frac{1}{day}\right)$
$log_{10}(\beta)$	$(-5.78, -5.23)$	$log_{10}\left(\frac{mL}{copies \times day}\right)$
$log_{10}(a)$	$(-0.76, 0.42)$	$log_{10}\left(\frac{1}{day}\right)$
$log_{10}(\gamma)$	$(3.39, 4.00)$	$log_{10}\left(\frac{copies \times \mu L}{cells \times mL \times day}\right)$
ω	18.8	$\frac{1}{day}$
$log_{10}(\eta)$	$(0.60, 0.89)$	–

Table 3.2: 2-LTR circles parameters. Parameters for 2-LTR formation and decay rates determined in [47].

Parameters	Value	Units
k_{II}	$(270, 910)$	$\frac{\mu L}{10^6 PBMC}$
ϕ	0.002	–
δ	0.46	$\frac{1}{day}$

3.3 Reproductive Ratio and Conditions for Cryptic Viremia

$\hat{R}_{0_2}$ defines the reproductive ratio of the virus in in the compartment with highest drug activity prior to raltegravir intensification if the compartment were isolated (as the compartments are not isolated, the actual reproductive ratio can be greater or smaller depending on the behavior of neighboring compartments). Thus, we use $\hat{R}_{0_2}$ to determine lower conditions for cryptic viremia.

For the 1,000-trial Monte-Carlo simulation of the model defined by Equations (2.1) and (2.2), we use parameters drawn from the prior distributions generated by a Bayesian Markov-Chain Monte Carlo technique in [48], leading to the values for $\hat{R}_{0_2}$

in the range 0.8 to 1.15. The total volume of all N spherical sites tissue is 30 mL, with each individual site having diameters of either 0.5, 1, 1.5 or 2 mm. Note that, we are using a fixed tissue volume for the N spherical lymph nodes and for each change in an individual sphere, consequently the total number of spherical compartments N is variable. The median observed viral loads in the center of the spherical site (compartment 10) prior to integrase inhibitor intensification are plotted against $\hat{R}_{0_2}$ in Figure 3.1.

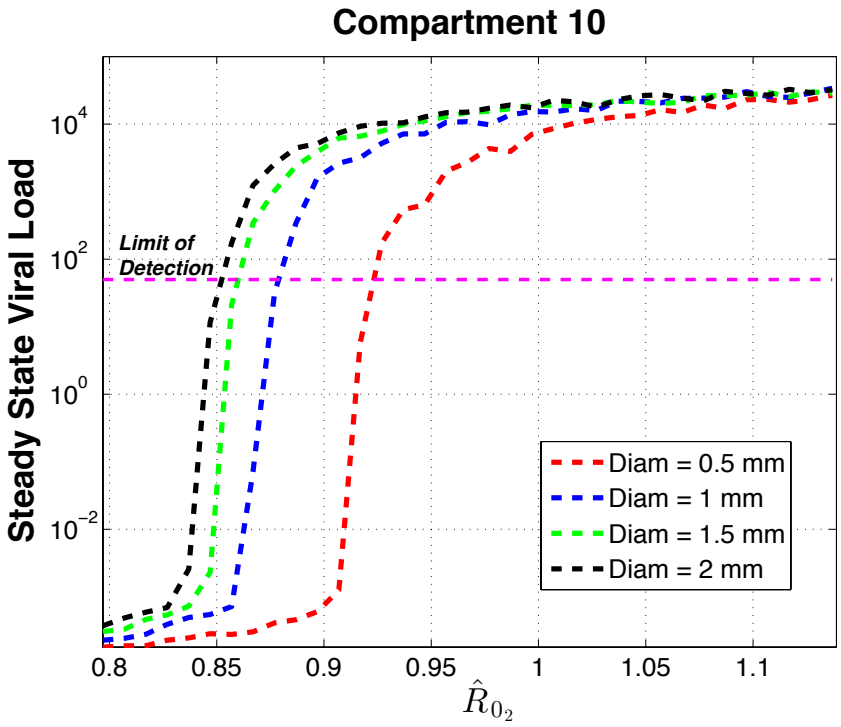

Figure 3.1: Pre-intensification Viral Load in Sanctuary site. Average steady state of viral load in the most remote compartment versus $\hat{R}_{0_2}$ for diameter length of 0.5, 1, 1.5 and 2 mm.

The plot describes the median steady-state viral load in compartment 10 before intensification and the horizontal line the normal assays limit of detection. In all cases, the viral load in Compartment 1, which describes the blood and free-flowing lymph, was well below the limit of detection, demonstrating that the model is consistent with

cryptic viremia not detectable in the blood. As shown in Figure 3.1, $\hat{R}_{0_2}$ must be greater than 0.85, 0.86, 0.88 and 0.93 for diameter size of 2, 1.5, 1 and 0.5 mm respectively to have a detectable viral load in the most remote compartment. Above the critical threshold, the total viral load saturates quickly, and target-cell depletion determines the steady-state viral load. The conditions for cryptic viremia before intensification are related to the transient behavior of 2-LTR in blood after adding raltegravir.

3.4 Reproductive Ratio and 2-LTR Formation

To better understand the role of $\hat{R}_{0_2}$ in the 2-LTR formation in the blood after raltegravir intensification we use the results of the 80,000 trials where we simulated the application of raltegravir after 600 days, allowing all populations to reach steady state. Then we plot the behavior of 2-LTR in compartment 1 after applying intensification for different diameters as shown in Figure 3.2.

Note the smaller the size of the compartment, the higher the maximum value of 2-LTR in the main compartment after raltegravir intensification. This relation is because smaller compartments diffuse more rapidly into the blood. However, as shown in Figure 3.1, the smaller the site diameter the larger the value of $\hat{R}_{0_2}$ is required to allow viral replication. Figure 3.2 also demonstrates that the smaller the site the greater $\hat{R}_{0_2}$ to find detectable 2-LTR peaks in the main compartment. More specifically $\hat{R}_{0_2}$ has to be in the range between $0.96 - 1$ to get detectable 2-LTR peaks for diameter length from 0.5 to 2 mm. This condition implies that a significant reduction in drug efficacy throughout the site is necessary to explain the transient 2-LTR peaks observed in [11]. It is worth pointing out that the shape of the transient peaks predicted by the model, as shown in Figure 3.2, match the median observed dynamics reported in [11].

3.5 Infected T-Cell turnover rate, 2-LTR Formation and Sanctuary Site Size

To understand the relation between the total tissue volume, individual site size, infected T-Cell turnover rate and predicted 2-LTR peaks in compartment 1, we use the data from the 80,000-trial Monte-Carlo simulation using the priors previously described with values of $\hat{R}_{0_2}$ drawn from the uniform distribution $0.93 - 1.5$ and total tissue volume and individual sphere diameter drawn from the uniform distributions $30 - 499$ mL and $0.1 - 2$ mm respectively. The scatterplot in Figure 3.3 shows the steady state value of the total infected cells turnover rate before intensification versus the maximum value of the 2-LTR transient behavior in blood.

There is a positive, approximately linear correlation between the 2-LTR peak and the T-Cell infection, suggesting that the 2-LTR peak post-intensification is a useful surrogate measurement of cryptic replication. In Figure 3.3, the plot is divided into four regions according to the total tissue volume of all N sites and the diameter of each site. Region I has the largest tissue volume and diameter, region II, large tissue volume but small diameter, region III small tissue volume and large diameter and region IV for small volume tissue and diameter. Larger peaks of 2-LTR positively correlate with greater total tissue volume as well as more infection, and weakly negatively correlate with site diameter, as long as the diameter is above the threshold necessary to allow replication. For total sanctuary site volumes above 30 mL, 2-LTR peaks in compartment 1 are larger than the limit of detection in greater than 95% of the cases. In general, neither cryptic replication nor a 2-LTR peak is present when the site diameter is less than 0.2 mm. This condition is because virus replication cannot be supported in sites smaller than 0.2 mm in diameter; the rate of loss of infected cells to compartment 1 via diffusion makes sustained replication impossible. The median viral load in the center of the sanctuary site is plotted vs. site diameter in Figure 3.4.

We also investigated the case where $\hat{R}_{0_{10}}$ is below 1; that is, only inefficient residual viremia is present in all compartments. Under these conditions, the predicted 2-LTR concentrations in compartment 1 following integrase inhibitor intensification

always follow a monotonic, rather than a transient increase, as shown in Figure 3.5. The maximum predicted value of 2-LTR in compartment 1 is below the limit of detections in normal assays (1.2 2-LTR/$10^6 PBMC$ [47]) for greater than 95% of the trials when $\hat{R}_{0_{10}}$ is below 1.

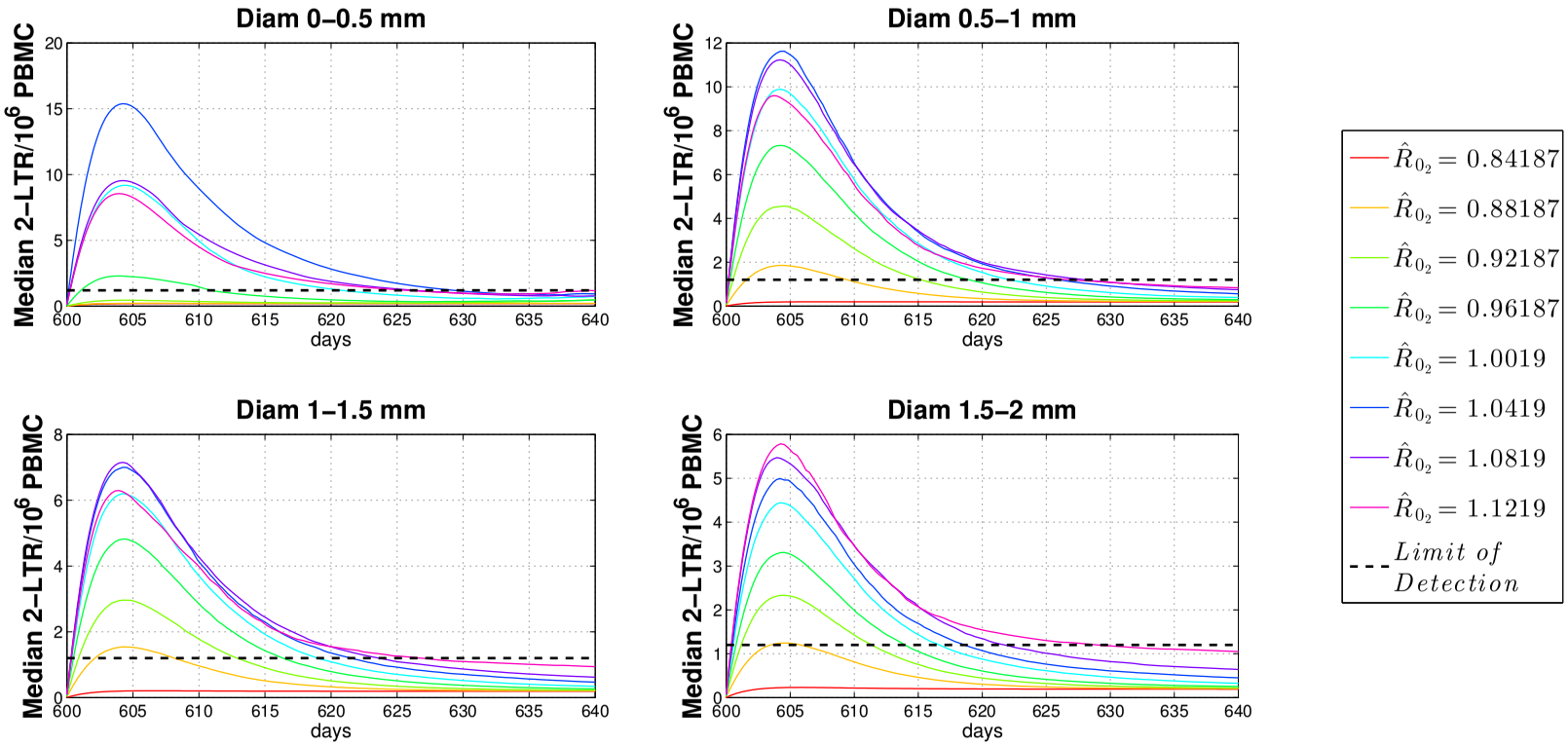

Figure 3.2: 2-LTR Post-intensification varying $\hat{R}_{0_2}$ and diameter size. Average 2-LTR containing cells in the main compartment for a fixed total compartment volume. For diameter length 1, 1.5 and 2 mm the lower $\hat{R}_{0_2}$ bound for detectable peaks approximately over 0.96, and for the smaller case, diameter equal to 0.5mm, the lower bound is $\hat{R}_{0_2} > 1$.

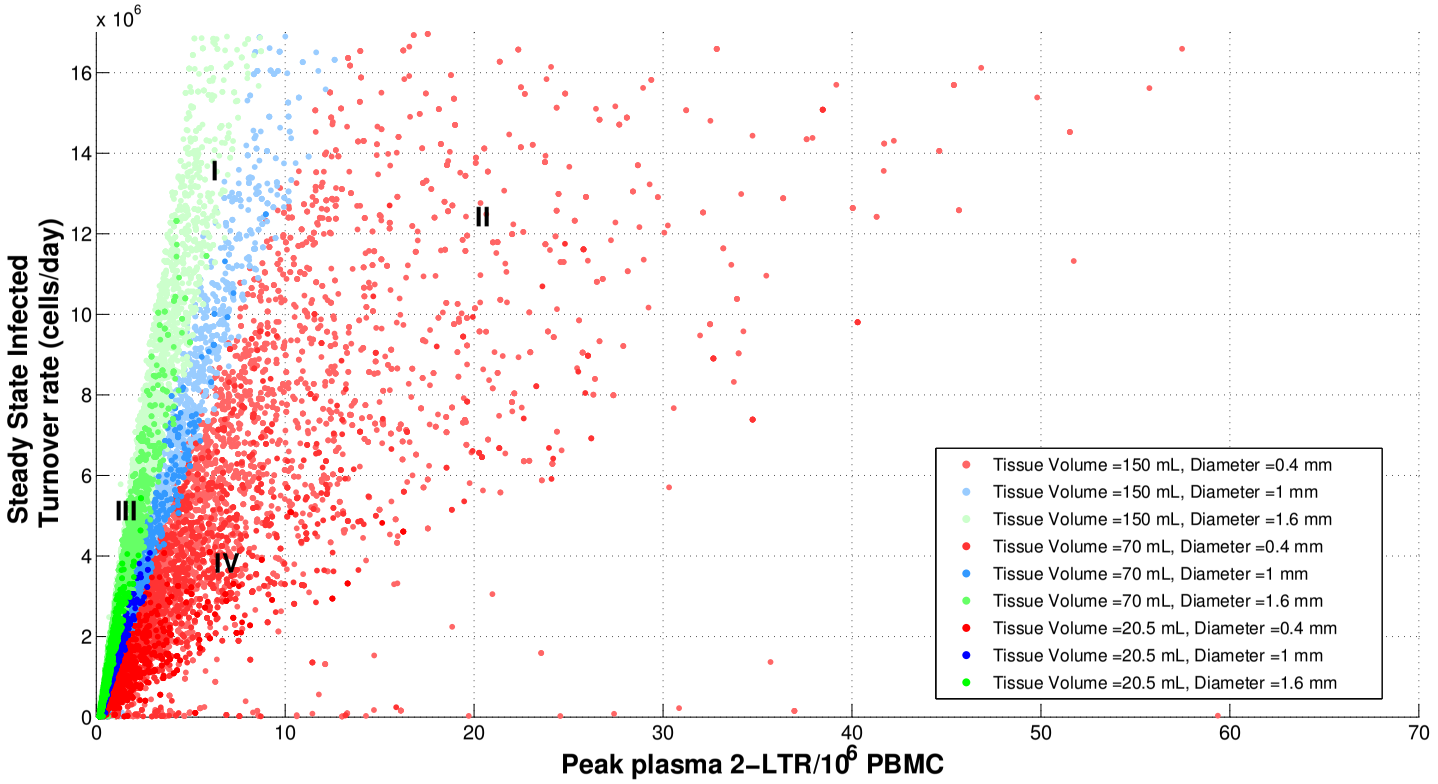

Figure 3.3: Correlation of total infection pre-intensification and 2-LTR peak post-intensification. Regions of the scattered plot depending on the N compartments volume tissue and individual sphere diameter length. Region I, the largest tissue volume and diameter, region II, large tissue volume but small diameter, region III small tissue volume and large diameter and region IV for small volume tissue and diameter.

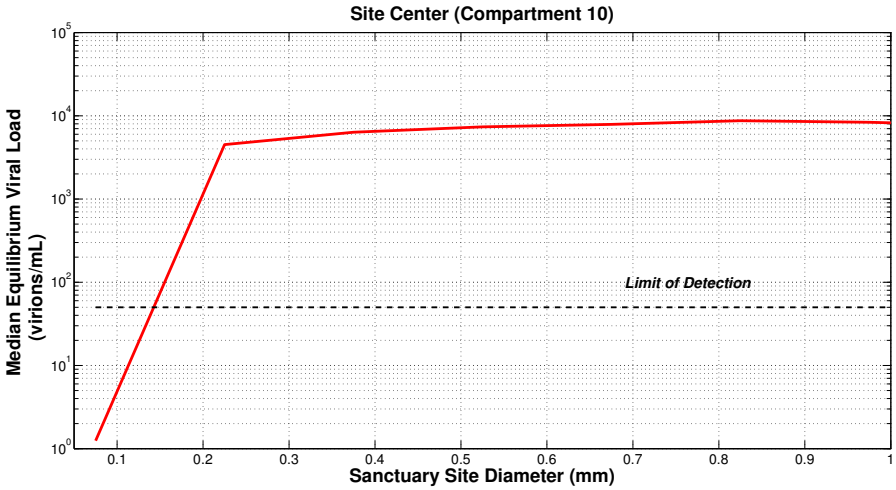

Figure 3.4: Viral load in sanctuary site centers vs. site diameter. Viral replication can not be sustained in sanctuary sites with diameters less than 0.2 mm.

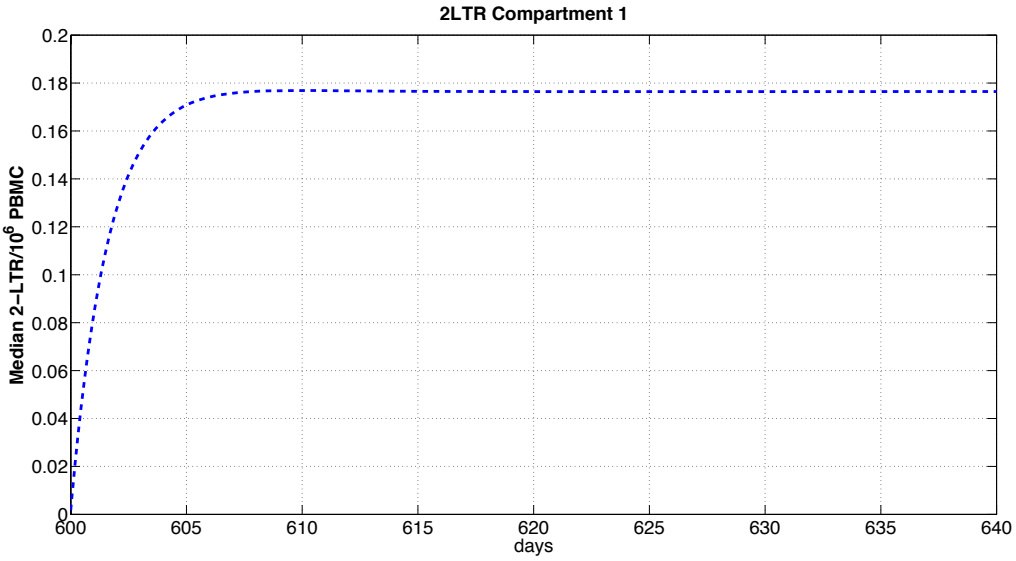

Figure 3.5: 2-LTR behavior when $\hat{R}_{0_{10}} < 1$. Monotonic 2-LTR dynamics in compartment 1 for all parameter values where $\hat{R}_{0_{10}} < 1$. Under these conditions, no transient 2-LTR dynamics are possible.

Chapter 4

CHARACTERIZATION OF CRYPTIC VIREMIA AND 2-LTR FORMATION

4.1 Introduction

As presented in the previous chapter, $\hat{R}_{0_i}$ defines the reproductive ratio of the virus in compartment i prior to raltegravir intensification if the compartments were isolated. We presented how $\hat{R}_{0_2}$ was used to define conditions for cryptic viremia and 2-LTR formation. However, as the compartments are not isolated, the actual reproductive ratio can be greater or smaller depending on the behavior of neighboring compartments. This leads to different values of $\hat{R}_{0_2}$ as the diameter, the parameter that defines diffusion, changes.

Moreover, in the previous chapter we also presented the description of these conditions based in a fixed distribution for drug penetration. Given that, the drug penetration distribution in each compartment is not well understood, possible scenarios could be missing [59, 25, 75, 20, 18]. Furthermore, we also used a fixed value for 2-LTR decay rate as estimated in[49]. However, neglecting trafficking T-cell recirculation could lead to an estimating bias (see next chapter), and a possible broader range for this value, including values estimated in [82, 57, 47], might explain better this decay.

In this chapter, we present a stability analysis to obtain a way to characterize conditions for cryptic viremia taking into account diffusion parameters. Then we present a Monte-Carlo simulation supplementing to the one presented in the previous chapter for the effect of different suboptimal penetration of RTI and PI regimens by varying the drug penetration geometric ratios for each drug. We also include in the simulations different values for 2-LTR decay rate, and demonstrate how that allows for the varying 2-LTR patterns in blood very similar to what was for the 13 patients in the

INTEGRAL study [11]. Based on that, we demonstrate that measurable 2-LTR circles maximum values are correlated to the total infection in the body, however different patterns of drug penetration and reservoir size are presented for each peak.

4.2 Stability Analysis

For this part we compacted the equations (2.1) and (2.2) without the equation for $\mathbf{c}_i$, in one set of equations using the parameter ρ_i, with ρ_1 equal to N, and $\rho_{2,\dots n} = 1$. Thus, the system has the form,

$$\begin{aligned}
\dot{\mathbf{x}}_i &= \lambda - d\mathbf{x}_i - \beta \mathbf{x}_i \mathbf{v}_i (1 - \eta_{RTI}\mathbf{u}_{RTI}\theta_i) \\
&\quad + \rho_i \textstyle\sum_{j \in \mathcal{N}_i} D_{i,j}^{(x)} (\mathbf{x}_j - \mathbf{x}_i), \\
\dot{\mathbf{y}}_i &= \beta \mathbf{x}_i \mathbf{v}_i (1 - \eta_{RTI}\mathbf{u}_{RTI}\theta_i) - a\mathbf{y}_i + y_e \\
&\quad + \rho_i \textstyle\sum_{j \in \mathcal{N}_i} D_{i,j}^{(y)} (\mathbf{y}_j - \mathbf{y}_i), \\
\dot{\mathbf{v}}_i &= \gamma (1 - \eta_{PI}\mathbf{u}_{PI}\varphi_i)\mathbf{y}_i - \omega \mathbf{v}_i \\
&\quad + \rho_i \textstyle\sum_{j \in \mathcal{N}_i} D_{i,j}^{(v)} (\mathbf{v}_j - \mathbf{v}_i).
\end{aligned} \tag{4.1}$$

To do the stability analysis we rewrite the model in (4.1) defining the vector $\mathbf{u}_i \in \mathbb{R}^3$ and the vector field $f(\mathbf{u}_i, \boldsymbol{\mu}_i)$ for $i = 1, ..., n$ as:

$$\mathbf{u}_i = \begin{bmatrix} \mathbf{x}_i \\ \mathbf{y}_i \\ \mathbf{v}_i \end{bmatrix},$$

$$f(\mathbf{u}_i, \boldsymbol{\mu}_i) = \begin{bmatrix} \lambda - d\mathbf{x}_i - \beta \mathbf{x}_i \mathbf{v}_i (1 - \eta_{RTI}\mathbf{u}_{RTI}\theta_i) \\ \beta \mathbf{x}_i \mathbf{v}_i (1 - \eta_{RTI}\mathbf{u}_{RTI}\theta_i) - a\mathbf{y}_i + y_e \\ \gamma (1 - \eta_{PI}\mathbf{u}_{PI}\varphi_i)\mathbf{y}_i - \omega \mathbf{v}_i \end{bmatrix}$$

With $\boldsymbol{\mu}_i = [\theta_i, \phi_i]$ representing the drug penetration. We define also the adjacency matrices $\mathbf{D}_1$, $\mathbf{D}_2$ and $\mathbf{D}_3 \in \mathbb{R}^{n \times n}$ with respective elements $[\mathbf{D}_1]_{i,j} = D_{i,j}^{(x)}$, $[\mathbf{D}_2]_{i,j} = D_{i,j}^{(y)}$ and $[\mathbf{D}_3]_{i,j} = D_{i,j}^{(v)}$, defining how the compartments are connected for each state. For each $\mathbf{D}_k$, by definition, the corresponding Laplacian matrix $\mathbf{L}_k$ has the form,

$$[\mathbf{L}_k]_{i,j} = \begin{cases} \sum_j [\mathbf{D}_k]_{i,j} & i = j \\ -[\mathbf{D}_k]_{i,j} & i \neq j \end{cases}.$$

Thus, if we have the concatenated vector

$$\mathbf{u} = \begin{bmatrix} \mathbf{u}_1 \\ \mathbf{u}_2 \\ \vdots \\ \mathbf{u}_n \end{bmatrix},$$

and the vector field

$$f(\mathbf{u}) = \begin{bmatrix} f(\mathbf{u}_1, \boldsymbol{\mu}_1) \\ f(\mathbf{u}_2, \boldsymbol{\mu}_2) \\ \vdots \\ f(\mathbf{u}_n, \boldsymbol{\mu}_n) \end{bmatrix},$$

we can rewrite the system in equation (4.1) as

$$\dot{\mathbf{u}} = f(\mathbf{u}) - \mathcal{L}\mathbf{u}, \tag{4.2}$$

where $\mathcal{L}$ is defined as,

$$\mathcal{L} = \sum_{k=1}^{3} \mathbf{C}\mathbf{L}_k \otimes \mathbf{E}_k,$$

with $\mathbf{C} = diag\,(\rho)$, the Kronecker product operator $\otimes$, and $\mathbf{E}_k = e_k e_k^{\mathbf{T}} \in \mathbb{R}^{3\times 3}$ with e_k being the k^{th} canonical basis vector of $\mathbb{R}^3$. When y_e is significantly low, a quasi stationary point of $\mathbf{u}$, when there is no infection, is $\bar{\mathbf{u}}_0 = \mathbf{1}_n \otimes \mathbf{w}_0$, with $\mathbf{w_0} = \begin{bmatrix} \frac{\lambda}{d} \\ 0 \\ 0 \end{bmatrix}$ and $\mathbf{1}_n$ the $n \times 1$ vector of ones. Therefore, linearizing the system around this point,

we have a linear system of the form $\dot{\widetilde{\mathbf{u}}} = \mathbf{J}_{\mathbf{u}}\widetilde{\mathbf{u}}$ for $\widetilde{\mathbf{u}}$ near to $\bar{\mathbf{u}}_0$. The matrix $\mathbf{J}_{\mathbf{u}}$ has the form

$$\mathbf{J}_{\mathbf{u}} = \mathbf{J}_f - \mathcal{L}, \tag{4.3}$$

where $\mathbf{J}_f$ is defined as the direct sum of the Jacobi matrices $\mathbf{J}(\mathbf{w}_0, \boldsymbol{\mu}_i)$ for each $f(\mathbf{u}_i, \boldsymbol{\mu}_i)$,

$$\mathbf{J}_f = \bigoplus_{i=1}^{N} \mathbf{J}(\mathbf{w}_0, \boldsymbol{\mu}_i) = \begin{bmatrix} \mathbf{J}(\mathbf{w}_0, \boldsymbol{\mu}_1) & 0 & \cdots & 0 \\ 0 & \mathbf{J}(\mathbf{w}_0, \boldsymbol{\mu}_2) & \ddots & \vdots \\ \vdots & \ddots & \ddots & 0 \\ 0 & \cdots & 0 & \mathbf{J}(\mathbf{w}_0, \boldsymbol{\mu}_n) \end{bmatrix},$$

where assuming that the intensification is not applied, each compartmental Jacobi is,

$$\mathbf{J}(\mathbf{w}_0, \boldsymbol{\mu}_i) = \begin{bmatrix} -d & 0 & -\frac{\beta\lambda(1-\eta_{RTI}\theta_i)}{d} \\ 0 & -a & \frac{\beta\lambda(1-\eta_{RTI}\theta_i)}{d} \\ 0 & \gamma(1-\eta_{PI}\varphi_i) & -\omega \end{bmatrix}.$$

Thus, the stationary point $\bar{\mathbf{u}}_0$ is stable when the real part of the maximum eigenvalue of $\mathbf{J}_{\mathbf{u}}$, σ_{max}, is negative. Therefore we can obtain, for each set of parameters, conditions for stability before numerical simulation of the ODE system, even though we cannot find its analytical solution.

4.3 Monte-Carlo Simulation

From the system in equations (4.1) we run a Monte-Carlo simulation to obtain conditions for cryptic viremia and HIV-1 2-LTR formation when cART is intensified with raltegravir. These conditions are characterized by only one variable, σ_{max}, the maximum eigenvalue of the Jacobi of the linearized system. As in [13], we run $80,000$ simulated patients, and for each one we randomly sample different parameters representing its possible characteristics in a single patient. Specifically, each sample is performed using the following procedure:

4.3.1 Selection of HIV-1/T-Cells Parameter rates HIV-1/T-Cells

Viral dynamic parameters were selected from the marginal posterior distributions estimated in [48]. The selection of a single set of parameters was made following that R_0 before the application of cART is greater than one, and that the basic reproductive ratio after the cART in the range $[0.52 - 0.56]$, close to the MLE estimation in [48]. This conditions assure that cART represses viral replication in the blood to values around $1\frac{virion}{mL}$.

4.3.2 Selection of 2-LTR formation rates

For ϕ, the ratio between intrinsic and raltegravir enhanced likelihood of cDNA integration failure, we use the MLE unidimensional value of 0.002. We use values of k_{II} in the range $[270 - 910]\ \frac{\mu L}{10^6 PBMC}$ as before. For δ we selected uniformly from $0.01 - 0.5$ $\frac{1}{day}$, consequent with previous studies of in vivo rates from $0.047 - 0.47\ \frac{1}{day}$ [82, 57, 47].

4.3.3 Selection of Diffusion related parameters:

We used the same parameter values of the previous chapter. We select the follicle diameter uniformly from 0.01 to 2 mm. For $\hat{D}_{i,j}^{(\cdot)}$, we use $0.1\frac{mm^2}{day}$ and $0.43\frac{mm^2}{day}$ for T-cells and the virus respectively divided by the of each layer layers $\frac{r}{n-1}$, where r is the radius of the follicle site. Finally for the effective diffusivity of T-cells between the main compartment and the follicular site $\hat{D}_{1,2}^{(x)}$, $\hat{D}_{1,2}^{(y)}$ and $\hat{D}_{1,2}^{(c)}$ we use the value $\frac{1}{300}\frac{mm}{day}$.

4.3.4 Selection of drug efficacy and penetration:

The drug efficacy for reverse transcriptase inhibitors (η_{RTI}) and protease inhibitors (η_{PI}) is computed equally from a single parameter η following the relation $(1 - \eta) = (1 - \eta_{RTI})(1 - \eta_{PI})$. The parameter η represent the same as in [48] for a single-compartment model. Therefore we choose this parameter from the parameter set in [48] and with the same condition of the other HIV-1/T-Cells parameters. Given that drug penetration is still not completely understood [75, 18, 20], we define drug penetration of RTI and PI drugs, θ_i and φ_i respectively, as the drug concentration

fraction between each compartment i with respect to compartment 1. This fraction is computed assuming a geometric sequence where $\theta_i = r_1^{i-1}\theta_1$ and $\varphi_i = r_2^{i-1}\varphi_1$. Hence, the parameter of drug penetration for RTI and PI are the ratios of the sequences r_1 and r_2. For both r_1 and r_2, we choose from a unifrom distribution in 0.1 to 0.9, giving average drug pentration ($\bar{\theta}_{LN} = \frac{1}{n-1}\sum_{i=2}^{n}\theta_i$ and $\bar{\varphi}_{LN} = \frac{1}{n-1}\sum_{i=2}^{n}\varphi_i$) from values around 0.01 to 0.7. For the drug penetration of raltegravir (ξ_i), we assume one of the hypothesis suggested in [11, 47, 13] and in the recent work done in [63]that says that this drug is able to penetrate sanctuary sites more efficiently than the other drugs. Therefore, for all compartments, from $i = 1, ..., N$, we do not use a geometric sequence, but instead we use the same drug penetration fraction in the range $0.6 - 0.8$.

4.4 Characterization of Cryptic Viremia

For the steady state when there is no infection, we compute numerically the maximum real eigenvalue of the system σ_{max}, conditioning the cases when the virus is able to replicate (see previous section). Assuming suboptimal drug penetration of RTI and PI regimens, that is for $(\theta_1, \varphi_1) = (1, 1)$ and $(\theta_{2,...,n}, \varphi_{2,...,n})$ smaller than 1, we find cases when there is sustained replication in the remote compartments but with no replication in the compartment that represents the blood. The Fig. 4.1a depicts the value of the steady state viral load before raltegravir intensification from the Monte-Carlo simulation for different values of σ_{max} in the main compartment and the most remote compartment. Notice the instability behavior when σ_{max} becomes positive, especially in the most remote compartment. In general, the steady state in the most remote compartment can reach up to $10^4 \frac{virions}{mL}$ despite the mean steady state viral load in the measurable compartment being just $1\frac{virion}{mL}$. Notice this behavior is from simulations for all different ranges of the parameters selected. Specifically Fig. 4.1b shows the steady state viral load in compartment 1 follows a log-normal distribution with mean $1.294\frac{virions}{mL}$. This value is consistent with all literature presented before about the capacity of cART in suppressing viral load in the blood. In our case, however, it includes high viral load in lymph node compartments. This phenomena is called

cryptic viremia, and it is characterized by σ_{max}.

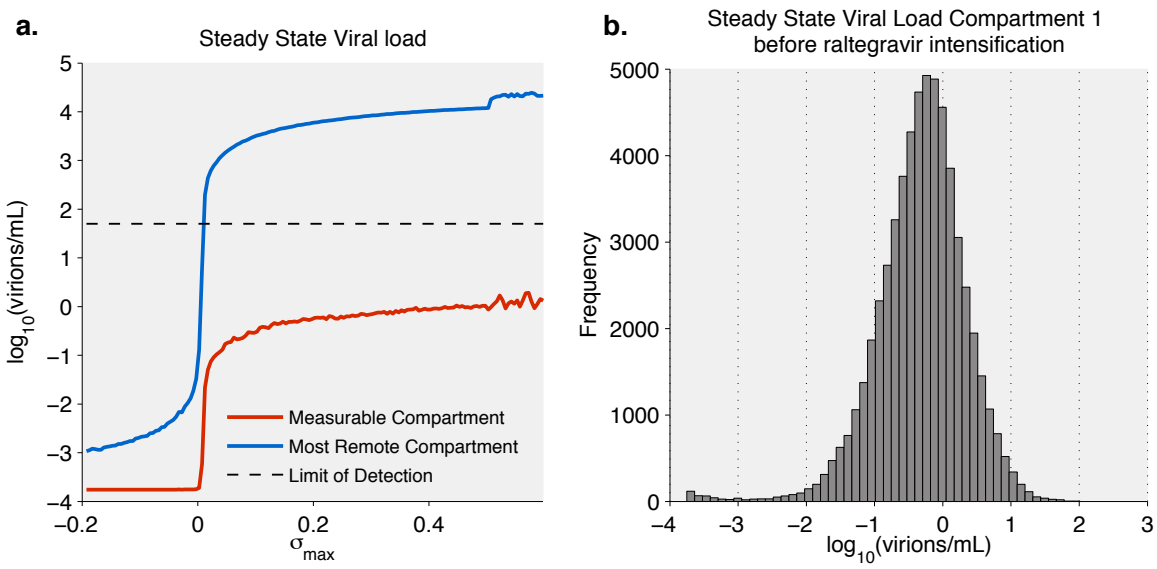

Figure 4.1: Characterization of cryptic viremia. On the left, steady state viral load in compartment one and the most remote compartment in log-scale vs. σ_{max} before raltegravir intensification. Notice that viral load in the most remote compartment goes over the limit of detection for values σ_{max} greater than zero despite viral load in the first compartment is below those limits. On the right, a histogram of the steady state viral load in compartment one before raltegravir intensification. Notice that the average value is around 1 $\frac{virion}{mL}$.

4.5 Suboptimal Drug Penetration and Reservoir Size Conditions for Cryptic Viremia

As $\sigma_{max} > 0$ represents cryptic viremia, our interest is clinical-relevant and possible measurable parameter combinations in which the system crosses this treshold. First, we study different LN-tissue/blood RTI-PI concentration ratios for combinations of the remaining parameters (see further methods for details about parameter selection) so that $\sigma_{max} > 0$. Fig. 4.2a shows the relationship between the average RTI and PI ratios inside the lymph nodes ($\bar{\theta}_{LN}$ and $\bar{\varphi}_{LN}$ respectively), with respect to σ_{max} values. The red part in the figure represents the combinations for σ_{max} greater than

zero. In general, either RTI or PI, their average penetration must be less than 0.55 to sustain cryptic viremia. However, for either RTI or PI, if its ratio increases, the other drug ratio has to decrease almost linearly to sustain replication inside the lymph node and be considered a sanctuary site for cART. These drug penetration results are not inconsistent with previous data as reviewed in [20, 75] where their findings indicated ratios around 0.4 for RTIs and from 0.5 to 0.2 for PIs. Here we find that cryptic viremia is possible when total drug efficiency in lymph nodes is very low.

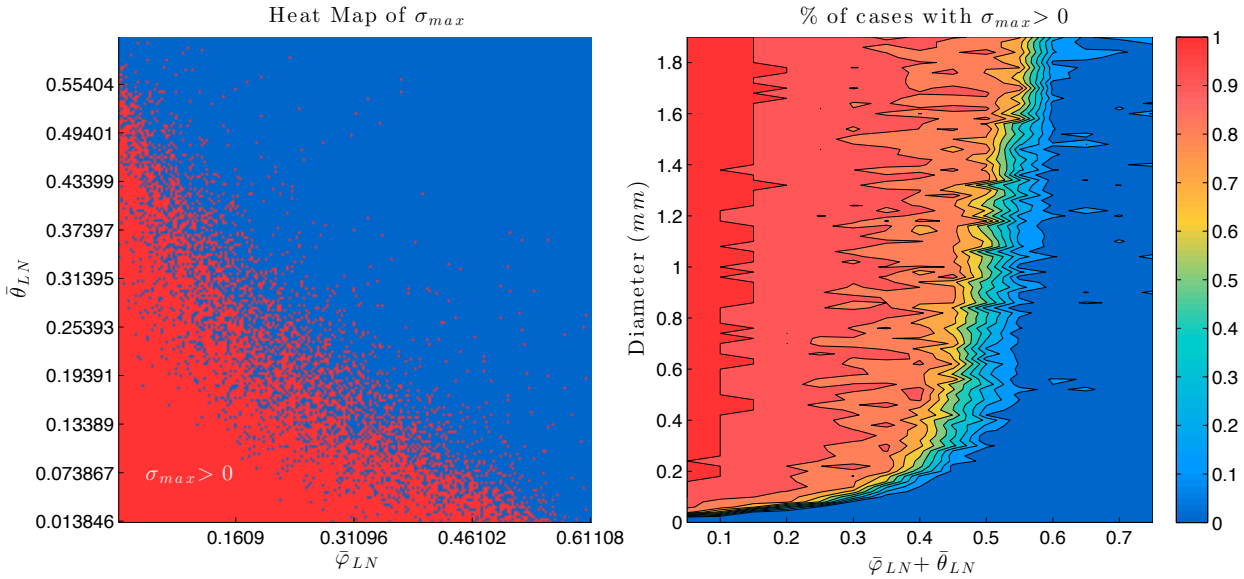

Figure 4.2: Conditions for cryptic viremia. On the left, a heat map for the values of σ_{max} in relation with the average RTI and PI drug penetration $\bar{\theta}_{LN}$ and $\bar{\varphi}_{LN}$. There is almost a linear relationship $\bar{\theta}_{LN} + \bar{\varphi}_{LN} \lesssim 0.5$ to have cryptic viremia for any value of the other parameters. On the right, a contour graph presenting the relative frequency for $\sigma_{max} > 0$ for different values of the diameter of the sanctuary sites (in mm) and total drug penetration $(\bar{\theta}_{LN} + \bar{\varphi}_{LN})$. In general, very low total drug penetration, with diameters over 0.2 mm guarantee $\sigma_{max} > 0$.

A second relevant parameter is the size of the anatomical reservoir. Mathematically this size affects the moving rates of T-cells and virions among compartments. In our model $D_{i,j}^{(\cdot)} = \hat{D}_{i,j}^{(\cdot)} \frac{A_{i,j}}{V_i}$ where $A_{i,j}$ represents the surface area between layers i and j

inside the lymph node, V_i the volume of layer i and $\hat{D}_{i,j}^{(\cdot)}$ the permeability of T-cells or the virus between compartment i and j. Hence the critical parameter for reservoir size is the diameter of the lymph node follicle. Based on 80000 simulations, we compute the proportion of cases when σ_{max} was greater than zero with respect to the diameter and the total drug penetration $\bar{\theta}_{LN} + \bar{\varphi}_{LN}$. Fig. 4.2b shows that regardless the diameter, if total drug penetration $\bar{\theta}_{LN} + \bar{\varphi}_{LN}$ is greater than 0.6, the percentage of cases to have cryptic viremia is always less than or equal to 10%. On the other hand, only if the total drug penetration $\bar{\theta}_{LN} + \bar{\varphi}_{LN}$ is smaller than 0.1 and the diameter is greater than 0.2 mm it is possible to have cryptic viremia in nearly 100% of the cases. As total drug penetration increases, the probability to have cryptic viremia decreases, but the percentages are higher for larger diameters. In general, the likelihood to have viral replication in lymph nodes follicles with diameters greater than 0.2 mm and with total drug penetration smaller than 0.5 is around 95%.

Larger follicular diameters have been reported previously in patients under cART with no detectable blood viral load. For instance, the work done in [61] presented hyperplastic follicles even up to 1 mm for 3 of 9 patients after six months of treatment. In fact, a study reported in [1] found for some patients under cART, hyperplastic follicles with areas oscillating up to 1.23 mm^2 in 12 months and 0.33 mm^2 in 36 months. These results correspond approximately to diameters from 0.65 to 1.25 mm, in the range of possible cryptic viremia according to the model. Therefore, we suggest, if there is sufficiently low drug penetration inside lymph nodes, follicles with diameters from 0.65 to 1.25 mm could sustain viral replication.

4.6 Raltegravir Intensification and 2-LTR Containing Cells Half-life

Cryptic viremia leads to 2-LTR formation when raltegravir is added to the regimen. When the system reaches a steady state we model raltegravir intensification by adding the term $(1 - \eta_{II}\mathbf{u}_{II}\xi_i)$ in equation (4.1), and with the state $\mathbf{c}_i$ representing 2-LTR containing cells in each compartment as in [13]. The equations for the new state, proposed in [47], present the density dependent formation of 2-LTR circles, its clearance

rate and how they move between compartments assuming the same configuration for recirculation inside lymph nodes as before. Thus the system has the form presented in equation 2.2 in chapter 2.

Given the concerns of possible overestimation of the 2-LTR half-life in previous studies, the relevant parameter for analysis is the 2-LTR containing cells decay rate δ. For that reason we study the 2-LTR behavior in compartment 1 ($\mathbf{c}_1$) for different values of δ. For each sample, we first compute what is the likelihood to fit the data for each patient presented in Buzon et. al. [11]. Based on the work in [49, 47], the likelihood model has the form,

$$\mathcal{L}(\mathbf{c}_1|m_{ik}) = \begin{cases} f_{\mathcal{LN}}(m_{ik}, \mathbf{c}_1(t_{i,k}), \sigma^2(\mathbf{c}_1(t_{i,k}))), & m_{ik} > 1.2 \\ F_{\mathcal{LN}}(m_{ik}, \mathbf{c}_1(t_{i,k}), \sigma^2(\mathbf{c}_1(t_{i,k}))), & m_{ik} = 1.2 \end{cases}, \tag{4.4}$$

Table 4.1: Best fits Monte-Carlo simulation and 2-LTR decay rate estimation. Parameter values for best fit to INTEGRAL study data from Monte-Carlo simulation for the first 5 columns (*Patient 10 was discarded for the computation of the median).

Patient	Diameter (mm)	$\bar{\theta}_{LN}$	$\bar{\varphi}_{LN}$	σ	δ
1.	0.8689	0.3665	0.1716	0.0373	0.0973
2.	1.0870	0.0503	0.1135	0.2850	0.4817
3.	1.3178	0.1640	0.1640	0.1582	0.1875
4.	1.0066	0.4628	0.0525	0.0533	0.0426
5.	0.1250	0.0960	0.0225	0.2437	0.2974
6.	0.1547	0.0234	0.0213	0.3788	0.4342
7.	1.3774	0.1848	0.0368	0.2677	0.0553
8.	1.6716	0.0671	0.1009	0.2470	0.0485
9.	1.0728	0.0842	0.4334	0.0128	0.0318
10.	0.9831	0.0555	0.3616	-0.1517	0.0280
11.	1.9138	0.0470	0.6096	0.0982	0.0291
12.	1.9138	0.0470	0.6096	0.0982	0.0291
13.	1.9700	0.0824	0.5129	0.0605	0.0436
Median*	1.2024	0.0833	0.1387	0.1282	0.0519

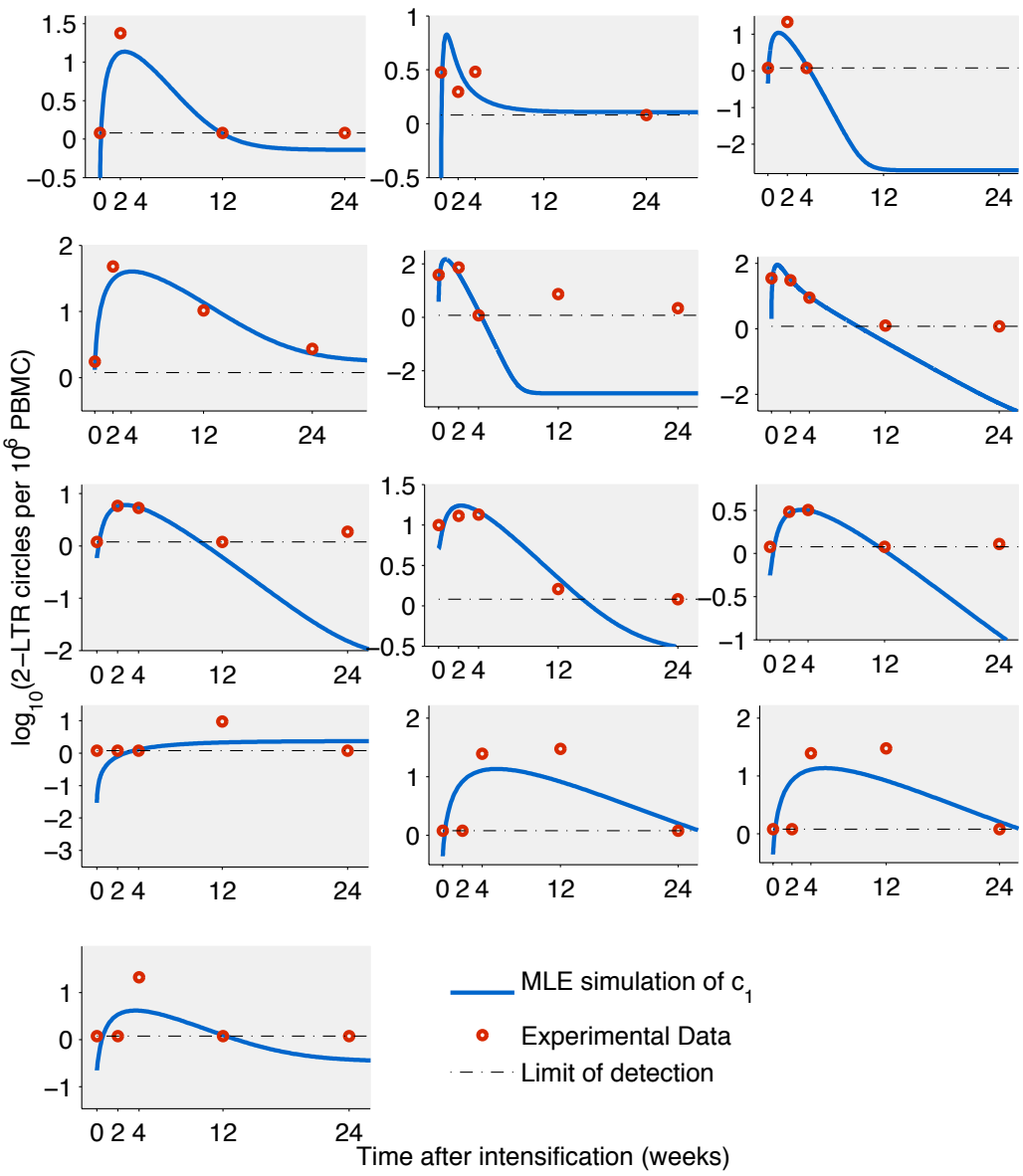

Figure 4.3: Best fits from MC simulation. Best fits from the 80,000 samples in the Monte-Carlo simulation for the 2-LTR circles per million data after raltegravir intensification from the study in [11]. For all the patient set of data σ_{max} is greater than zero (except for patient 10) directing cryptic viremia as the cause of the transient behaviors.

Fig. 4.3 presents the maximum likelihood estimation (MLE) of $\mathbf{c}_1$ generated from the data for each of the simulated patients. The relevant parameters for the MLE

for each patient if presented in Table 4.1. Fig. 4.3 shows a very good fit of the data to the model. The fits are comparable to the ones done before in [47]. However, they have contrasted diferences in the value of 2-LTR per 10^6 PBMC clearence rate δ. In this case the median of δ is 0.0519 days^{-1}, almost an order of magnitude smaller than our previous estimation of 0.46 days^{-1}, but more in agreement with previous experimental estimation for 2-LTR half-life. Notice in table 4.1 for all the cases when simulation leads to 2-LTR transient behavior (all except patient 10) the value of σ_{max} is always greater than zero corresponding to sustained viral replication inside the LNs. Relative to the results in the previous section, we compute the average corresponding areas for the best data fits with 0.92 mm^2, in agreement with the mentioned ranges in [1]. Thus, we have demonstrated that HIV ongoing replication in hyperplastic follicles with poor penetration of cART, is a possible scenario to produce 2-LTR circles patterns in PBMC after raltegravir intensification as in the studies in [11] and [38].

4.7 2-LTR Formation and Pre-intensification de-novo Infection Rate

Given that σ_{max} implies criptic viral replication under cART and could lead to 2-LTR circles in PBMC, the transient response of 2-LTR circles after raltegravir intensification is related to recent infected cells turnover rate before raltegravir intensification. As Fig. 4.4a presents, the maximum value of 2-LTR circles has a positive correlation coefficient of 0.8025 on a logarithmic scale with respect to the total infection turnover rate when $\sigma_{max} > 0$. Specifically, for peaks over the limit of quantification (1.2 2-LTR circles per 10^6 PBMC [47]), the total infection goes from 10^5 to 10^8 infected cells per day. However, each 2-LTR circles peak value is correlated to a range of a steady state infected cells per day prior to intensification. In this range, the distribution of the follicular site diameter, the distribution total LN tissue, and the distribution of RTI/PI penetration in the sites change. Fig. 4.4b-d present those distributions for 2-LTR per 10^6 PBMC with values around 1.2, 10 and 70. In average, the diameter of the follicular site is negatively correlated respect to the maximum value of 2-LTR circles. The minimum value was about 0.2 mm for a peak up to 100 2-LTR circles per

10^6 PBMC. Conversely, the total LN tissue volume is positively correlated with 2-LTR circles peak. When it has a lower number, around the limit of quantification, the total tissue volume is at least 30 mL to have detectable 2-LTR circles in PBMC. RTIs and PIs average penetration in the LN sites have similar distributions. As the maximum amount of 2-LTR circles per 10^6 PBMC decreases the drug penetration distribution get broader although with very close medians, around 0.1. Therefore, it is less likely to have higher drug penetration when the 2-LTR circles peak increases.

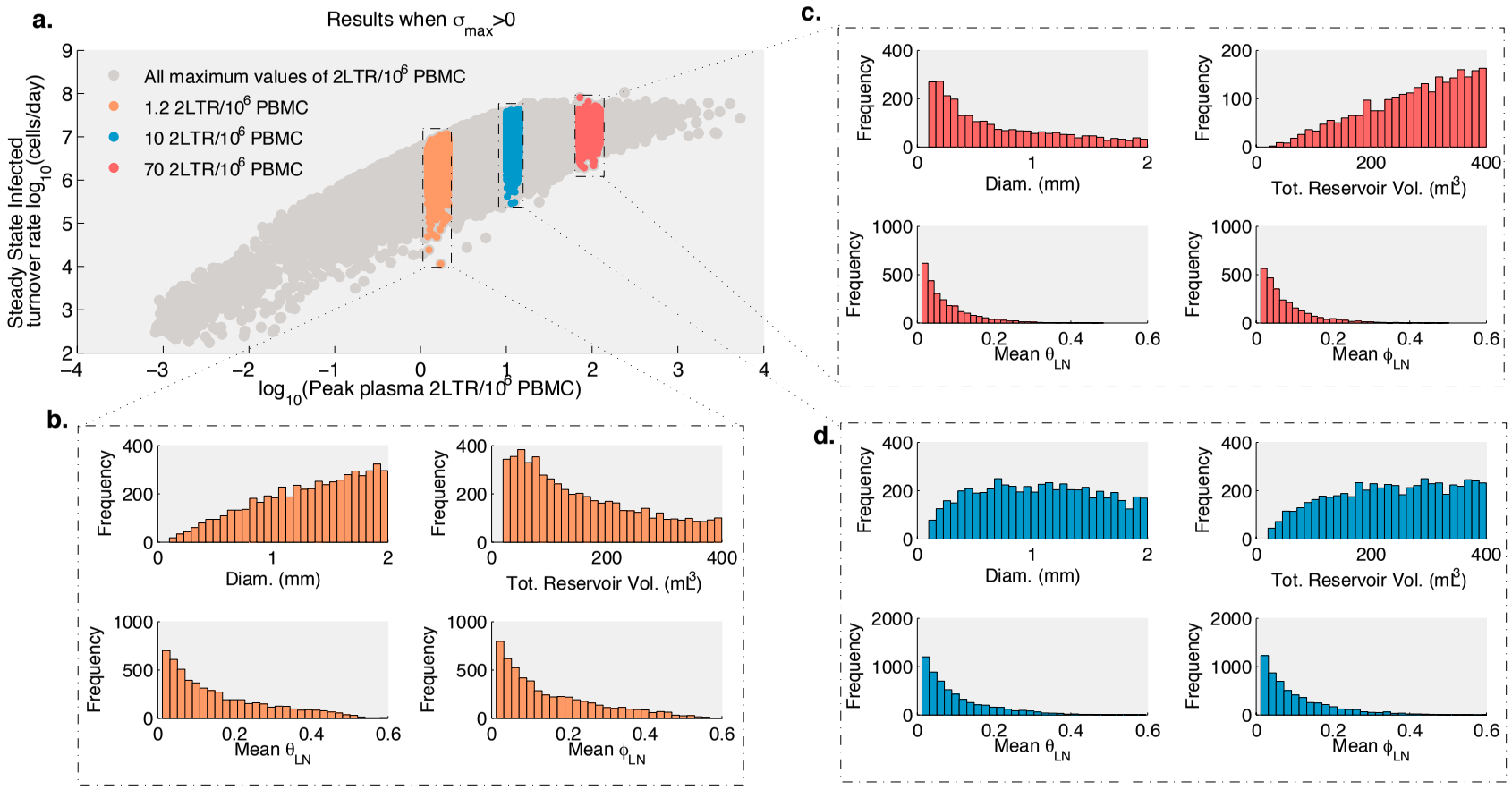

Figure 4.4: Relation between 2-LTR circles and infected cells. Section a. presents a scatter graph presenting the relationship between the maximum value of the 2-LTR transient response in compartment one and the number of infected cells per day in all compartments. Sections b-d present histograms of the diameter, total tissue volume and drug penetration when the 2-LTR maximum value in compartment one is 1.2, 10 and 70 2-LTR circles per million cells respectively.

Chapter 5

COMPUTATION OF 2-LTR HALF-LIFE BIAS

5.1 Introduction

2-LTR circles in-vivo are only reliable markers if they have a short half-life. Experiments in-vivo shows that 2-LTR circles are labile with short half-life from few days up to one month [73, 82, 57, 47]. Plausible reasons for in-vivo short-half life are based on physiological factors as host T-cells half-lives, cell division or cell migration. Previously, short half-life of 2-LTR circles from Buzon study was estimated, consistent with previous estimates in-vivo [47]. This study leads to the conclusion that the 2-LTR transient behaviors are most likely due to HIV-1 cryptic replication in sanctuary sites where RAL penetrates.

Furthermore, in the previous chapter we presented that 2-LTR transient behavior in the blood can have decay rates with an average of 0.05 days^{-1} when the spatial dynamics of sanctuary sites hypothesis is considered. This result suggests that previous estimations of 2-LTR half-life, as done in [47], fitting INTEGRAL study data to a single-compartment model, can incur into a bias due to neglection of spatial dynamics. Thus, there is concern that, by neglecting T-cells recirculation, 2-LTR circles half-life might be underestimated.

In this chapter, therefore, we analyze the bias introduced by the model mismatch by identifying the parameters of a simple model using simulated data generated from the compartmental model. The simulated data is corrupted by the measurement noise process described in [49]. The identified parameter values are then correlated to the parameter values used to generate the simulated data. We present the design for

the creation of virtual clinical trials and a description of the model used, the comparison of the maximum likelihood estimate from the simulated data and the posterior distributions.

5.2 Selection of Virtual Patients using INTEGRAL Study Data

To select the virtual patients we take the results of the Monte Carlo simulation from the previous chapter. Then, for each set of parameters of the simulation, we compute the likelihood of a measured 2-LTR concentration of a patient i at time k given the modelled 2-LTR concentration $\mathbf{c}_1$ after raltegravir intensification using the same model of uncertainty proposed in [49, 47]. The model is constructed under an analysis of PCR technique to amplify the samples performed in [11]. This procedure adds a lognormal uncertainty in the 2-LTR samples that increase as the expected number decreases, and it contraints the samples to a limit of quantification equivalent to 1.2 2-LTR/10^6 PBMC (for more details see [49, 47]). Thus, the model has the form,

$$\mathcal{L}(\mathbf{c}_1|m_{ik}) = \begin{cases} f_{\mathcal{LN}}(m_{ik}, \mathbf{c}_1(t_{i,k}), \sigma^2(\mathbf{c}_1(t_{i,k}))), & m_{ik} > 1.2 \\ F_{\mathcal{LN}}(m_{ik}, \mathbf{c}_1(t_{i,k}), \sigma^2(\mathbf{c}_1(t_{i,k}))), & m_{ik} = 1.2 \end{cases}, \tag{5.1}$$

where $f_{\mathcal{LN}}(\cdot)$ and $F_{\mathcal{LN}}(\cdot)$ denote the PDF and CDF of the lognormal distribution, and the variance $\sigma(c)$ has the form

$$\sigma(c) = 10^{-0.21-[0.24\times log_{10}(c)]}. \tag{5.2}$$

With this model, we use the 13 patients 2-LTR transient behavior data after raltegravir intensification of the INTEGRAL study presented in [11]. Using this data, we compute the maximum likelihood to have each patient data m_i given the $\mathbf{c}_1$ for the time after raltegravir intensification of each result from the Monte Carlo simulation. Thus, the result is a set of 13 time-series of $\mathbf{c}_1$ simulations.

5.3 Creation of Virtual Data

For the 13 best fits of the simulations $\mathbf{c}_1$ to each patient data, using the model in (5.7), we create two different 2-LTR circles per 10^6 PBMC sampling schedules related to the ones made in [11] and [38].

We assume that the measurements are sampled from the virus in the first compartment of the model in equation 2.1. The original study data were HIV-1 RNA PCR measurements; we assume the uncertainty related to that technique that has a log-normal distribution as described above. Finally, we assume that each measurement is independent from patient to patient, and from time to time. This yield to the model of 2-LTR measurements, as proposed in [47]:

$$\begin{aligned} m_i(t_{i,k}) &= \max\{\mathbf{c}_1(t_{i,k} - t_0, \mathbf{p}) + e_{i,k},\ 1.2\} \\ e_{i,k} &\sim \mathcal{LN}(0, \sigma^2(\mathbf{c}_1)) \end{aligned} . \tag{5.3}$$

In this model $m_i(t_{i,k})$ represents the simulated measurement of 2-LTR per 10^6 PBMC for patient i at time t_{ik} after time of raltegravir intensification t_0. The noise $e_{i,k}$ is assumed log-normally distributed with zero-mean sample variance, where $\sigma(\mathbf{c})$ is defined as in equation (5.2) [49].

Using this model of uncertainty and for each virtual patient $\mathbf{c}_1$ the two sampling schedules are as follows. The first one is exactly the same made in Buzon et al. [11] where the sampling was done in weeks 0, 2, 4, 12 and 24 after raltegravir intensification. This schedule was chosen to compare the bias produced in the procedure made in [47]. In the second schedule the samples are in weeks number 0, 0.5, 1, 1.5, 2, 5, 8, 12 and 24 after raltegravir intensification. This sampling includes measurements as scheduled in [38] and following a feasible schedule for real patients to avoid blood drawn: sampling no more frequently than twice weekly, and with fewer than 10 total samples over a 20-week period. As presented in equation (5.3), to include the limit of quantification for 2-LTR, each sample was virtually left censored to 1.2 [49]. We hypothesize that this second schedule decrease the bias as having more information in the first weeks were the transient part of the 2-LTR behavior happens.

5.4 Model to Fit

Using the simulated data, we want to estimate the parameters of the following model,

$$\begin{aligned} \dot{\mathbf{y}} &= (1-\eta_{II}\mathbf{u_{II}})aR\mathbf{y} - a\mathbf{y} + \mathbf{y_e} \\ \dot{\mathbf{c}} &= \phi k_{II}(1-\eta_{II}\mathbf{u_{II}})aR\mathbf{y} + k_{II}\eta_{II}\mathbf{u_{II}}aR\mathbf{y} - \delta\mathbf{c}. \end{aligned} \tag{5.4}$$

As presented in [47] this model is the simplest way to describe the same dynamics of the spatial model. Assuming that the system has reached an steady state before raltegravir intensification, the behavior of 2-LTR containing cells after raltegravir intensification has the form,

$$\begin{aligned} \mathbf{c}(t) &= \mathbf{c}(\infty) + (\mathbf{c}(0) - \mathbf{c}(\infty))\, e^{-\delta t} \\ &\quad + \mathbf{c}(\infty)\tfrac{\delta\eta_{II}R}{(1-R)(a(1-(1-\eta_{II}\mathbf{u_{II}})R)-\delta)}(e^{-\delta t} - e^{a(1-(1-\eta_{II}\mathbf{u_{II}})R)t}). \end{aligned} \tag{5.5}$$

with

$$\begin{aligned} \mathbf{c}(0) &= \tfrac{k_{II}y_e\phi R}{\delta(1-R)}, \text{ and} \\ \mathbf{c}(\infty) &= \tfrac{k_{II}y_eR(\phi+\eta_{II}-\phi\eta_{II})}{\delta(1-(1-\eta_{II}\mathbf{u_{II}})R)}. \end{aligned} \tag{5.6}$$

The parameters of the model are described in previous chapters, and the model with its respective observability analysis is presented in [47]. The implementation of the Bayesian estimation is described below, and the posterior distributions estimated by the MCMC technique is reported.

5.5 MCMC Methodology

We implemented the same MCMC methodology as in [47] to estimate the 2-LTR decay rate of the single-compartment model of equation (5.6), using a Metropolist-Hasting algorithm. Given the simulated data generated for each virtual patient $i = 1, 2, ..., 13$, and measurements taken at times t_{ik} for $k = 1, ..., n_i$, we use a hierarchical mixed-nonlinear effects Bayesian approach to estimate the parameters, with fixed and inter-patient variation. To define the model let $\mathbf{p}_i$ denote the set of parameter values

for patient i in model (5.4). Also, let $\mathbf{c}(t_{i,k}, \mathbf{p}_i)$ be the solution of $\mathbf{c}(t)$ in (5.6) for the i^{th} patient at time t_{ik} using parameters $\mathbf{p}_i$. Further we assume measurements with log-normal distribution as

$$m_{ik}(t_{ik}) \sim \mathcal{LN}(\mathbf{c}(t_{i,k}, \mathbf{p}_i), \sigma^2(c_{ik})),$$

with $\sigma(\cdot)$ defined in equation (5.2). Then, taking into account the limits of quantification of HIV-1 PCR measurements, we use a likelihood function for a measured virion concentration m_{ik} given the set of parameters of patient i, $\mathbf{p}_i$, using the Tobit of censored measurements approach as presented in [47]. Thus, the first stage of the model has the form

$$\mathcal{L}(\mathbf{p}_i|m_{ik}) = \begin{cases} f_{\mathcal{LN}}(m_{ik}, \mathbf{c}(t_{i,k}, \mathbf{p}_i), \sigma^2(c_{ik})), & m > 1.2 \\ F_{\mathcal{LN}}(m_{ik}, \mathbf{c}(t_{i,k}, \mathbf{p}_i), \sigma^2(c_{ik})), & m = 1.2 \end{cases}, \tag{5.7}$$

where $f_{\mathcal{LN}}(\cdot)$ and $F_{\mathcal{LN}}(\cdot)$ denote the PDF and CDF of the lognormal distribution.

As in [47] we reparametrized a parameter $A = \frac{k_{II} y_e}{\delta}$. Moreover, we assume for the parameters δ and ϕ fixed effects and for R, η_{II} and A random effects with inter-patient variation. For the prior distribution of the parameters, we use similar prior distributions, with a previous simulated annealing optimization procedure as in [47]. The prior distributions are,

$$\left\{ \begin{array}{rcc} \delta & \sim & \mathcal{U}(0,1) \\ \phi & \sim & \mathcal{LN}(0.002, 1) \\ R & \sim & \mathcal{U}(0,1) \\ \eta_{II} & \sim & \mathcal{U}(0,1) \\ A & \sim & \mathcal{LN}(\mu_i, 2.5) \end{array} \right\}, \tag{5.8}$$

where $\mathcal{U}$ and $\mathcal{LN}$ represent the uniform and log-normal distribution and μ_i represents the mean value obtained for each patient by a prior simulated-annealing-based optimization.

Thus, with the definition of the likelihood and the priors from equations (5.7) and (5.8), we compute the posterior distribution with MCMC using Metropolis Hasting algorithm to update in each iteration the vector $\mathbf{p}_i$ until the Markov chain converges. Finally, we compute the bias by subtracting the median of the posterior distribution of $\hat{\delta}$ for all patients and the median of δ to generate the virtual data $\mathbf{c}_1$.

5.6 Results

From here we will use $\hat{\delta}$ to describe the estimated value of the decay rate and $\hat{\phi}$ for the estimated value of ϕ by the MCMC method. For both sampling schedules described in the previous section, the estimated 2-LTR decay rate $\hat{\delta}$ has a significant bias with respect to the median value used to simulate the virtual data. However, the virtual sampling using Buzon schedule [11] leads to a higher bias than the more frequent schedule proposed. As presented in table 5.1, the median value of $\hat{\delta}$ were 0.25 day^{-1} and 0.17 day^{-1}, for the Buzon-based and more frequent schedule respectively. Figure 5.1 and 5.2 present the log-likelihood of the MCMC estimates for the last 10^6 iterations for each virtual patient and for the total likelihood of all of them. As presented in the figures, these behaviors correspond to a converged chain. The fitting to the virtual data for the maximum likelihood estimates for each patient is presented in figures 5.7 and 5.8.

Table 5.1: Results for $\hat{\delta}$ and $\hat{\phi}$. Median estimate and standard deviation of the posterior distributions of $\hat{\delta}$ and $\hat{\phi}$ for the Buzon-based and more frequent schedule.

	$\hat{\delta}$ $(days^{-1})$		$\hat{\phi}$	
	Median	Std.	Median	Std.
Buzon-based Sampling Schedule	0.25	0.49	0.0057	0.35
More Frequent Sampling Schedule	0.17	0.24	0.01	0.3

In figure 5.3 and 5.4 the posterior distribution of the shared parameter $\hat{\delta}$ is presented for Buzon and the more frequent schedule respectively. Both of them are approximately log-normal distributions. For the Buzon-based schedule, the posterior

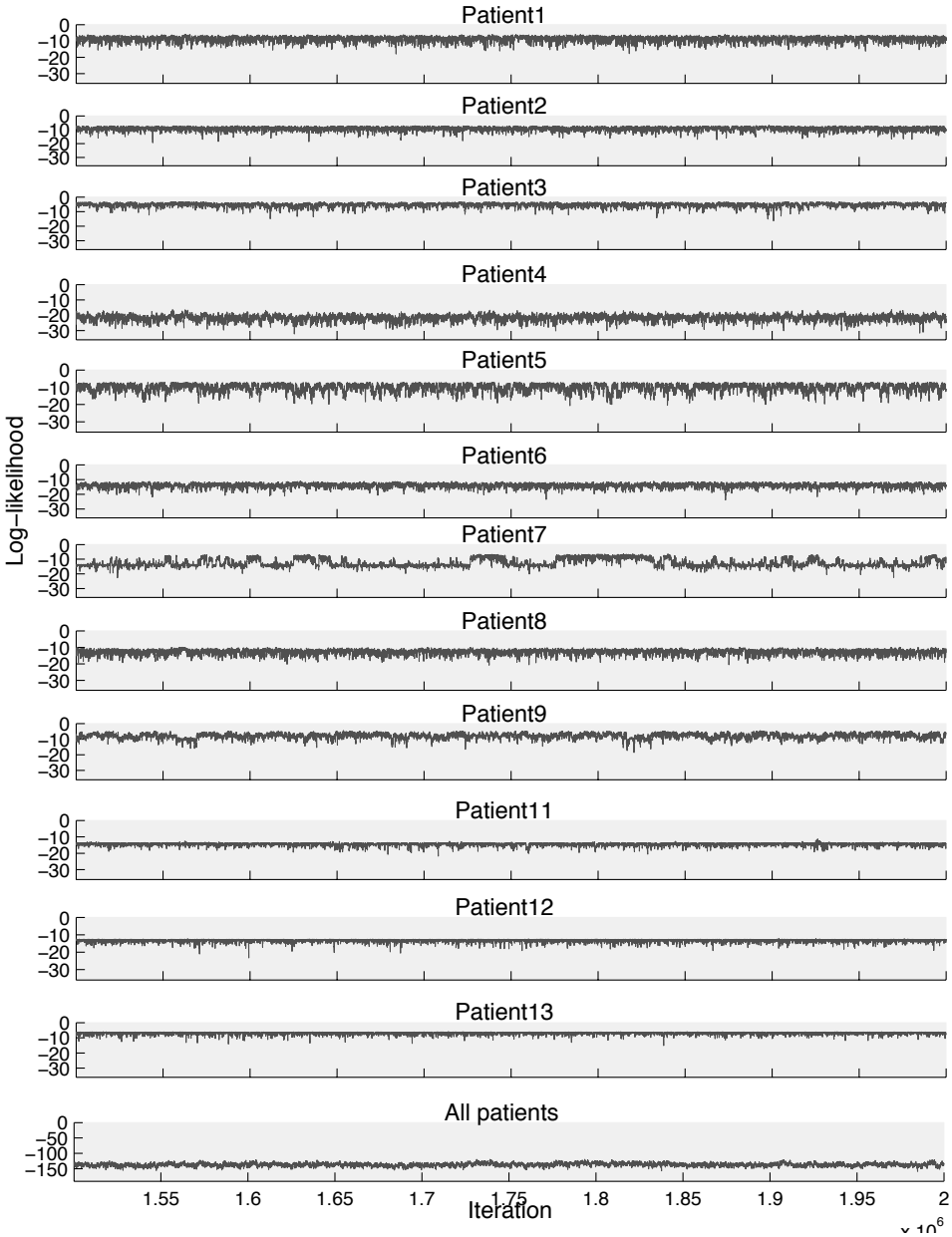

Figure 5.1: Log-likelihood of estimates using Buzon-based schedule. This figure presents the log-likelihood of the MCMC estimates for each virtual patient and all set of patients for the last 10^6 iterations of the algorithm. Notice that this corresponds to a converged Markov chain

distribution of $\hat{\delta}$ has a median of 0.25 days^{-1} and a standard deviation of 0.49 days^{-1}. The distribution of $\hat{\delta}$ for the more frequent schedule has a median of 0.17 days^{-1} with

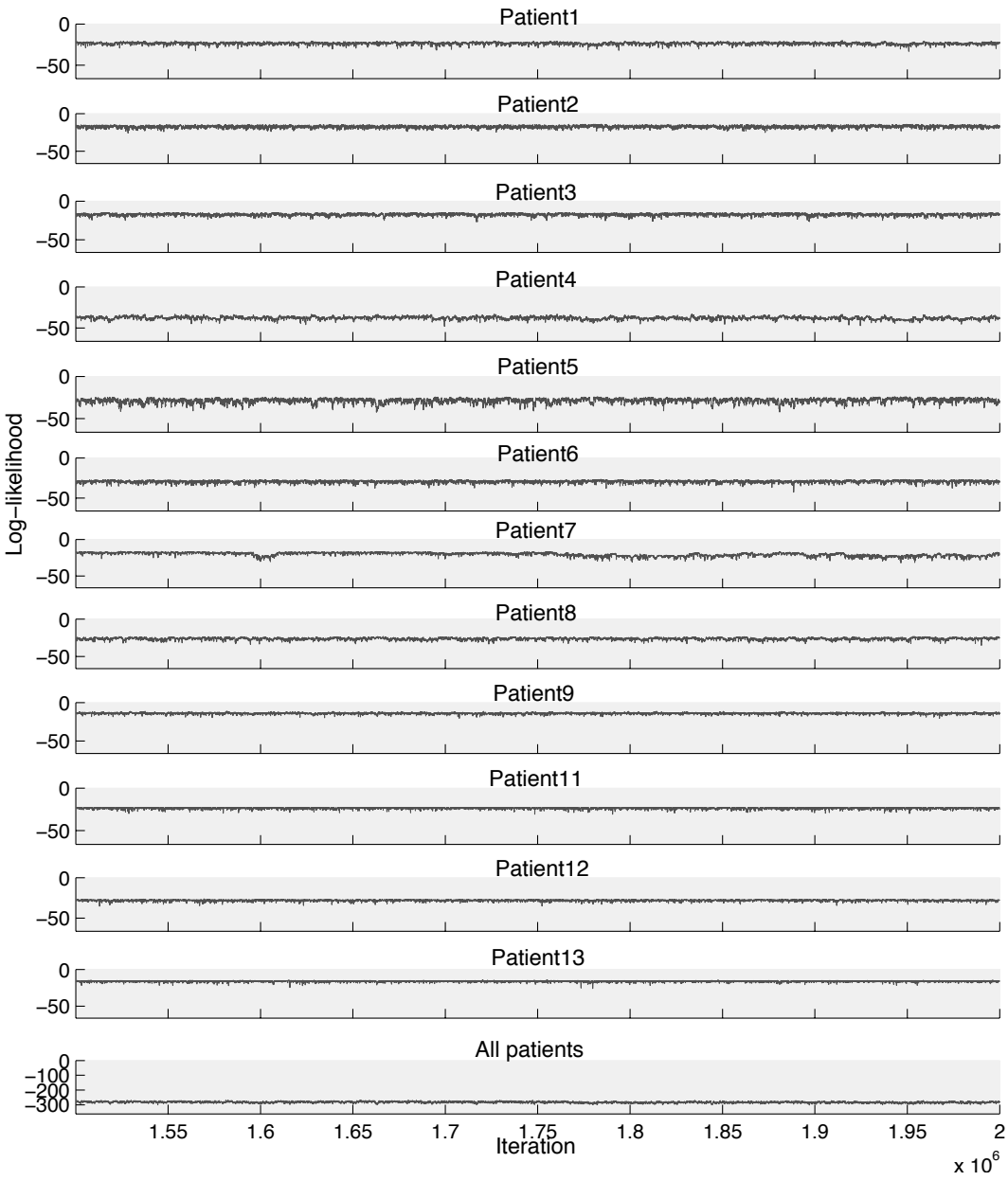

Figure 5.2: Log-likelihood of estimates using more frequent schedule. This figure presents the log-likelihood of the MCMC estimates for each virtual patient using the proposed schedule and all set of patients for the last 10^6 iterations of the algorithm. Notice that this correspond to a converged Markov chain

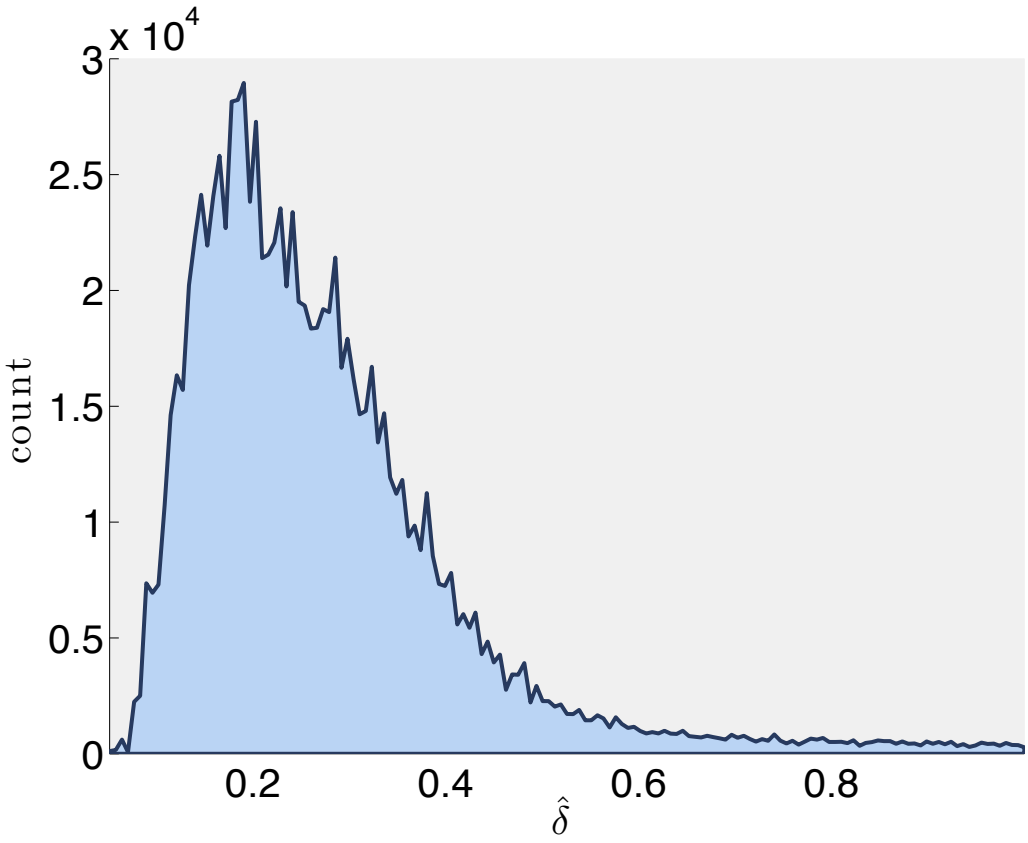

Figure 5.3: Posterior distributions of $\hat{\delta}$, Buzon schedule. Distribution of $\hat{\delta}$ obtained from the MCMC simulation using Buzon-based schedule virtual data from the multi-compartmental model. The distribution has a median of 0.25 days^{-1} and standard deviation of 0.49 days^{-1}.

a standard deviation of 0.24 days^{-1}. The significant difference between the uniform priors and the posterior distributions for $\hat{\delta}$ implies that the priors assumed were non-informative. Notice also the smaller bias and the smaller standard deviation of $\hat{\delta}$ using the more frequent schedule, implying that even this sample schedule still has a small size, a few more samples give a more exact and precise estimation.

Figure 5.5 and 5.6 present the posterior distributions of $\hat{\phi}$ for both schedules. The prior has a log-normal distribution with mean of 0.002, the same value used in

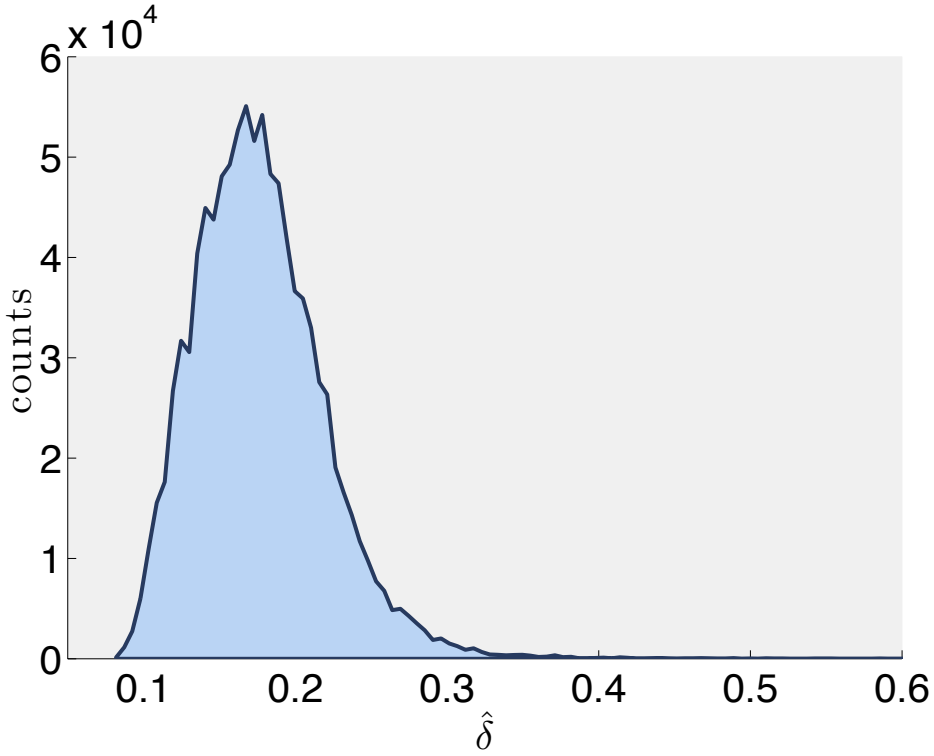

Figure 5.4: Posterior distributions of $\hat{\delta}$, More frequent schedule. Distribution of $\hat{\delta}$ obtained from the MCMC simulation using more frequent schedule virtual data from the multi-compartmental model. The distribution has a median of 0.17 days^{-1} and standard deviation of 0.24 days^{-1}.

simulations to create the virtual data. The posterior distributions of $\hat{\phi}$ are also approximately log-normal. The posterior distribution of $\hat{\phi}$ following the Buzon schedule has a median value of 0.0057 with a standard deviation of 0.35. Meanwhile, the posterior distribution of the more frequent schedule have a median value of 0.01 with a standard deviation of 0.3.

This analysis presents the bias estimation of 2-LTR in PBMC decay rate δ for two specific and realistic scenarios of limited 2-LTR data in PBMC after raltegravir intensification in patients under cART. These two scenarios were virtually created following for the first a sampling schedule as presented in Buzon et al. [11], and a second assuming a more frequent, but feasible and realistic scenario. The estimation

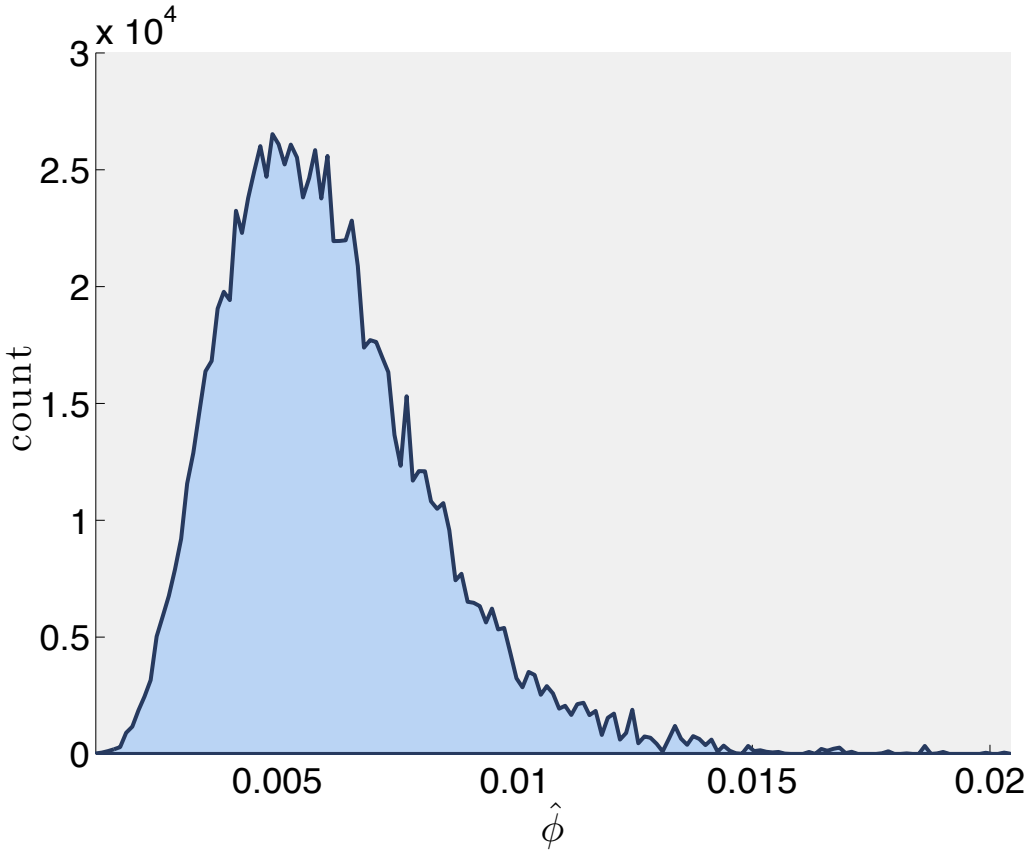

Figure 5.5: Posterior distributions of $\hat{\phi}$, Buzon schedule. Distribution of $\hat{\phi}$ obtained from the MCMC simulation using Buzon-based schedule virtual data from the multi-compartmental model. The distribution has a median of 0.0057 days^{-1} and standard deviation of 0.35 days^{-1}.

processes used follows the same procedure presented in [47] to estimate δ using real data. As we present here this specific procedure can incur a bias for parameters δ and ϕ due to neglecting explicit spatial dynamics in the single-compartment model used for fitting. However, this bias, can be decreased if more frequent sample schedule is used as proposed.

As we have presented in previous chapters, HIV ongoing replication in hyperplastic follicles with poor penetration of cART, is a possible scenario to produce 2-LTR circles patterns in PBMC after raltegravir intensification as in the studies in [11] and

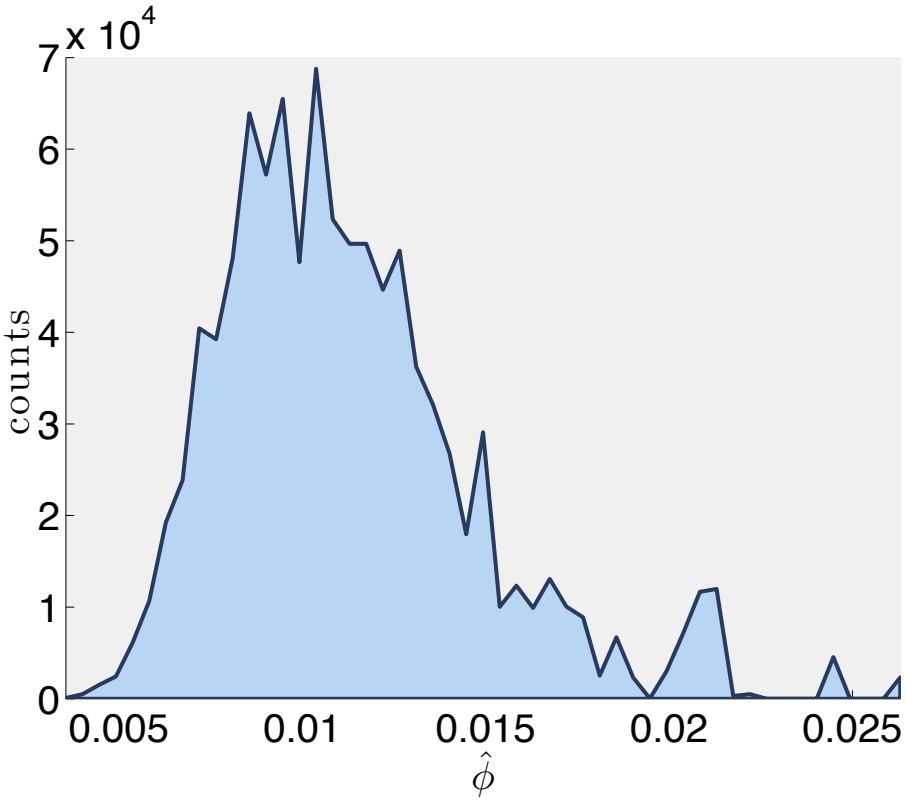

Figure 5.6: Posterior distributions of $\hat{\phi}$, more frequent schedule. Distribution of $\hat{\phi}$ obtained from the MCMC simulation using more frequent schedule virtual data from the multi-compartmental model. The distribution has a median of 0.01 days^{-1} and standard deviation of 0.3 days^{-1}.

[38]. Previously it was presented that in-vivo 2-LTR circles bearing cells half-life has been estimated between 8 and 25 days [82, 57]. In previous work we estimated the 2-LTR in PBMC decay rate to be around 0.47 days^{-1}. However, as we hypothesized, neglecting T-cells recirculation yield to underestimation of this value resulting in a bias up to 0.2 days^{-1}, but this bias can be decreased if more early data points are added. These results have important implications for designing future clinical trials and the estimation of parameters as the 2-LTR decay rate, to be used for possible measurements of cryptic viremia. The bias has to be considered in both the design of

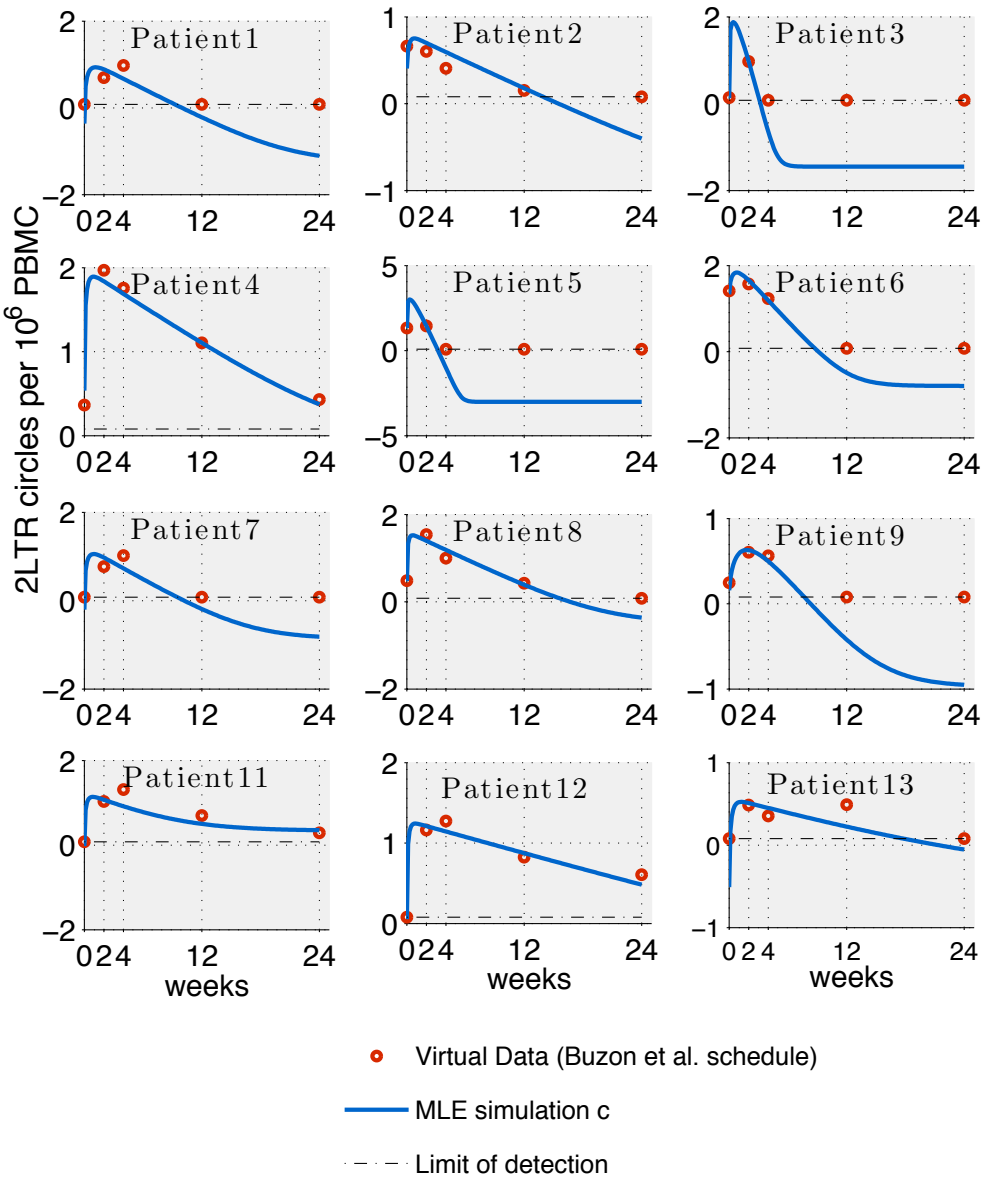

Figure 5.7: MLE fitting, Buzon-based schedule. This figure presents the maximum likelihood estimation of the Buzon-based schedule of virtual data for the 13 patients.

the sampling schedule and in estimating the parameters, since in this specific case, neglecting explicitly the physiological process in the single-compartment model produces error.

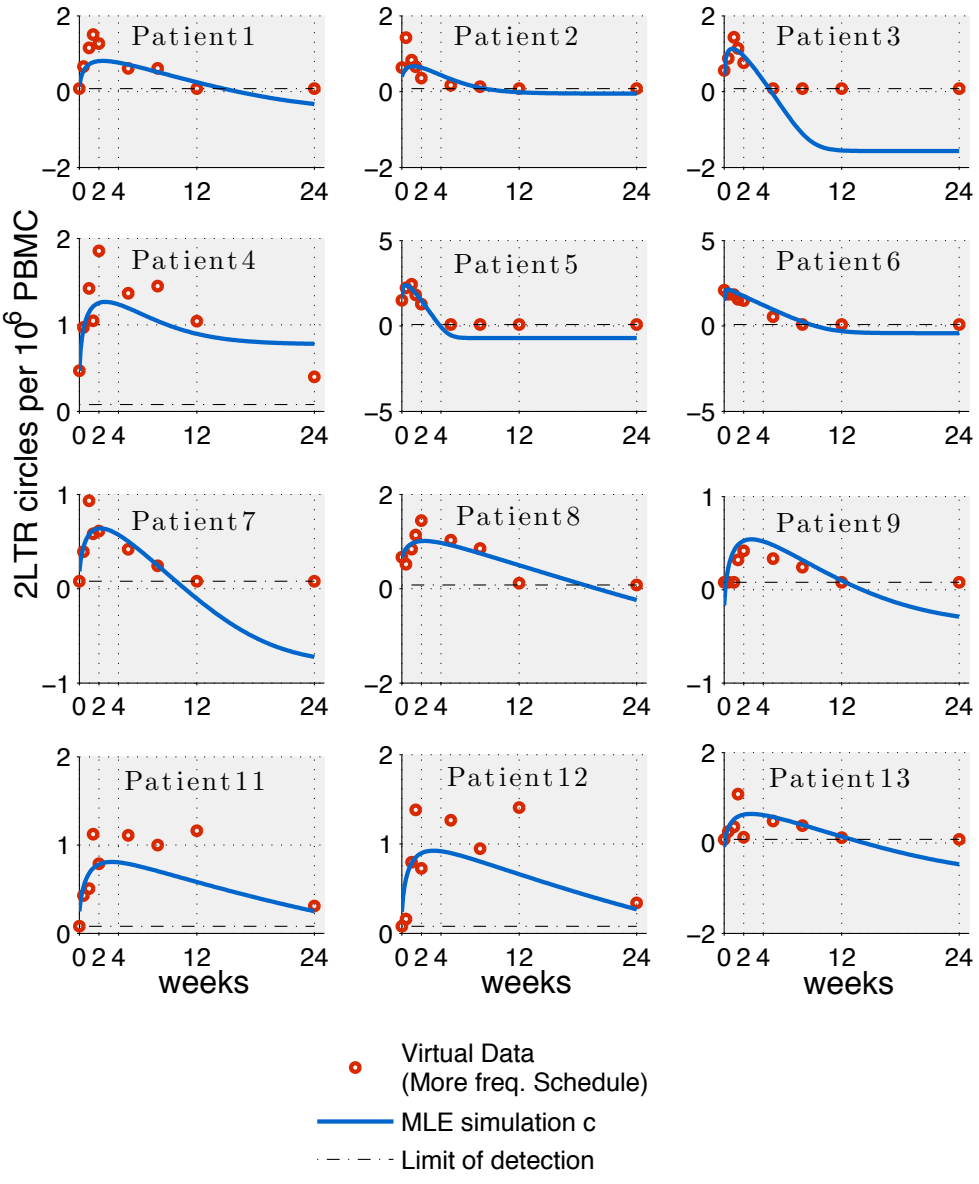

Figure 5.8: MLE fitting, more frequent schedule. This figure presents the maximum likelihood estimation of the more frequent schedule of virtual data for the 13 patients.

Chapter 6

CRYPTIC VIREMIA AND VIRAL BLIPS

6.1 Introduction

Intermittent episodes of transient viremia (viral blips) over the limit of detection occur in a significant set of HIV-patients under cART with suppressed plasma viral load (pVL) [23, 58].

The exact nature of blips is still controversial. Some literature describes occasional activation of long-lived cells or occasional activation of the immune system (due to vaccines or opportunistic infections) as possible causes [23, 24, 51, 42, 69, 70]. On the other side, studies present random fluctuations of pVL around mean HIV levels below limits of detection or errors and variability in assay (since percent error increases as viral levels decreases) [19, 58].

Generally, it is accepted that if the amplitude of the viral blip is greater than 200 $\frac{copies}{mL}$, it is associated with biological causes and virological rebound. Also if blips amplitudes are just over 50 $\frac{copies}{mL}$, but smaller than 200 $\frac{copies}{mL}$, random variations of viral load, with means very close, but below the limit of detection may be also the cause. In this case, the blip is not associated with virological failure [37, 15]. In most situations this phenomena is more related to viral persistence than assays errors [37].

Elimination of HIV-1 persistence is the current focus of research for viral eradication. Activation of long-lived cells, especially latent CD4+ T cells, is believed to be the principal cause of persistence. However, recent studies of 2-LTR formation after raltegravir (RAL) intensification and lower drug concentrations in lymphatic tissues present ongoing replication in anatomical reservoirs as a potential contributor. Previously, we have shown that 2-LTR formation in the blood after (RAL) intensification

can be produced due to replication in lymph nodes with suboptimal drug penetration. For low concentrations, there is a critical size before cryptic viremia exists inside the site. We, therefore, hypothesize that when the diameter of the lymph node follicle increase, there is a transition in the patient from viral replication suppression by cART to cryptic viremia. In this case, a viral blips occurs. We hypothesize also that this blip may not cross the limit of detection, and could possibly be the random variation about the mean, resulting in a blip over the limit of detection.

In this chapter we hypothesize that intermittent viremia episodes are due to changes in the diameter of lymph node follicles with poor penetration of drugs. We use a multi-compartmental model presented in previous chapters. We do a theoretical analysis of the model to find conditions that guarantee that the system does not result in cryptic viremia, and this then gives an initial state of the system. Next, we characterize the occurrence, duration, amplitude and final value of the viral blip as a function of the diameter of the lymph node follicles. We show that changes in the diameter affect mainly the connectivity between compartments resulting in transient episodes of viremia into the main compartment which is the blood.

6.2 Theoretical Conditions for Virus Suppression

To do the analysis we rewrite the model in (4.1) defining the vector $\mathbf{u}_i \in \mathbb{R}^3$ and the vector field $f(\mathbf{u}_i, \boldsymbol{\mu}_i)$ for $i = 1, ..., n$ as:

$$\mathbf{u}_i = \begin{bmatrix} \mathbf{x}_i \\ \mathbf{y}_i \\ \mathbf{v}_i \end{bmatrix},$$

$$f(\mathbf{u}_i, \boldsymbol{\mu}_i) = \begin{bmatrix} \lambda - d\mathbf{x}_i - \beta \mathbf{x}_i \mathbf{v}_i (1 - \eta_{RTI} \mathbf{u}_{RTI} \theta_i) \\ \beta \mathbf{x}_i \mathbf{v}_i (1 - \eta_{RTI} \mathbf{u}_{RTI} \theta_i) - a\mathbf{y}_i + y_e \\ \gamma (1 - \eta_{PI} \mathbf{u}_{PI} \varphi_i) \mathbf{y}_i - \omega \mathbf{v}_i \end{bmatrix},$$

with $\boldsymbol{\mu}_i = [\theta_i, \phi_i]$ representing the drug penetration. We define also the adjacency matrices $\mathbf{D}_1$, $\mathbf{D}_2$ and $\mathbf{D}_3 \in \mathbb{R}^{n \times n}$ with elements $[\mathbf{D}_1]_{i,j} = D^{(x)}_{i,j}$, $[\mathbf{D}_2]_{i,j} = D^{(y)}_{i,j}$

and $[\mathbf{D}_3]_{i,j} = D^{(v)}_{i,j}$ respectively, defining how the compartments are connected for each state. For each $\mathbf{D}_k$, by definition, the corresponding Laplacian matrix $\mathbf{L}_k$ is given by,

$$[\mathbf{L}_k]_{i,j} = \begin{cases} \sum_j [\mathbf{D}_k]_{i,j} & i = j \\ -[\mathbf{D}_k]_{i,j} & i \neq j \end{cases}.$$

Thus, define the concatenated vector

$$\mathbf{u} = \begin{bmatrix} \mathbf{u}_1 \\ \mathbf{u}_2 \\ \vdots \\ \mathbf{u}_n \end{bmatrix},$$

and the vector field

$$f(\mathbf{u}) = \begin{bmatrix} f(\mathbf{u}_1, \boldsymbol{\mu}_1) \\ f(\mathbf{u}_2, \boldsymbol{\mu}_2) \\ \vdots \\ f(\mathbf{u}_n, \boldsymbol{\mu}_n) \end{bmatrix},$$

we can rewrite the system in equation (4.1) as

$$\dot{\mathbf{u}} = f(\mathbf{u}) - \mathcal{L}\mathbf{u}, \tag{6.1}$$

where $\mathcal{L}$ is defined as,

$$\mathcal{L} = \sum_{k=1}^{3} \mathbf{C}\mathbf{L}_k \otimes \mathbf{E}_k. \tag{6.2}$$

Here, $\mathbf{C} = diag\,(\rho)$, the Kronecker product operator $\otimes$, and $\mathbf{E}_k = e_k e_k^{\mathbf{T}} \in \mathbb{R}^{3\times 3}$ with e_k being the k^{th} canonical basis vector. When y_e is significantly small, a quasi stationary point of $\mathbf{u}$, when there is no infection, is $\bar{\mathbf{u}}_0 = \mathbf{1}_n \otimes \mathbf{w}_0$, with $\mathbf{w_0} = \begin{bmatrix} \frac{\lambda}{d} \\ 0 \\ 0 \end{bmatrix}$ and $\mathbf{1}_n$ the $n \times 1$ vector of ones.

To understand the conditions for which the virus is suppressed in all compartments, we need to understand when each compartment $\mathbf{u}_i$ goes to $\mathbf{w}_0$ as time goes to infinity. We use the following definitions and procedure as presented in [4, 2]. Defining $\mathbf{w} = \frac{1}{n}\sum_{i=1}^{n} \mathbf{u_i}$, let

$$\begin{aligned} \bar{\mathbf{u}} &= \mathbf{1}_n \otimes \mathbf{w}, \\ \tilde{\mathbf{u}} &= \mathbf{u} - \bar{\mathbf{u}}, \\ \tilde{\mathbf{u}}_i &= \mathbf{u}_i - \mathbf{w}. \end{aligned}$$

Notice that for any matrix $\mathbf{T}$ of 3 rows, $\tilde{\mathbf{u}}^{\mathbf{T}}(\mathbf{1}_n \otimes \mathbf{T}) = 0$. Then, we have that

$$\begin{aligned} \dot{\tilde{\mathbf{u}}} &= f(\mathbf{u}) - \mathcal{L}\mathbf{u} - \dot{\bar{\mathbf{u}}} \\ &= f(\mathbf{u}) - \mathcal{L}\tilde{\mathbf{u}} - \mathcal{L}\bar{\mathbf{u}} - \dot{\bar{\mathbf{u}}} \\ &= f(\mathbf{u}) - \mathcal{L}\tilde{\mathbf{u}} - \textstyle\sum_{\mathbf{k=1}}^{\mathbf{3}} (\mathbf{CL_k} \otimes \mathbf{E_k})(\mathbf{1_n} \otimes \mathbf{w}) - \dot{\bar{\mathbf{u}}} \\ &= f(\mathbf{u}) - \mathcal{L}\tilde{\mathbf{u}} - \textstyle\sum_{\mathbf{k=1}}^{\mathbf{3}} (\mathbf{CL_k 1_n} \otimes \mathbf{E_k w}) - \dot{\bar{\mathbf{u}}} \\ &= f(\mathbf{u}) - \mathcal{L}\tilde{\mathbf{u}} - \dot{\bar{\mathbf{u}}} \end{aligned}$$

The last line of above is true because the vector $\mathbf{1}_n$ is an eigenvector of the matrix $\mathbf{L}_k$ associated with the eigenvalue zero. Notice also that if

$$f(\bar{\mathbf{u}}) = \begin{bmatrix} f(\mathbf{w}, \boldsymbol{\mu}_1)^{\mathbf{T}} \\ f(\mathbf{w}, \boldsymbol{\mu}_2)^{\mathbf{T}} \\ \vdots \\ f(\mathbf{w}, \boldsymbol{\mu}_n)^{\mathbf{T}} \end{bmatrix},$$

then, we have the system in the form,

$$\dot{\tilde{\mathbf{u}}} = f(\mathbf{u}) - \mathcal{L}\tilde{\mathbf{u}} - f(\bar{\mathbf{u}}). \tag{6.3}$$

From here, we based the derivation of viral suppression conditions as an specific case of the recent works done in [4, 2], but, with two main differences: first, the Laplacian

operator $\mathcal{L}$ in equation (6.2) for our problem is not symmetric because it includes the diagonal matrix $\mathbf{C}$; and second, the vector field $f(\mathbf{u})$ include parameters (μ_i) that could have different values for each compartment. However, the derivation is for the particular case when all the states in every compartment "synchronize" to the stationary point $\bar{\mathbf{u}}$.

We use the Lyapunov function $\mathbf{V} = \frac{1}{2}\tilde{\mathbf{u}}^{\mathbf{T}} (\mathbf{I}_n \otimes \mathbf{P}) \tilde{\mathbf{u}}$, where $\mathbf{P}$ is a positive real symmetric matrix in $\mathbb{R}^{3\times 3}$. This leads to

$$\dot{\mathbf{V}} = \tilde{\mathbf{u}}^{\mathbf{T}} (\mathbf{I}_n \otimes \mathbf{P}) (f(\mathbf{u}) - f(\bar{\mathbf{u}})) - \tilde{\mathbf{u}}^{\mathbf{T}} \mathcal{L} (\mathbf{I}_n \otimes \mathbf{P}) \tilde{\mathbf{u}}. \tag{6.4}$$

Taking the second term of the right in (6.4), expanding $\mathcal{L}$ and using the Kronecker product property $(\mathbf{A} \otimes \mathbf{B})(\mathbf{C} \otimes \mathbf{D}) = (\mathbf{AC} \otimes \mathbf{BD})$ yields,

$$\tilde{\mathbf{u}}^{\mathbf{T}} \mathcal{L} (\mathbf{I}_n \otimes \mathbf{P}) \tilde{\mathbf{u}} = \sum_{k=1}^{3} \tilde{\mathbf{u}}^{\mathbf{T}} (\mathbf{C} \otimes \mathbf{I}_3) (\mathbf{L}_k \otimes \mathbf{E_k P}) \tilde{\mathbf{u}}. \tag{6.5}$$

Given that $\mathbf{L}_k$ is symmetric, it follows that $(\mathbf{L}_k \otimes \mathbf{E_k P}) + (\mathbf{L}_k \otimes \mathbf{E_k P})^{\mathbf{T}} = \mathbf{L}_k \otimes (\mathbf{PE}_k + \mathbf{E_k P})$, and for a positive real symmetric matrix $\mathbf{P}$, there exist a positive definite matrix $\mathbf{Q}_k \in \mathbb{R}^{3\times 3}$ such that $\frac{1}{2}(\mathbf{PE}_k + \mathbf{E_k P}) = \mathbf{Q}_k^{\mathbf{T}} \mathbf{Q}_k$. Hence, equation (6.5) becomes

$$\begin{aligned} \tilde{\mathbf{u}}^{\mathbf{T}} \mathcal{L} (\mathbf{I}_n \otimes \mathbf{P}) \tilde{\mathbf{u}} &= \textstyle\sum_{k=1}^{3} \tilde{\mathbf{u}}^{\mathbf{T}} (\mathbf{C} \otimes \mathbf{I}_3) \left(\mathbf{I}_n \otimes \mathbf{Q}_k^{\mathbf{T}}\right) (\mathbf{L}_k \otimes \mathbf{I}_3) (\mathbf{I}_n \otimes \mathbf{Q}_k) \tilde{\mathbf{u}} \\ &= \textstyle\sum_{k=1}^{3} \tilde{\mathbf{u}}^{\mathbf{T}} \left(\mathbf{I}_n \otimes \mathbf{Q}_k^{\mathbf{T}}\right) (\mathbf{CL}_k \otimes \mathbf{I}_3) (\mathbf{I}_n \otimes \mathbf{Q}_k) \tilde{\mathbf{u}} \end{aligned} \tag{6.6}$$

Moreover, given that:

1. All eigenvalues of $\mathbf{CL}_k$ are greater or equal to zero because the matrix $\mathbf{L}_k$ is positive-semidefinite and $\mathbf{C}$ is diagonal.
2. The matrix $\mathbf{CL}_k$ has a eigenvector $\mathbf{v} = \mathbf{1}_n$ associatted with the eigenvalue $\lambda_1^{(k)} = 0$. Thus the eigenvalues of $\mathbf{CL}_k$ can be arranged in ascending order

$$0 = \lambda_1^{(k)} \leq \lambda_2^{(k)} \leq ... \leq \lambda_n^{(k)}$$

3. By the Couran-Fisher minimax theorem [41], for any $\mathbf{z} \perp \mathbf{v}$ we have that $\mathbf{z^T C L}_k \mathbf{z} \geq \lambda_2^{(k)} \mathbf{z^T z}$. In the same way for any $\mathbf{z} \perp (\mathbf{v} \otimes \mathbf{I}_3)$ we have that $\mathbf{z}^{\mathbf{T}} (\mathbf{CL}_k \otimes \mathbf{I}_3) \mathbf{z} \geq \lambda_2^{(k)} \mathbf{z^T z}$.

4. It follows that for $\mathbf{z} = (\mathbf{I}_n \otimes \mathbf{Q}_k) \tilde{\mathbf{u}}$ we have that

$$\begin{aligned} \mathbf{z}^{\mathbf{T}} (\mathbf{v} \otimes \mathbf{I}_3) &= \tilde{\mathbf{u}}^{\mathbf{T}} \left(\mathbf{I}_n \otimes \mathbf{Q}_k^{\mathbf{T}}\right) (\mathbf{1}_n \otimes \mathbf{I}_3) \\ &= \tilde{\mathbf{u}}^{\mathbf{T}} \left(\mathbf{1}_n \otimes \mathbf{Q}_k^{\mathbf{T}}\right) \\ &= 0. \end{aligned}$$

   Therefore, $(\mathbf{I}_n \otimes \mathbf{Q}_k) \tilde{\mathbf{u}} \perp (\mathbf{v} \otimes \mathbf{I}_3)$.

From (6.6),

$$\begin{aligned} \tilde{\mathbf{u}}^{\mathbf{T}} \left(\mathbf{I}_n \otimes \mathbf{Q}_k^{\mathbf{T}}\right) (\mathbf{CL}_k \otimes \mathbf{I}_3) (\mathbf{I}_n \otimes \mathbf{Q}_k) \tilde{\mathbf{u}} &\geq \lambda_2^{(k)} \tilde{\mathbf{u}}^{\mathbf{T}} \left(\mathbf{I}_n \otimes \mathbf{Q}_k^{\mathbf{T}}\right) (\mathbf{I}_n \otimes \mathbf{Q}_k) \tilde{\mathbf{u}} \\ &= \lambda_2^{(k)} \tilde{\mathbf{u}}^{\mathbf{T}} \left(\mathbf{I}_n \otimes \mathbf{Q}_k^{\mathbf{T}} \mathbf{Q}_k\right) \tilde{\mathbf{u}} \\ &= \lambda_2^{(k)} \tilde{\mathbf{u}}^{\mathbf{T}} (\mathbf{I}_n \otimes \mathbf{PE}_k) \tilde{\mathbf{u}} \end{aligned}$$

Therefore, the equation (6.4) takes the form

$$\begin{aligned} \dot{\mathbf{V}} &\leq \tilde{\mathbf{u}}^{\mathbf{T}} (\mathbf{I}_n \otimes \mathbf{P}) (f(\mathbf{u}) - f(\bar{\mathbf{u}})) - \textstyle\sum_{k=1}^{3} \lambda_2^{(k)} \tilde{\mathbf{u}}^{\mathbf{T}} (\mathbf{I}_n \otimes \mathbf{PE}_k) \tilde{\mathbf{u}} \\ &= \textstyle\sum_{i=1}^{n} \left\{ \tilde{\mathbf{u}}_i^{\mathbf{T}} \mathbf{P} (f(\mathbf{u}_i, \boldsymbol{\mu}_i) - f(\mathbf{w}, \boldsymbol{\mu}_i)) - \tilde{\mathbf{u}}_i^{\mathbf{T}} \mathbf{P} \left(\textstyle\sum_{k=1}^{3} \lambda_2^{(k)} \mathbf{E}_k \right) \tilde{\mathbf{u}}_i \right\} . \end{aligned}$$

By the mean value theorem, and assuming that $\mathbf{w} \to \mathbf{w}_0$ as $t \to \infty$,

$$f(\mathbf{u}_i, \boldsymbol{\mu}_i) - f(\mathbf{w}_0, \boldsymbol{\mu}_i) = \mathbf{J}(\mathbf{w}_0, \boldsymbol{\mu}_i) \tilde{\mathbf{u}}_i + g(\tilde{\mathbf{u}}_i, \boldsymbol{\mu}_i),$$

where $\mathbf{J}(\mathbf{w}_0, \boldsymbol{\mu}_i) = \begin{bmatrix} -d & 0 & -\frac{\beta\lambda(1-\eta_{RTI}\theta)}{d} \\ 0 & -a & \frac{\beta\lambda(1-\eta_{RTI}\theta_i)}{d} \\ 0 & \gamma(1-\eta_{PI}\varphi_i) & -\omega \end{bmatrix}$, and where $g(\tilde{\mathbf{u}}_i, \boldsymbol{\mu}_i)$ satisfies $\frac{\|g(\tilde{\mathbf{u}}_i, \boldsymbol{\mu}_i)\|_2}{\|\tilde{\mathbf{u}}_i\|_2} \to 0$ as $\|\tilde{\mathbf{u}}_i\|_2 \to 0$. Hence, rearranging terms, for t large,

$$\dot{\mathbf{V}} \leq \sum_{i=1}^{n} \left\{ \tilde{\mathbf{u}}_i^{\mathbf{T}} \left[\mathbf{P} \left(\mathbf{J}(\mathbf{w}_0, \boldsymbol{\mu}_i) - \sum_{k=1}^{3} \lambda_2^{(k)} \mathbf{E}_k \right) \right] \tilde{\mathbf{u}}_i + \tilde{\mathbf{u}}_i^{\mathbf{T}} \mathbf{P} g(\tilde{\mathbf{u}}_i, \boldsymbol{\mu}_i) \right\} \tag{6.7}$$

Let define $g(\tilde{\mathbf{u}}) = \left[g(\tilde{\mathbf{u}}_1, \boldsymbol{\mu}_1)^{\mathbf{T}}, g(\tilde{\mathbf{u}}_2, \boldsymbol{\mu}_2)^{\mathbf{T}}, ..., g(\tilde{\mathbf{u}}_n, \boldsymbol{\mu}_n)^{\mathbf{T}}\right]^{\mathbf{T}}$. Define the matrix $\mathbf{A}$ as the direct sum of the matrices $\mathbf{A}_i = \mathbf{J}(\mathbf{w}_0, \boldsymbol{\mu}_i) - \sum_{k=1}^{3} \lambda_2^{(k)} \mathbf{E}_k$ for each $f(\mathbf{u}_i, \boldsymbol{\mu}_i)$,

$$\mathbf{A} = \bigoplus_{i=1}^{n} \{\mathbf{A}_i\} = \begin{bmatrix} \mathbf{A}_1 & 0 & \cdots & 0 \\ 0 & \mathbf{A}_2 & \ddots & \vdots \\ \vdots & \ddots & \ddots & 0 \\ 0 & \cdots & 0 & \mathbf{A}_n \end{bmatrix},$$

Therefore, the inequality in (6.7) can be compacted in the form,

$$\dot{\mathbf{V}} \leq \tilde{\mathbf{u}}^{\mathbf{T}} (\mathbf{I}_n \otimes \mathbf{P}) \mathbf{A} \tilde{\mathbf{u}} + \tilde{\mathbf{u}}^{\mathbf{T}} (\mathbf{I}_n \otimes \mathbf{P}) g(\tilde{\mathbf{u}}).$$

Furthermore, if the matrix $\mathbf{A}$ is Hurwitz,

$$(\mathbf{I}_n \otimes \mathbf{P})\mathbf{A} + \mathbf{A}^{\mathbf{T}} (\mathbf{I}_n \otimes \mathbf{P}) = -\mathbf{B},$$

for symmetric positive definite matrix $\mathbf{B}$. Further, for any $\gamma > 0$ there exist $r > 0$ such that $\|g(\tilde{\mathbf{u}})\|_2 < \gamma \|\tilde{\mathbf{u}}\|_2$ for all $\|\tilde{\mathbf{u}}\|_2 < r$. Therefore,

$$\dot{\mathbf{V}} \leq -\left[\lambda_{min}\{\mathbf{B}\} - 2\gamma \|\mathbf{I}_n \otimes \mathbf{P}\|_2\right] \|\tilde{\mathbf{u}}\|_2^2, \ \forall \|\tilde{\mathbf{u}}\|_2 < r.$$

Thus, for a value $\gamma < \frac{\lambda_{min}\{\mathbf{B}\}}{2\|\mathbf{I}_n \otimes \mathbf{P}\|_2}$, then $\dot{\mathbf{V}} < 0$. So, the principal condition of stability for $\bar{\mathbf{u}}$ is the spectrum of the matrix $\mathbf{A}$. Given that $\mathbf{A}$ is a block diagonal matrix, in order for it to be Hurwitz, the real part of the maximum eigenvalue of each block $\mathbf{A}_i$ has to be smaller than zero.

The characteristic polynomial for the matrix $\mathbf{A}_i$ has the form

$$\pi(\sigma) = \left(-a - \lambda_2^{(2)} - \sigma\right)\left(-\omega - \lambda_2^{(3)} - \sigma\right) - \left(\frac{\beta\lambda\gamma}{d}\right) f_i = 0,$$

with $f_i = (1 - \eta_{RTI}\mathbf{u}_{RTI}\theta_i)(1 - \eta_{PI}\mathbf{u}_{PI}\varphi_i)$. It is not difficult to show that to have $\sigma < 0$ the following relation has to be fulfilled,

$$f_i \frac{\frac{\beta\lambda\gamma}{da\omega}}{\left(1+\frac{\lambda_2^{(2)}}{a}\right)\left(1+\frac{\lambda_2^{(3)}}{\omega}\right)} < 1.$$

Notice that the condition for block matrices in $\mathbf{A}$ differs only by the factor f_i. Thus, this condition only depends on the block matrix $\mathbf{A}_i$ with the maximum value of f_{max}, which is equivalent to the compartment i with the minimum drug penetration (θ_i, φ_i). Notice also that when the virus is not directly diffused from the main compartment to the others $\lambda_2^{(3)} \approx 0$. Therefore we define a condition of viral suppression in every compartment with the form,

$$R = f_{max} \frac{R_0}{\left(1+\frac{\lambda_2^{(2)}}{a}\right)}, \tag{6.8}$$

with $R_0 = \frac{\beta\lambda\gamma}{da\omega}$. Thus, R has to be smaller than 1 to guarantee that all compartments synchronize to the quasi stationary state $\mathbf{w}_0$.

We use the resulting data from the Monte-Carlo simulation in chapter 4 for the patients with low values of latently infected reactivation rate. From these individuals, we compute R from equation (6.8) and use the viral load steady state in the most remote and measurable compartment. Figure 6.1 shows this relation. As is depicted, when R is smaller than 1, the compartments synchronize to 10^{-5} $\frac{virions}{mL}$. As R increases over 1, the most remote compartment begin to sustain viral replication. Since R depends on $\lambda_2^{(2)}$, this instability depends on the diameter of the site. Based on this, we hypothesize that a viral blip is the consequence of crossing this threshold because of an increase of the diameter size. For all the simulations in the following sections, the system is parameterized with an initial diameter size so that R is smaller than 1 initially.

6.3 Model of Diameter Increase

A relevant parameter for the behavior of the system is the size of the anatomical reservoir. Mathematically this size affects the rate at which T-cells and virions move

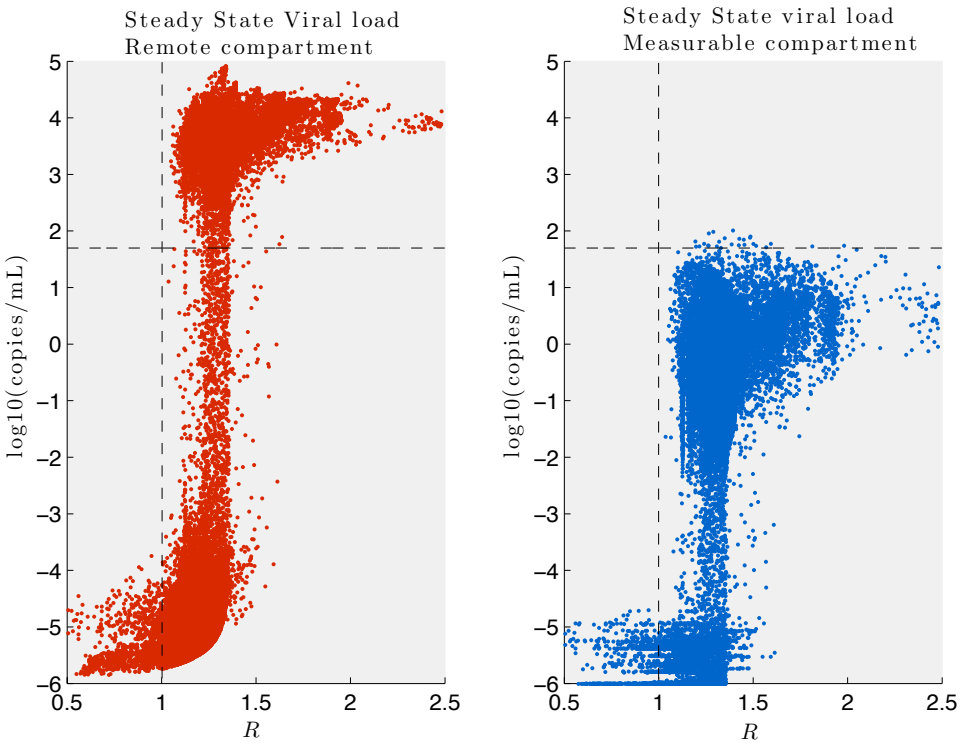

Figure 6.1: Steady state viral load in measurable compartment and remote compartment versus R. Notice for both figures the steady state synchronizes at 10^{-5} virions/mL for $R < 1$. However when $R > 1$, the two figures present the scenario where cryptic viremia is present.

among compartments. In our model $D_{i,j}^{(\cdot)} = \hat{D}_{i,j}^{(\cdot)} \frac{A_{i,j}}{V_i}$ where $A_{i,j}$ represents the surface area between layers i and j inside the lymph node, V_i the volume of layer i and $\hat{D}_{i,j}^{(\cdot)}$ the permeability of T-cells and virus movement between compartment i and j. Hence, the critical parameter for reservoir size is the diameter δ of the lymph node follicle. This diameter affects the value of the connectivity coefficient $\lambda_2^{(2)}$ leading to different values of R. Therefore, we are interested in how this diameter might change. A sigmoid model is used to describe the behavior of the diameter with time. The model of diameter rise has the form,

$$\delta(t) = \frac{\delta_{max} - \delta_{min}}{1 + e^{-\xi(t-t_{0.5})}} + \delta_{min}, \tag{6.9}$$

with minimum and maximum diameter δ_{min} and δ_{max} respectively. The rate of diameter rise ξ and the time at which the diameter reach the midpoint is $t_{0.5}$. Notice that, as $\delta(t)$ changes, we will have different values for R. These changes will lead to different viral load behaviors in the main compartment. Thus, depending on δ_{min}, δ_{max}, and ξ we can obtain different behaviors of the viral load and then characterize the viral blip, always maintaining $R < 1$ for $\delta(0)$.

6.4 Characterization of Viral Blips

We start the characterization of the viral blip for fixed values of R_0, a and f_{max}, and analyzing how the sanctuary site diameter influences the formation of viral blips. To understand how the increasing of the diameter could set the characteristics of a viral blip, we first establish a value for $t_{0.5}$ at which the system has reached steady state. In this case we set $t_{0.5} = 400\ days$. Then, we tune the parameter between ξ in a reasonable range. We hypothesize that, during a relative fast diameter increase, a transient blip occurs, and cryptic viremia is established. We, therefore, use values of ξ from 0.03 to 0.05 days^{-1} to give an enough time for viral blips to increase and last for a reasonable duration.

Figure 6.2 presents the results for the viral load in compartment one, the most remote compartment and R as the the diameter increase for the different rates, assuming $t_{0.5} = 400$ days, and δ_{min} and δ_{max} equal to 0.04 and 1.5 mm respectively. Notice that the value of δ_{min}, according to the previous section, guarantees the absence of cryptic viremia with $R < 1$. We also assume for that the compartmental system has the fixed parameters shown in table 6.1 (see chapter 4 for more details). Notice that the low values of drug distribution ratios r_1 and r_2, implying very low drug penetrations in the sites, and are in agreement with the range to have cryptic viremia described in previous chapters. However, because the small initial diameter, cryptic viremia does not emerge. As expected, for smaller rates of the diameter changes, we have transient episodes of viremia in compartment one with higher and longer amplitude and duration (in red in figure 6.2). We can get viral blips from 55 $\frac{virions}{mL}$ (in blue in the figure) to

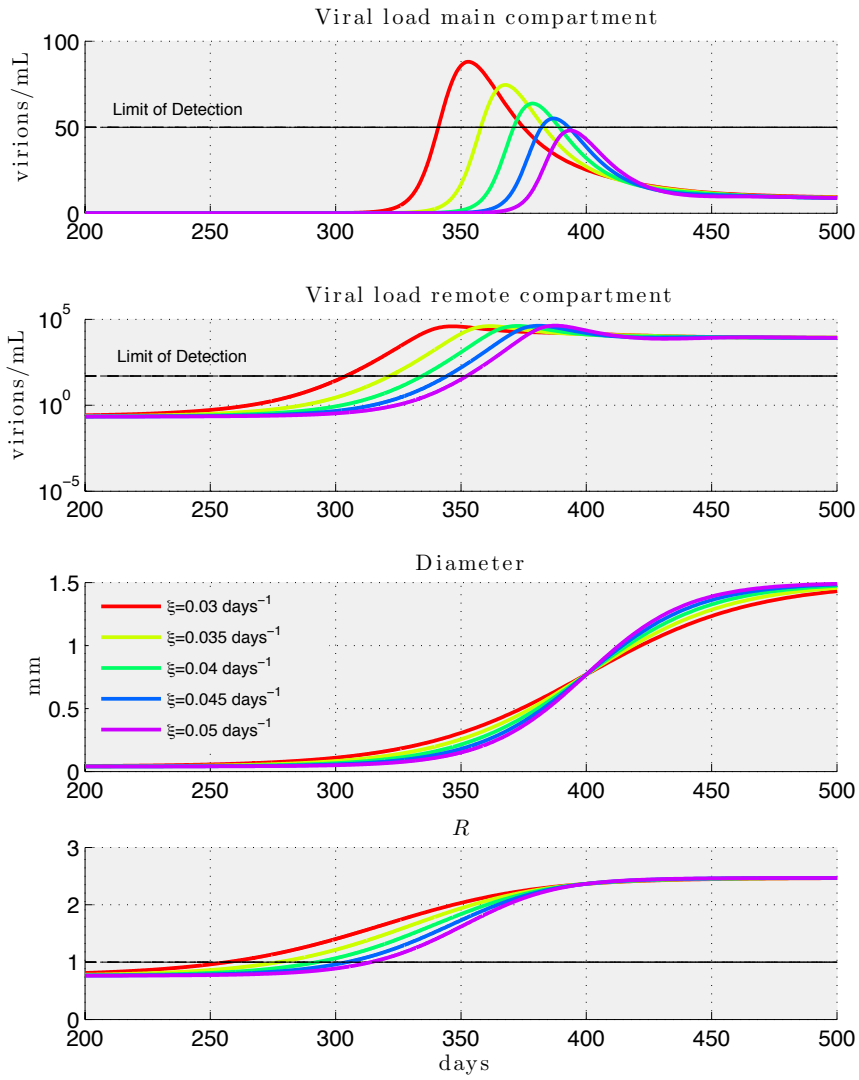

Figure 6.2: Viral blip behavior changing ξ. The figure presents how the behavior of the virus in compartment 1 and 10, together with the behavior of R changes as the diameter changes for different values of ξ. Notice that for a minimum ξ the amplitude of the viral blip in compartment one is higher. Notice also that for all values of ξ, the change of the diameter leads the system from a suppressed state to a cryptic virema state.

90 $\frac{virions}{mL}$ (in red in the figure) with duration over the limit of detection between 10 to 30 days, in agreement with the data found in the literature [23].

Figure 6.3 shows that by changing only ξ we can generate viral blips with

Table 6.1: Model Parameters. Parameters for HIV an T cells rates, drug penetration and diffusivity (See chapter 4 for a detailed description).

Parameters	Value	Units
λ	598.57	$\frac{cells}{\mu L \times day}$
d	0.21	$\frac{1}{day}$
β	6.8×10^{-6}	$\frac{mL}{copies \times day}$
a	1.5	$\frac{1}{day}$
γ	2.1×10^{3}	$\frac{copies \times \mu L}{cells \times mL \times day}$
ω	18.8	$\frac{1}{day}$
η	0.61	–
V_1	30	mL
$\hat{D}_{1,2}^{(x,y,c)}$	$\frac{1}{300}$	$\frac{mm^2}{day}$
$\hat{D}_{1,2}^{(v)}$	0	$\frac{mm^2}{day}$
$\hat{D}_{i,j}^{(x,y,c)}$ $i,j > 1$	0.1	$\frac{mm^2}{day}$
$\hat{D}_{i,j}^{(v)}$ $i,j > 1$	0.43	$\frac{mm^2}{day}$
$r_1 = r_2$	0.01	–

duration between 20 and 30 days of duration for rates of ξ between approximately 0.031 to 0.039 days^{-1}. The behavior of the amplitude and the duration of the blip clearly decrease as ξ increases. For a fixed R_0 and f_{max} the faster the diameter increases, the lower the amplitude of the viral blip and shorter its duration over the limit of detection. Depending on R_0, the ranges for amplitude and duration may vary.

Using $\xi = 0.031 \text{days}^{-1}$, assuring that we have a viral blip with amplitude of approximately 85 $\frac{copies}{mL}$ and duration of 30 days, we use the same values for the other parameters as in table 6.1 to see the variability of the blip as the final diameter changes. Thus, we disrupt the diameter rise when $\delta(t)$ reaches different values and sustain that diameter value over the range of the simulation in order to understand how the maximum diameter affects the behavior of the viral blip. Specifically we stop increasing the diameter at values 0.05, 0.2, 0.4, 0.8 and 1.2mm. As shown in figure 6.4, for small maximum diameters, if that do no result in $R > 1$, the virus remains suppressed in all compartments (red line). As the diameter gets larger, the viral load increases in a

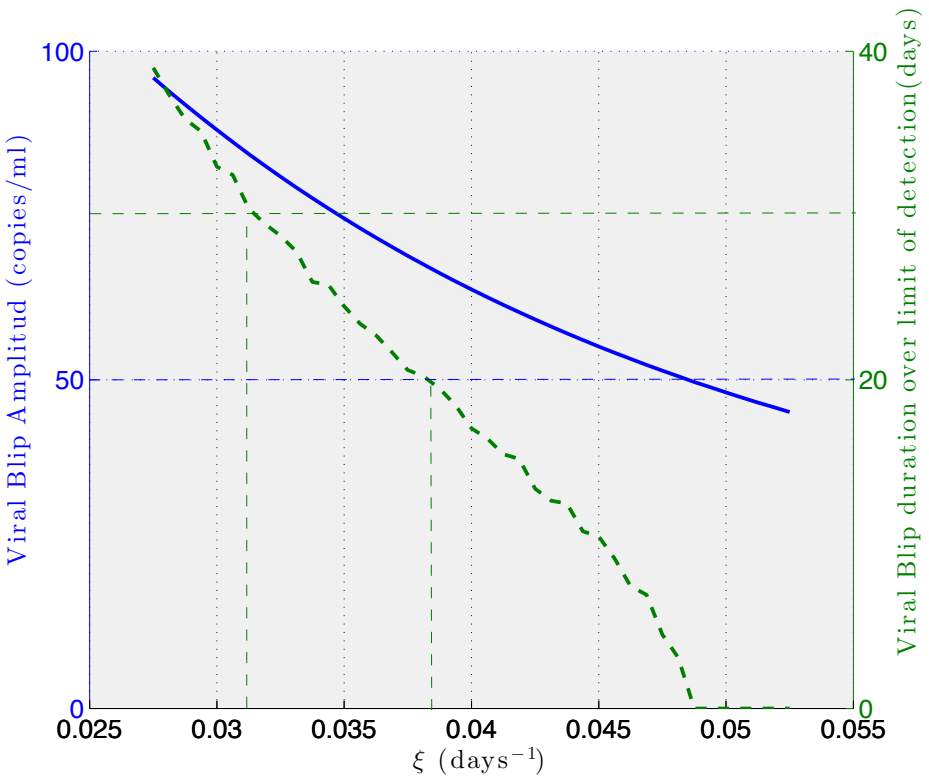

Figure 6.3: Viral blip amplitude and duration vs. ξ. In blue, the amplitude of the viral blip decreases as ξ increases, with a maximum value of 90 virions/mL. In green, a similiar behavior for the viral blip duration in ranges with similar conditions to previous studies.

monotonic way with higher peaks (yellow line). After a certain point, the maximum diameters no longer change the viral blip amplitude, and the viral load steady-state value in the blood decreases as the maximum diameter increases (green, blue and magenta lines).

To understand why there are different steady state levels of the viral load in compartment one (from here, referred to as $\bar{\mathbf{v}}_1$), we analyze the behavior of the target cells in compartment 1, 2 and 10 for the different values of the maximum diameter. As figure 6.5 shows, in compartment 1, for the smaller diameter corresponding to a initial $R < 1$ (this is for $\delta_{max} = 0.1$ and yellow line in the figure) a significant number of cells

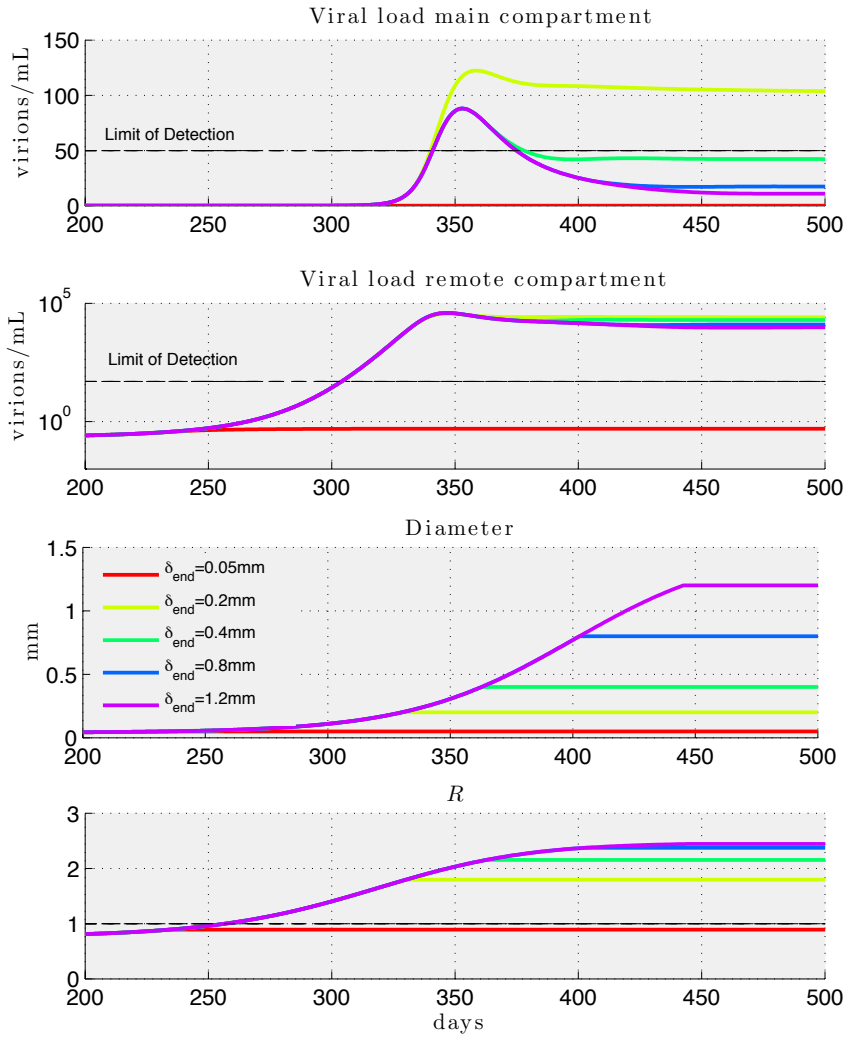

Figure 6.4: Viral blip behavior for different final diameters. For a fixed R_0 value, viral load in compartment 1 and 10, diameter and R in time behaviors for different final values of the diameter. Notice that the final diameter leads to different steady states of viral load in compartment 1.

are infected. This number of infected cells is comparable to the cell count for larger maximum diameters, where a smaller quantity of cells is infected. In contrast, the opposite happens in the most external and most interior compartment (compartments 2 and 10 respectively): Inside the sphere the target cells are infected more for larger maximum diameters.

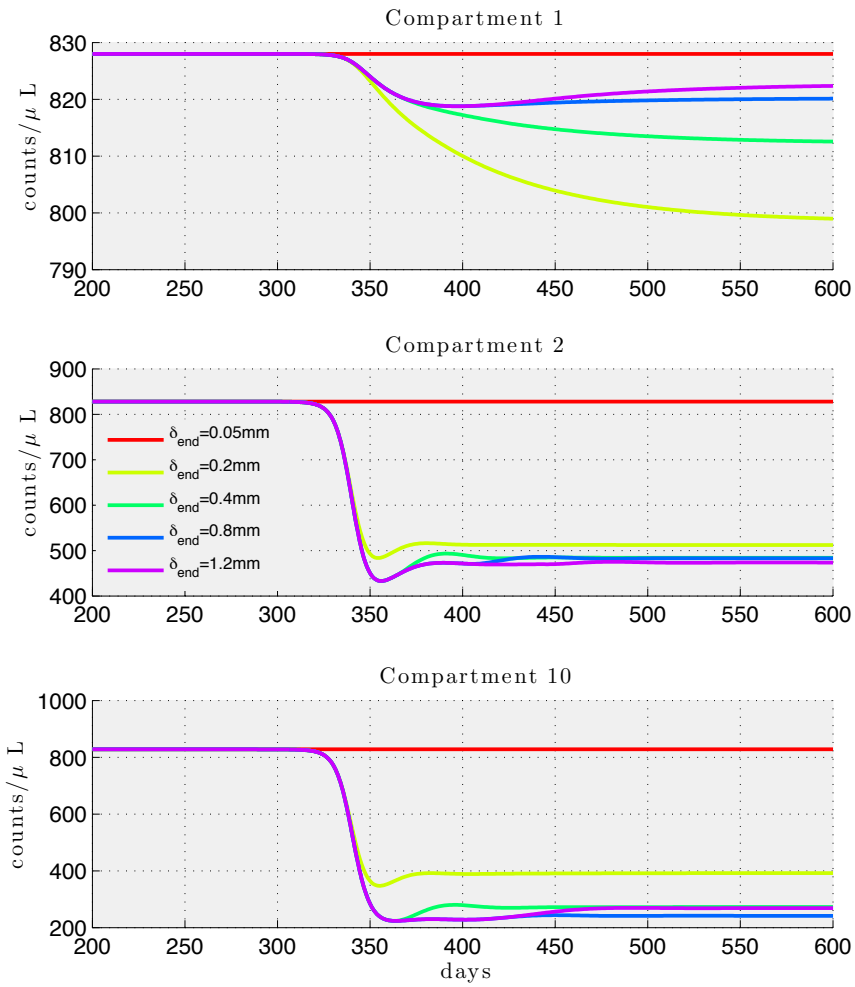

Figure 6.5: T cells concentration vs. final diameter. T cells concentration behaviors in compartment 1, 2, and 10 representing their concentration in the blood, the most external and interanl compartment in the sanctuary site. Opposite behaviors are presented in compartment 1 with respect to the others as the final diameter changes.

An explanation for these two contrasted behaviors is that the ability of T cells to move between the main and secondary compartments is different for different diameter sizes. Given that we assume the virus cannot move from the main compartment, the capacity of the virus to have supported replication in the first compartment depends

on how well infected cells are able to move there and thus spread new viruses. For smaller maximum diameters, T cells are better connected between compartments, can move faster to the first compartment and sustain there a steady state viral load over the limit of detection. As the maximum diameter increases, infected cells become more isolated from the main compartment, therefore fewer viruses are generated from this source and the transient viral blip results.

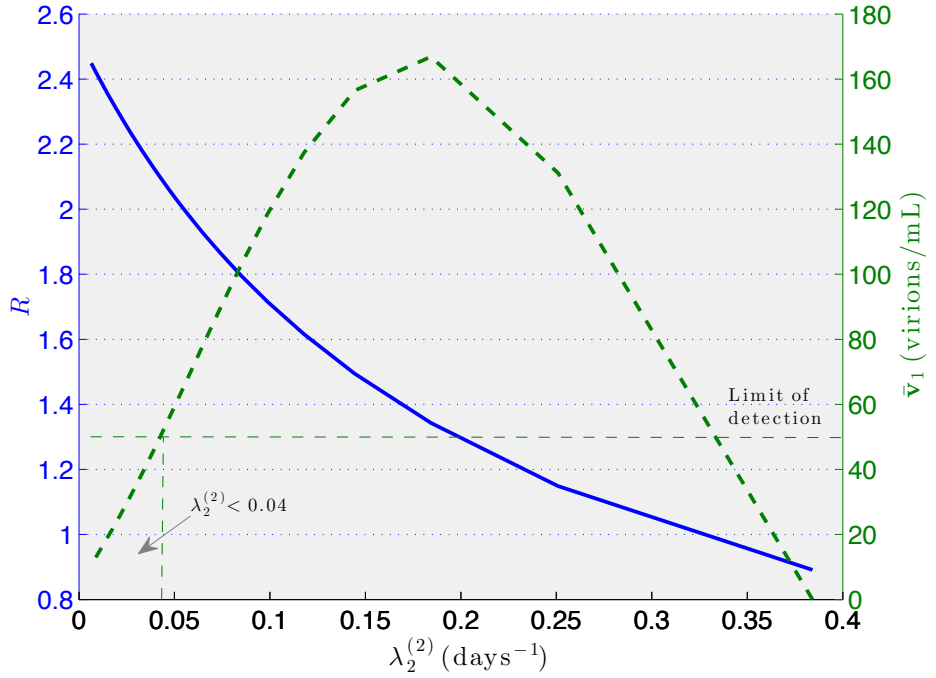

Figure 6.6: Final R and $\bar{\mathbf{v}}_1$ vs $\lambda_2^{(2)}$. In blue, the final value of R decreases as the connectivity coefficient $\lambda_2^{(2)}$ increases. High values of $\lambda_2^{(2)}$ imply small diameter that lead the system to $R < 1$ and suppressed virus. In green the steady state viral load in compartment 1, $\bar{\mathbf{v}}_1$. $\bar{\mathbf{v}}_1$ only has values below the limit of detection for very high and very low $\lambda_2^{(2)}$, meaning that viral blips occur in moderately connected compartments.

In our model, this cell connectivity among compartments is characterized by the parameter $\lambda_2^{(2)}$. Figure 6.6 presents in blue the final values of R, and in green the steady state viral load in compartment 1 as $\lambda_2^{(2)}$ changes. As shown in equation (6.8),

the values of R decreases as $\lambda_2^{(2)}$ increases. On the other hand, the steady state viral load in the main compartment increases as $\lambda_2^{(2)}$ increases in the beginning. However, at some point, as $\lambda_2^{(2)}$ continue growing the steady state viral load start to decrease. Therefore, for very high and very low connectivity, the viral load is not sustained in the main compartment. Nevertheless, for very high values of $\lambda_2^{(2)}$ the value of R is smaller than one, so that the remote compartment cannot sustain viral replication either. This is because high values of $\lambda_2^{(2)}$ result in small diameters of the compartment as seen in figure 6.7. An important question is, what would the minimum final diameter size be in order to have steady state viral load in compartment one below the limit of detection. As figure 6.6 and 6.7 show, for this particular R_0 case, the final diameter size should

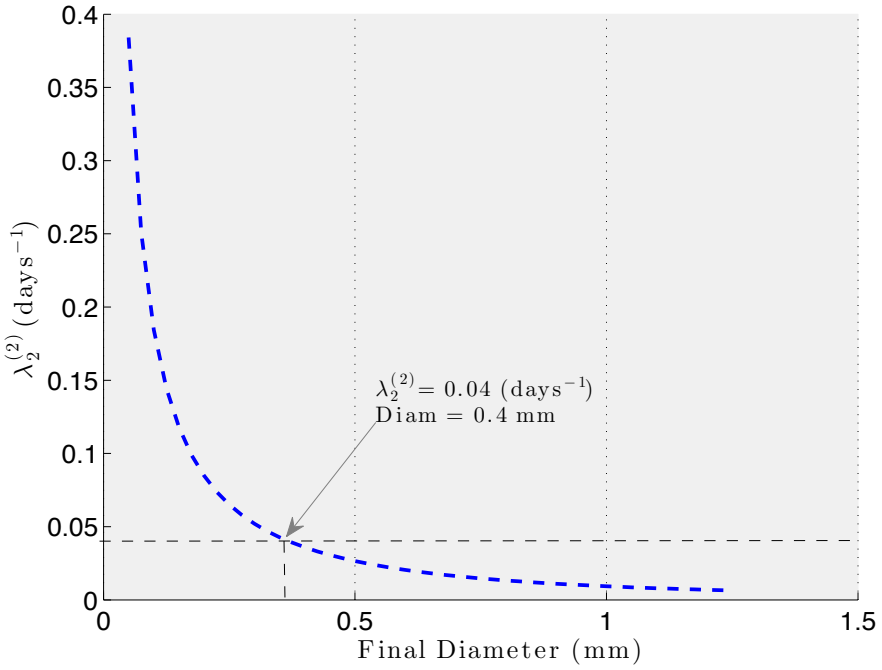

Figure 6.7: $\lambda_2^{(2)}$ vs final diameter. The connectivity of T cells in the system, $\lambda_2^{(2)}$, has a negative exponential relation with the final diameter. This concurs with the fact that recirculation of T cells happens in sites with smaller diameters.

need to be greater than 0.4 mm. So, this maximum diameters become larger than this, an viral blip occur. However, the question remains as to how this result might change as the value of R_0 and f_{max} change.

6.5 Effect of the Basic Reproductive Ratio in the Viral Blip

In this section, we present a generalization of the previous results for different values of R_0. Because f_{max} represents the proportion of the infection that is unaffected by the drug in the more distant compartment, f_{max} is very close to 1. The only other parameter relevant in the behavior of viral blips is R_0. To understand how the values of R_0 could modify the results of the previous section we perform the following simulations. We select randomly the T-cell/HIV parameter rates from the posterior distributions estimated in [48], such that for a fixed $\delta_{min} = 0.04\ mm$ the value of R remains smaller than one. For a specific set of T-cell/HIV parameters the value R_0 is computed. For each R_0 we compute two sets of simulations.

The first set is to describe how R_0 affects the boundaries of ξ to obtain viral blips with realistic amplitudes and duration over the limit of detection. Therefore, we tune the value of ξ from 0.015 to 0.05 days^{-1} with a fixed $\delta_{max} = 1.25$mm and simulate the model for each value of ξ, maintaining the remained parameters fixed as in the previous section and table 6.1. From this first set of simulations, we obtain values of the viral blip amplitude and duration over 50 $\frac{virions}{mL}$ in the first compartment in terms of ξ for each R_0.

Next, for each specific R_0, we compute the value of ξ needed for a viral blip of duration smaller than 30 days over the limit of detection with the maximum amplitude. Using this value of ξ, the second set of simulations aims to find how R_0 affects the final value of the diameter to have realistic viral blips with steady state below the limit of detection. Thus, in the second set of simulations, we stop the increase of the diameter when it reaches values from 0.05mm to 1.25mm, and maintaining the rest of the parameters as in the first set. From this set of simulations we obtain the steady state viral load in compartment one.

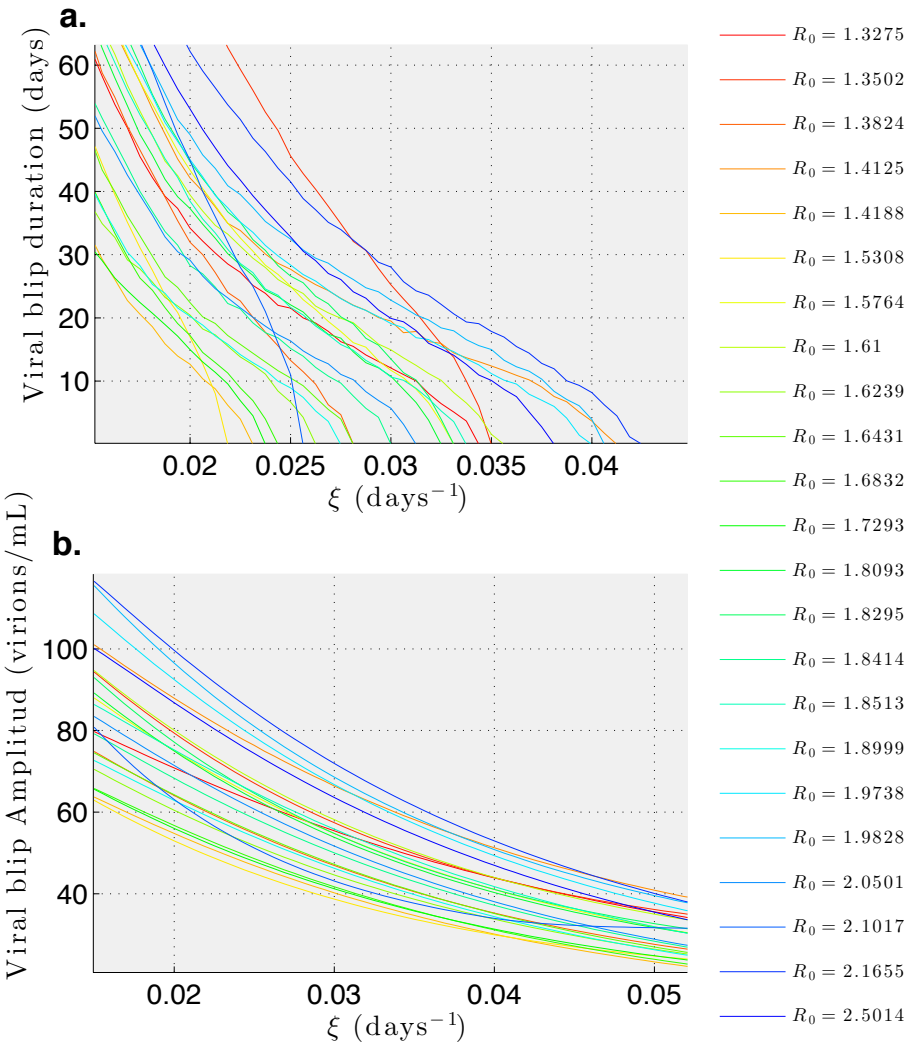

Figure 6.8: Generalization of viral blip duration and amplitude, vs. ξ for different R_0. The decreasing pattern of viral blip amplitude and duration does not change for different values of R_0. However, their minimum and maximum values are not correlated with R_0.

The results for the first set of simulations are presented in Figure 6.8 and 6.9. Figure 6.8a presents different behavior of viral blip duration over the limit of detection vs. ξ for different values of R_0. Notice that the viral blip duration vs. ξ behavior is not correlated with the value of R_0. On the other hand, as presented in figure 6.9, the

range for the minimum value of the diameter rise rate ξ_{min} to have at most at most a maximum viral blip duration of 30 days [23], is from 0.0156 days^{-1} to 0.0294 days^{-1} with a median of 0.0225 days^{-1}.

Figure 6.8b shows the behavior of the viral blip maximum amplitude vs. ξ for the different values of R_0. As for the viral blip duration, their amplitude behavior with respect to ξ is also not correlated with R_0. Moreover, to have an amplitude over the limit of detection (or viral blip duration greater than zero), the maximum value of the diameter rise rate ξ_{max} has a median of 0.0319 days^{-1} and ranges from 0.0212 days^{-1} to 0.0419 days^{-1} as shown in figure 6.9. Notice that the value of R_0 does not

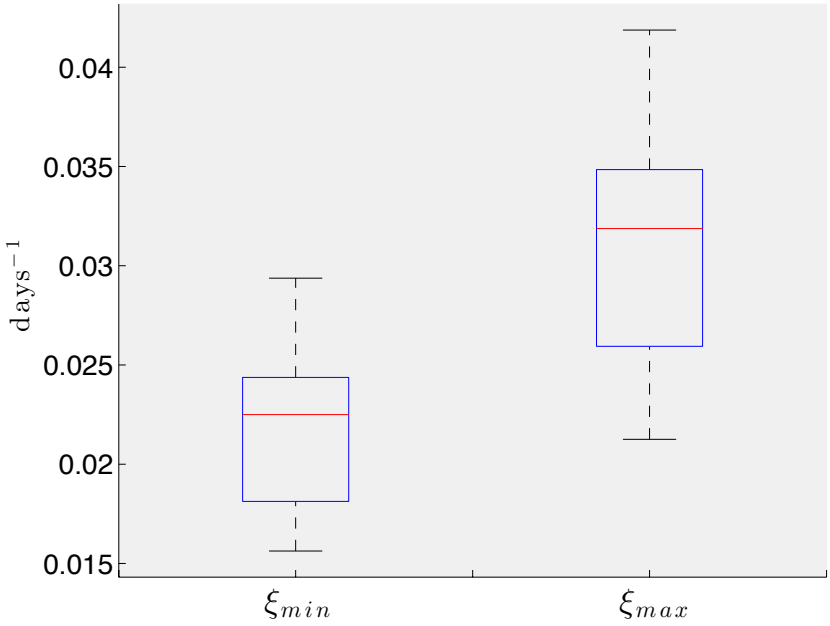

Figure 6.9: Ranges of ξ for several R_0. ξ_{min} and ξ_{max} represent the values of ξ for viral blips with a maximum duration of 30 days and minimum amplitude of 50 copies/mL for different values of R_0 respectively. The median value for ξ_{min} is 0.0225 days^{-1} and for ξ_{max}, 0.0319 days^{-1}.

change the pattern of the viral blip duration or amplitude presented in the previous

sections, but it set the range in which a realistic viral blip might occur following the characterization done in [23].

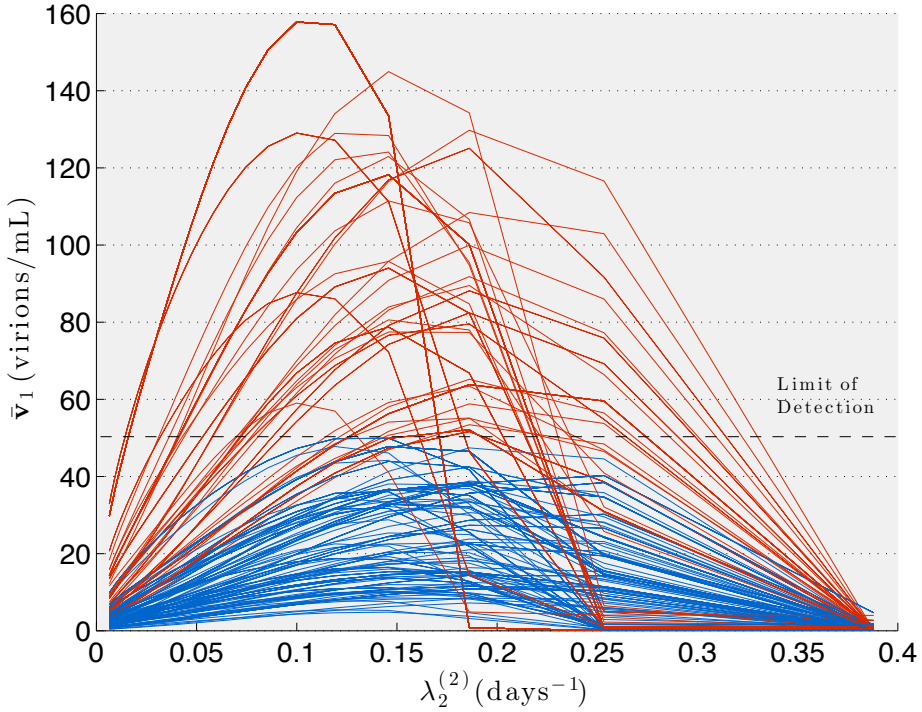

Figure 6.10: Viral blip steady state in comp. 1 $\bar{\mathbf{v}}_1$ vs $\lambda_2^{(2)}$ for different values of R_0. For every R_0 the pattern of $\bar{\mathbf{v}}_1$ was the similar, with low values for $\lambda_2^{(2)}$ low values. In blue, however, are the behaviors of $\bar{\mathbf{v}}_1$ with all their values below the limit of detection for R_0 around 1.4, regardless the value of $\lambda_2^{(2)}$. In red, $\bar{\mathbf{v}}_1$ has values over the limit of detection for some values of $\lambda_2^{(2)}$. These behaviors correspond for R_0 around 2.1.

For the second set of simulations, figure 6.10 shows the plot of the steady state viral load in compartment one vs the connectivity coefficient $\lambda_2^{(2)}$ for different values of R_0. Notice that the behavior of this steady state value for different R_0 is the same as in the previous section. Also, for 50% of the R_0 values (or virtual patients), regardless of the maximum diameter, the connectivity is never sufficient to allow a viral load steady state over the limit of detection in compartment one. As presented in figure 6.11, the

distribution for R_0 is different from the values of R_0 where the viral blip steady state can reach a value over the limit of detection in some values of $\lambda_2^{(2)}$. In the first set, the steady state viral load is always below the limit of detection, and the median value of R_0 is 1.45. For the second set, R_0 has a median of 2.1.

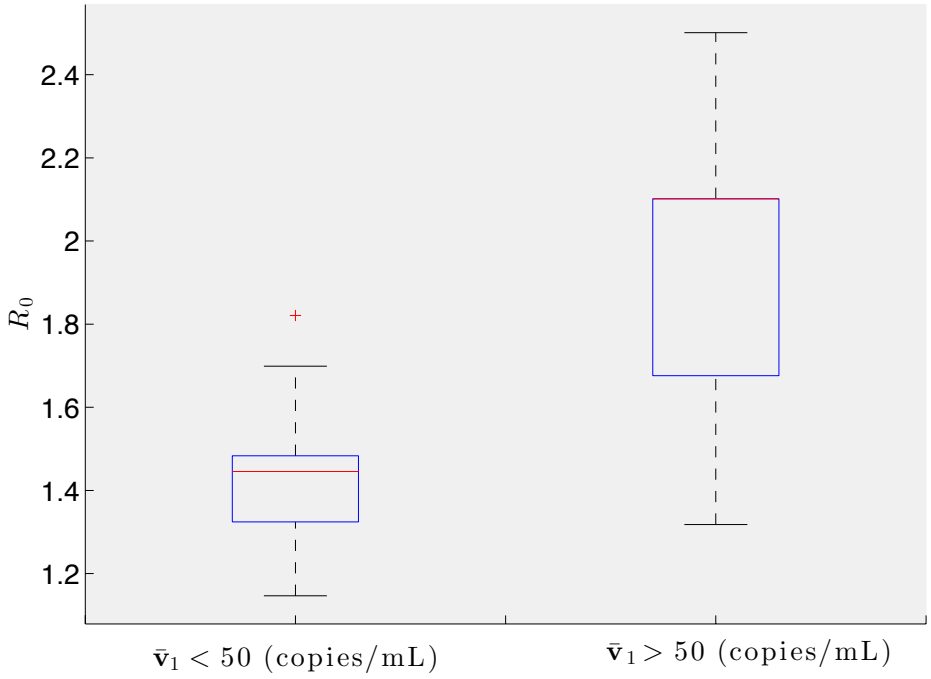

Figure 6.11: Distribution of R_0 with respect to $\bar{\mathbf{v}}_1$. The behavior of R_0 for $\bar{\mathbf{v}}_1 < 50$copies/mL has a median of 1.45 with a range from 1.15 to 1.82. Contrasted to them, the distribution of R_0 for $\bar{\mathbf{v}}_1 > 50$ copies/mL has a median of 2.1 with values from 1.32 to 2.5.

For the R_0 set with median 2.1, the minimum final diameter to have a steady state viral load in compartment one below the limit of detection depends on the value of ξ and is not correlated with R_0. As shown in figure 6.12, as ξ increases the minimum final diameter also increases, having values from 0.065mm to 0.775mm.

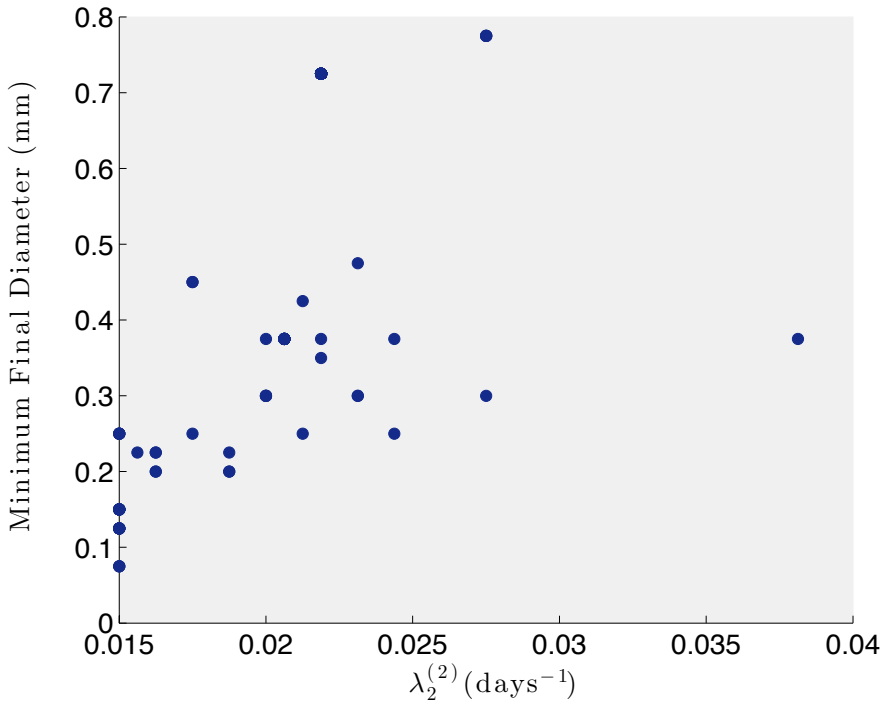

Figure 6.12: Minimum final diameter vs $\lambda_2^{(2)}$ for R_0 cases with $\bar{\mathbf{v}}_1 > 50$. The minimum final diameter required to have $\bar{\mathbf{v}}_1 < 50$ is positively correlated to $\lambda_2^{(2)}$. Their average diameter was 0.7mm, having values from 0.065mm to 0.775mm.

Thus, we have described, that according to this compartmental model, a diameter increase that leads to cryptic viremia in a lymphoid-base drug sanctuary, is a plausible theoretical explanation for the formation of viral blips. Viral blips, as presented in the literature, might occur in patients when the diameter of LN follicles with low drug penetration increases with rates ξ between 0.0225 and 0.0319 days^{-1}, and when the patient has a median of $R_0 = 2.1$, the diameter has to reach values greater than 0.7mm.

Chapter 7

CONCLUSIONS

The dynamics of HIV disruption of the adaptive immune system by infecting T helper cells is a complex process. Nevertheless it has been successfully articulated by simplified mathematical models, leading to the improvement of anti-retroviral therapy. Currently, viral persistence is the main challenge to attain a functional cure. The reactivation of latently infected cells is the main barrier to eradicating the virus. However, the formation of 2-LTR circles in PBMC after raltegravir intensification in some patients under cART, and the detection of low drug concentration in lymph nodes, strongly suggest that ongoing replication in lymphoid tissues be another obstacle for a cure. This dissertation presents a mathematical analysis of HIV-infection-spatial-dynamics in patients under cART and contributes to the understanding of viral persistence, and shows how ongoing replication in lymph nodes can be a factor. In addition, it gives insights as to how to improve clinical trials that can result in advance of future HIV treatment.

We have shown that a spatial, compartmental model of lymphoid follicles as sanctuary sites supporting ongoing viral replication is capable of reproducing the transient behavior of plasma HIV 2-LTR observed after application of raltegravir in patients undergoing cART therapy. Using Monte-Carlo methods, we explored the behavior of these sites across the feasible range of parameter values as determined from prior experimental data. The results demonstrated that the behavior of the compartments, and the dependence of the observed 2-LTR dynamics on the presence of locally uncontrolled cryptic viremia was robust to the uncertainty in the model parameters.

7.1 Conditions for Cryptic Viremia

We have shown that a necessary condition for the formation of a transient 2-LTR peak is a sufficiently low drug efficacy in the sanctuary site, such that the local reproductive ratio in the site is larger than 1. For the most restrictive scenario, with compartment diameters of 0.5 mm, the drug efficacy at the interface between the site and the blood/lymphatic sinus compartment $\hat{R}_{0_2}$ has to be greater than 0.93 to allow any significant level of HIV replication in the site.

The average combined-drug concentration lymph-node/blood ratio to sustain cryptic viremia should be less than 0.55. However, for either RTI or PI, if its ratio increases, the other drug ratio has to decrease almost linearly to sustain replication inside the lymph node and be considered a sanctuary site for cART. These drug penetration results are not inconsistent with previous data as reviewed in [20, 75] where their findings indicated ratios around 0.4 for RTIs and from 0.5 to 0.2 for PIs or smaller, and also as recently presented in [30]. Thus, we find that cryptic viremia is possible when total drug efficiency in lymph nodes is very low. On the other hand, if total drug penetration $\bar{\theta}_{LN} + \bar{\varphi}_{LN}$ is greater than 0.6, the percentage of cases to have cryptic viremia is always less than or equal to 10%.

A second necessary condition is that the individual lymphoid follicles are sufficiently large to support virus replication. For site diameters below 0.2 mm, fewer than 5% of the Monte-Carlo trials resulted in any significant virus replication in the site. If the total combined-drug penetration is smaller than 0.1 and the diameter is greater than 0.2 mm it is possible to have cryptic viremia in nearly 100% of the cases. As total drug penetration increases, the probability to have cryptic viremia decreases, but the percentages are higher for larger diameters. In general, the likelihood to have viral replication in lymph nodes follicles with diameters greater than 0.2 mm and with total drug penetration smaller than 0.5 is around 95%.

Larger follicular diameters have been reported previously in patients under cART with no detectable blood viral load. For instance, the work in [61] showed hyperplastic follicles even up to 1 mm for 3 of 9 patients after six months of treatment.

In fact, a study reported in [1] found for some patients under cART, hyperplastic follicles oscillating up to 1.23 mm^2 in 12 months and 0.33 mm^2 in 36 months. These results corresponds approximately to diameters from 0.65 to 1.25 mm, in the range of possible cryptic viremia according to the model. Therefore, we suggest, if sufficiently low drug penetration inside lymph nodes is present; follicles with these diameters are able to sustain viral replication.

7.2 Conditions for a Transient 2-LTR Formation and Cryptic Viremia

If the sites are sufficiently large, and have sufficiently low antiviral activity to allow efficient replication of HIV within the site, than the addition of raltegravir resulted in the transient production of 2-LTR circles within the site. Detectable 2-LTR peaks in the blood require that the total volume of sanctuary site tissue also be large enough that the diffusion of these 2-LTR from the sites into the blood occur at a rate large enough to bring the observed peak in the blood above the limit of detection, approximately 1.2 2-LTR circles per 10^6 PBMC. If the total infected cell turnover in the sites was greater than 10^6 infected cells per day, then, the observed peak in plasma 2-LTR would be above the limit of detection over 95% of the time. For infected cell turnover rates in the sanctuary sites as high as 2×10^8 infected cells per day, there was no measurable contribution of virus to compartment 1, neither was there any measurable change in the predicted plasma viral load following integrase inhibitor intensification, despite orders-of-magnitude reductions in the total infected cell turnover rates following intensification. Moreover, as the maximum amount of 2-LTR circles per 10^6 PBMC increases, the drug penetration distribution gets tighter with median around 0.1, implying that there is less drug penetration when a 2-LTR circles peak increases. This is consistent with the efficient viremia in the sanctuary sites being cryptic, undetectable from standard plasma viral load assays.

We have further shown that when the antiviral activity within the sites is sufficiently high, such that $R_0 < 1$ everywhere, it is impossible to produce a transient 2-LTR curve following raltegravir intensification. Under these conditions, the only possible

2-LTR dynamics following raltegravir intensification must lead to a monotonic increase of 2-LTR in compartment 1. For the range of parameters considered in our Monte-Carlo study, this monotonic increase never resulted in a 2-LTR concentration above the limit of detection of 1.2 2-LTR per 10^6 PBMC.

In the INTEGRAL study [11], 13 out of 45 patients exhibited measurable 2-LTR peaks in their blood following raltegravir intensification. These 2-LTR dynamics followed a characteristic pattern with a dramatic peak at week 2, decaying below baseline by week 24. Our model is able to reproduce these dynamics if and only if reduced drug activity in anatomically isolated sanctuary sites enables high levels of efficient cryptic HIV replication. The median observed 2-LTR peak at week 2 from the 13 patients was 5.8 2-LTR per 10^6 PBMC. If the assumptions of our spatial model are correct, this would correspond to a pre-intensification cryptic replication rate of between 2×10^6 and 2×10^7 infected cells per day. The highest measured peak among the 13 patients was 72.8 2-LTR per 10^6 PBMC; this would correspond to a pre-intensification cryptic replication rate of between 3×10^7 and 3×10^8 infected cells per day.

7.3 2-LTR Decay Rate Bias

Based on Monte-Carlo simulations, we showed those for which the 2-LTR behaviors in compartment one got the best fit to the INTEGRAL data. From these, we showed that 2-LTR transient behavior in the blood can have decay rates with an average of 0.05 days^{-1} when the spatial dynamics of sanctuary sites hypothesis is considered. This value has almost an order of magnitude smaller than our previous estimation of 0.46 days^{-1}, but more in agreement with previous experimental estimation for 2-LTR half-life between 8 and 25 days [82, 57]. This suggest that previous estimations of 2-LTR half-life, as done in [47], fitting INTEGRAL study data to a single-compartment model, can result in a bias because it did not consider spatial dynamics. Thus, there is concern that by neglecting T-cells recirculation 2-LTR circles half-life might be underestimated.

We presented a MCMC-Bayesian analysis to compute the bias by estimation of 2-LTR in PBMC decay rate δ for two specific realistic scenarios of limited 2-LTR data in PBMC after raltegravir intensification in patients under cART. These two scenarios were virtually created following a first sampling schedule as presented in Buzon et al. [11], and a second assuming a more frequent, but feasible and realistic scenario. The estimation processes used follows the same procedure presented in [47] to estimate δ using real data. As we hypothesized, neglecting T-cells recirculation yield to underestimation of this value having a bias up to 0.2 days^{-1}, but can be decreased if more early points are added. These results have important implications for designing future clinical trials and the estimation of parameters as the 2-LTR decay rate, to be used for possible measurements of cryptic viremia. The bias computed by this method is influenced by the way the sampling schedule is designed and in how the parameter estimation is done. Neglecting explicitly physiological process in the single-compartment model leads to less accurate results because of a larger bias.

7.4 Conditions for Viral Blips and Cryptic Viremia

For low drug concentrations there is a critical size in order for cryptic viremia to exist in sanctuary sites. We have shown as the diameter of site increases, a viral blips occurs. We presented that there can be blips that do not cross the limit of detection, but could affect the mean of the viral load with possible variability over the limit of detection.

Therefore, we developed theoretical conditions of viremia suppression below the limit of detection in all compartments, that depend on the size of the site by using a s-shape model for diameter increase in time. The behavior of the amplitude and the duration of the viral blip behaves inversely to how fast the diameter increase in time. The faster the diameter increases the lower the amplitude of the viral blip and shorter its duration over the limit of detection. Thus, to have realistic viral blips as in the literature [23], with duration less 30 days and with amplitudes relative close to the limit of detection, the diameter rise should have rates between 0.02 and 0.03 days^{-1}.

Also, the final diameter of the site affects different steady states of the virus load after the blip. When the steady state viral load after the blip always is below the limit of detection, the median value of R_0 is 1.45, and this situation correspond to the 50% of the simulations run. However for the other cases, when R_0 increases with median $R_0 = 2.1$, the steady state of the viral load after the blip might have values over the limit of detection for some final maximum diameters. We presented that the capacity of T cells to move between the main and secondary compartments (the sanctuary) can be characterized and is different for different final diameters. Given that we assume the virus cannot move from the main compartment, the capacity of the virus to have sustained replication in the first compartment depends also on how infected cells can move to that compartment and spread new viruses. For smaller maximum diameters, T cells are better connected between compartments, can move faster to the first compartment and sustain there a steady state viral load over the limit of detection. As the maximum diameter increases, infected cells start to be more isolated from the main compartment, therefore smaller amount of the virus is spread from this source and the transient viral blip is formed. In this cases, the maximum final diameters should be greater than 0.7mm to have relative lost of connection between compartments and have a realistic viral blip.

7.5 Future Work

High viral replication rates will certainly result in the production of novel viral mutants which may result in accelerated treatment failure. The contribution of the cryptic viremia to the development of resistance-based treatment failure will depend on many factors. The degree of residual activity of the antivirals in the sanctuary site will affect how strongly the resistance mutations are selected within the site, and the diffusion rates between the site and the blood will determine whether intermediate mutations are likely to be observed in blood-based assays before a full escape mutant is generated. Future work will focus on developing a predictive model for the evolution of resistance in the presence of cryptic viremia.

BIBLIOGRAPHY

[1] L Alos, P Navarrete, V Morente, F Garcia, M Garrido, M Plana, A Mozos, A Lopez, C Gil, T Pumarola, M Caballero, J L Blanch, E Fumero, J M Miró, T Gallart, J M Gatell, and E Campo. Immunoarchitecture of lymphoid tissue in HIV-infection during antiretroviral therapy correlates with viral persistence. *Modern Pathology*, 18(1):127–136, January 2005.

[2] Z Aminzare, Y Shafi, M Arcak, and E D Sontag. Guaranteeing spatial uniformity in reaction-diffusion systems using weighted L_2-norm contractions. In V Kulkarni, G B Stan, and K Raman, editors, *A Systems Theoretic Approach to Systems and Synthetic Biology: Models and System Characterizations*, page To appear. 2014.

[3] Jeffrey A Anderson, Nancie M Archin, William Ince, Daniel Parker, Ann Wiegand, John M Coffin, Joann Kuruc, Joseph Eron, Ronald Swanstrom, and David M Margolis. Clonal sequences recovered from plasma from patients with residual HIV-1 viremia and on intensified antiretroviral therapy are identical to replicating viral RNAs recovered from circulating resting CD4+ T cells. *J Virol*, 85(10):5220–5223, May 2011.

[4] Murat Arcak. Certifying spatially uniform behavior in reaction–diffusion PDE and compartmental ODE systems. *Automatica*, 47(6):1219–1229, June 2011.

[5] Valentina Baldazzi, Paola Paci, Massimo Bernaschi, and Filippo Castiglione. Modeling lymphocyte homing and encounters in lymph nodes. *BMC Bioinformatics*, 10:387, 2009.

[6] Caroline Bazzoli, Vincent Jullien, Clotilde Le Tiec, Elisabeth Rey, France Mentré, and Anne-Marie Taburet. Intracellular Pharmacokinetics of Antiretroviral Drugs in HIV-Infected Patients, and their Correlation with Drug Action. *Clin Pharmacokinet*, 49(1):17–45, January 2010.

[7] Joost B Beltman, Athanasius F M Marée, Jennifer N Lynch, Mark J Miller, and Rob J De Boer. Lymph node topology dictates T cell migration behavior. *J Exp Med*, 204(4):771–780, April 2007.

[8] Andrzej Bielecki and Piotr Kalita. Model of neurotransmitter fast transport in axon terminal of presynaptic neuron. *Journal of Mathematical Biology*, 56(4):559–576, April 2008.

[9] Andrzej Bielecki, Piotr Kalita, Marian Lewandowski, and Marek Skomorowski. Compartment model of neuropeptide synaptic transport with impulse control. *Biol Cybern*, 99(6):443–458, December 2008.

[10] Maria J Buzón, Francisco M Codoñer, Simon D W Frost, Christian Pou, Maria C Puertas, Marta Massanella, Judith Dalmau, Josep M Llibre, Mario Stevenson, Julià Blanco, Bonaventura Clotet, Roger Paredes, and Javier Martinez-Picado. Deep Molecular Characterization of HIV-1 Dynamics under Suppressive HAART. *PLoS Pathog.*, 7(10), October 2011.

[11] Maria J Buzón, Marta Massanella, Josep M Llibre, Anna Esteve, Viktor Dahl, Maria C Puertas, Josep M Gatell, Pere Domingo, Roger Paredes, Mark Sharkey, Sarah Palmer, Mario Stevenson, Bonaventura Clotet, Julià Blanco, and Javier Martinez-Picado. HIV-1 replication and immune dynamics are affected by raltegravir intensification of HAART-suppressed subjects. *Nat Med*, 16(4):460–465, April 2010.

[12] Duncan S Callaway and Alan S Perelson. HIV-1 infection and low steady state viral loads. *Bull Math Biol*, 64(1):29–64, January 2002.

[13] E. Fabian Cardozo, Rutao Luo, Michael J Piovoso, and Ryan Zurakowski. Spatial modeling of HIV cryptic viremia and 2-LTR formation during raltegravir intensification. *J Theor Biol*, 345C:61–69, December 2013.

[14] E. Fabian Cardozo, Cesar A Vargas, and Ryan Zurakowski. A Compartment Based Model for the Formation of 2-LTR Circles after Raltegravir Intensification. In *51st IEEE Conference on Decision and Control*, pages 4924–4929, Maui, HI, December 2012.

[15] Pedro Castro, Montserrat Plana, Raquel González, Anna López, Anna Vilella, Jose M Nicolas, Teresa Gallart, Tomás Pumarola, José M Bayas, JosÈ M Gatell, and Felipe Garcia. Influence of episodes of intermittent viremia ("blips") on immune responses and viral load rebound in successfully treated HIV-infected patients. *AIDS Res Hum Retroviruses*, 29(1):68–76, January 2013.

[16] T W Chun, R T Davey, M Ostrowski, J Shawn Justement, D Engel, J I Mullins, and A S Fauci. Relationship between pre-existing viral reservoirs and the reemergence of plasma viremia after discontinuation of highly active anti-retroviral therapy. *Nat Med*, 6(7):757–761, July 2000.

[17] T W Chun, L Stuyver, S B Mizell, L A Ehler, J A Mican, M Baseler, A L Lloyd, M A Nowak, and A S Fauci. Presence of an inducible HIV-1 latent reservoir during highly active antiretroviral therapy. *Proc Natl Acad Sci USA*, 94(24):13193–13197, November 1997.

[18] Jon Cohen. HIV/AIDS research. Tissue says blood is misleading, confusing HIV cure efforts. *Science*, 334(6063):1614, December 2011.

[19] Jessica M Conway and Daniel Coombs. A stochastic model of latently infected cell reactivation and viral blip generation in treated HIV patients. *PLoS Comput Biol*, 7(4):e1002033, April 2011.

[20] Theodore J Cory, Timothy W Schacker, Mario Stevenson, and Courtney V Fletcher. Overcoming pharmacologic sanctuaries. *Curr Opin HIV AIDS*, 8(3):190–195, May 2013.

[21] L Katie Crosley, Susan J Duthie, Abigael C Polley, Freek G Bouwman, Carolin Heim, Francis Mulholland, Graham Horgan, Ian T Johnson, Edwin C Mariman, Ruan M Elliott, Hannelore Daniel, and Baukje de Roos. Variation in protein levels obtained from human blood cells and biofluids for platelet, peripheral blood mononuclear cell, plasma, urine and saliva proteomics. *Genes Nutr*, 4(2):95–102, June 2009.

[22] Viktor Dahl, Lina Josefsson, and Sarah Palmer. HIV reservoirs, latency, and reactivation: prospects for eradication. *Antiviral Res*, 85(1):286–294, January 2010.

[23] Michele Di Mascio, Martin Markowitz, Michael Louie, Christine Hogan, Arlene Hurley, Chris Chung, David D Ho, and Alan S Perelson. Viral blip dynamics during highly active antiretroviral therapy. *J Virol*, 77(22):12165–12172, November 2003.

[24] Michele Di Mascio, Martin Markowitz, Michael Louie, Arlene Hurley, Christine Hogan, Viviana Simon, Dean Follmann, David D Ho, and Alan S Perelson. Dynamics of intermittent viremia during highly active antiretroviral therapy in patients who initiate therapy during chronic versus acute and early human immunodeficiency virus type 1 infection. *J Virol*, 78(19):10566–10573, October 2004.

[25] Michele Di Mascio, Sharat Srinivasula, Abesh Bhattacharjee, Lily Cheng, Lucia Martiniova, Peter Herscovitch, Juan Lertora, and Dale Kiesewetter. Antiretroviral Tissue Kinetics: In Vivo Imaging Using Positron Emission Tomography. *Antimicrob. Agents Chemother.*, 53(10):4086–4095, October 2009.

[26] G Dornadula, H Zhang, B VanUitert, J Stern, L Livornese, M J Ingerman, J Witek, R J Kedanis, J Natkin, J DeSimone, and R J Pomerantz. Residual HIV-1 RNA in blood plasma of patients taking suppressive highly active antiretroviral therapy. *JAMA*, 282(17):1627–1632, November 1999.

[27] Kristian Dreij, Qasim Ali Chaudhry, Bengt Jernstrm, Ralf Morgenstern, and Michael Hanke. A method for efficient calculation of diffusion and reactions of lipophilic compounds in complex cell geometry. *PLoS ONE*, 6(8):e23128, 08 2011.

[28] Teresa H Evering, Saurabh Mehandru, Paul Racz, Klara Tenner-Racz, Michael A Poles, Amir Figueroa, Hiroshi Mohri, and Martin Markowitz. Absence of HIV-1 evolution in the gut-associated lymphoid tissue from patients on combination antiviral therapy initiated during primary infection. *PLoS Pathog.*, 8(2):e1002506, February 2012.

[29] D Finzi, M Hermankova, T Pierson, L M Carruth, C Buck, R E Chaisson, T C Quinn, K Chadwick, J Margolick, R Brookmeyer, J Gallant, M Markowitz, D D Ho, D D Richman, and R F Siliciano. Identification of a reservoir for HIV-1 in patients on highly active antiretroviral therapy. *Science*, 278(5341):1295–1300, November 1997.

[30] Courtney V Fletcher, Kathryn Staskus, Stephen W Wietgrefe, Meghan Rothenberger, Cavan Reilly, Jeffrey G Chipman, Greg J Beilman, Alexander Khoruts, Ann Thorkelson, Thomas E Schmidt, Jodi Anderson, Katherine Perkey, Mario Stevenson, Alan S Perelson, Daniel C Douek, Ashley T Haase, and Timothy W Schacker. Persistent HIV-1 replication is associated with lower antiretroviral drug concentrations in lymphatic tissues. *Proc Natl Acad Sci U S A*, 111(6):2307–2312, February 2014.

[31] Joy M Folkvord, Carl Armon, and Elizabeth Connick. Lymphoid follicles are sites of heightened human immunodeficiency virus type 1 (HIV-1) replication and reduced antiretroviral effector mechanisms. *AIDS Res Hum Retroviruses*, 21(5):363–370, May 2005.

[32] Brian Friedrich, Guangyu Li, Natallia Dziuba, and Monique R Ferguson. Quantitative PCR used to assess HIV-1 integration and 2-LTR circle formation in human macrophages, peripheral blood lymphocytes and a CD4+ cell line. *Virol. J.*, 7:354, 2010.

[33] SDW Frost, J Martinez-Picado, L Ruiz, B Clotet, and AJL Brown. Viral dynamics during structured treatment interruptions of chronic human immunodeficiency virus type 1 infection. *J Virol*, 76(3):968–979, February 2002.

[34] Rajesh T Gandhi, Robert W Coombs, Ellen S Chan, Ronald J Bosch, Lu Zheng, David M Margolis, Sarah Read, Beatrice Kallungal, Ming Chang, Erin A Goecker, Ann Wiegand, Mary Kearney, Jeffrey M Jacobson, Richard D'Aquila, Michael M Lederman, John W Mellors, Joseph J Eron, and AIDS Clinical Trials Group (ACTG) A5244 Team. No effect of raltegravir intensification on viral replication markers in the blood of HIV-1-infected patients receiving antiretroviral therapy. *J Acquir Immune Defic Syndr*, 59(3):229–235, March 2012.

[35] Rajesh T Gandhi, Lu Zheng, Ronald J Bosch, Ellen S Chan, David M Margolis, Sarah Read, Beatrice Kallungal, Sarah Palmer, Kathy Medvik, Michael M Lederman, Nadia Alatrakchi, Jeffrey M Jacobson, Ann Wiegand, Mary Kearney,

John M Coffin, John W Mellors, Joseph J Eron, and AIDS Clinical Trials Group A5244 team. The effect of raltegravir intensification on low-level residual viremia in HIV-infected patients on antiretroviral therapy: a randomized controlled trial. *PLoS Med*, 7(8), 2010.

[36] Jean-Philippe Girard, Christine Moussion, and Reinhold Förster. HEVs, lymphatics and homeostatic immune cell trafficking in lymph nodes. *Nat Rev Immunol*, 12(11):762–773, November 2012.

[37] J Troy Grennan, Mona R Loutfy, DeSheng Su, P Richard Harrigan, Curtis Cooper, Marina Klein, Nima Machouf, Julio S G Montaner, Sean Rourke, Christos Tsoukas, Bob Hogg, Janet Raboud, and CANOC Collaboration. Magnitude of virologic blips is associated with a higher risk for virologic rebound in HIV-infected individuals: a recurrent events analysis. *J Infect Dis*, 205(8):1230–1238, April 2012.

[38] Hiroyu Hatano, Matthew C Strain, Rebecca Scherzer, Peter Bacchetti, Deborah Wentworth, Rebecca Hoh, Jeffrey N Martin, Joseph M McCune, James D Neaton, Russell P Tracy, Priscilla Y Hsue, Douglas D Richman, and Steven G Deeks. Increase in 2-long terminal repeat circles and decrease in D-dimer after raltegravir intensification in patients with treated HIV infection: a randomized, placebo-controlled trial. *J Infect Dis*, 208(9):1436–1442, November 2013.

[39] D D Ho, A U Neumann, A S Perelson, W Chen, J M Leonard, and M Markowitz. Rapid turnover of plasma virions and CD4 lymphocytes in HIV-1 infection. *Nature*, 373(6510):123–126, January 1995.

[40] Mariko Horiike, Shingo Iwami, Makoto Kodama, Akihiko Sato, Yuji Watanabe, Mika Yasui, Yuki Ishida, Takeshi Kobayashi, Tomoyuki Miura, and Tatsuhiko Igarashi. Lymph nodes harbor viral reservoirs that cause rebound of plasma viremia in SIV-infected macaques upon cessation of combined antiretroviral therapy. *Virology*, 423(2):107–118, February 2012.

[41] Roger A Horn and Charles R Johnson. *Topics in matrix analysis*. Cambridge University Press, Cambridge, 1994.

[42] Laura E Jones and Alan S Perelson. Transient viremia, plasma viral load, and reservoir replenishment in HIV-infected patients on antiretroviral therapy. *J Acquir Immune Defic Syndr*, 45(5):483–493, August 2007.

[43] D Kirschner, G F Webb, and M Cloyd. Model of HIV-1 disease progression based on virus-induced lymph node homing and homing-induced apoptosis of CD4+ lymphocytes. *J Acquir Immune Defic Syndr*, 24(4):352–362, August 2000.

[44] J P Kraehenbuhl. The gut-associated lymphoid tissue: a major site of HIV replication and CD4 cell loss. *Trends in Microbiology*, 6(11):419–20– discussion 420–1, November 1998.

[45] A Lafeuillade, H Khiri, S Chadapaud, G Hittinger, and P Halfon. Persistence of HIV-1 resistance in lymph node mononuclear cell RNA despite effective HAART. *AIDS*, 15(15):1965–1969, October 2001.

[46] Bonnie E Lai, Marcus H Henderson, Jennifer J Peters, David K Walmer, and David F Katz. Transport theory for HIV diffusion through in vivo distributions of topical microbicide gels. *Biophys. J.*, 97(9):2379–2387, November 2009.

[47] Rutao Luo, E. Fabian Cardozo, Michael J Piovoso, Hulin Wu, Maria J Buzón, Javier Martinez-Picado, and Ryan Zurakowski. Modelling HIV-1 2-LTR dynamics following raltegravir intensification. *J R Soc Interface*, 10(84):20130186, 2013.

[48] Rutao Luo, Michael J Piovoso, Javier Martinez-Picado, and Ryan Zurakowski. HIV model parameter estimates from interruption trial data including drug efficacy and reservoir dynamics. *PLoS ONE*, 7(7):e40198, July 2012.

[49] Rutao Luo, Michael J Piovoso, and Ryan Zurakowski. Modeling uncertainty in single-copy assays for HIV. *J. Clin. Microbiol.*, 50(10):3381–3382, July 2012.

[50] E B S Marinho, F S Bacelar, and R F S Andrade. A model of partial differential equations for HIV propagation in lymph nodes. *Physica A: Statistical Mechanics and its Applications*, 391(1-2):132–141, January 2012.

[51] Valérie Martinez, Anne-Geneviève Marcelin, Jean-Pierre Morini, Jean Deleuze, Anne Krivine, Isabelle Gorin, Sabine Yerly, Luc Perrin, Gilles Peytavin, Vincent Calvez, and Nicolas Dupin. HIV-1 intermittent viraemia in patients treated by non-nucleoside reverse transcriptase inhibitor-based regimen. *AIDS*, 19(10):1065–1069, July 2005.

[52] JL Martinez-Cajas and MA Wainberg. Antiretroviral therapy: optimal sequencing of therapy to avoid resistance. *Drugs*, 68(1):43–72, 2008.

[53] Henry P Mirsky, Mark J Miller, Jennifer J Linderman, and Denise E Kirschner. Systems biology approaches for understanding cellular mechanisms of immunity in lymph nodes during infection. *J Theor Biol*, 287:160–170, October 2011.

[54] Scott N Mueller, Thomas Gebhardt, Francis R Carbone, and William R Heath. Memory T cell subsets, migration patterns, and tissue residence. *Annu Rev Immunol*, 31:137–161, 2013.

[55] Thomas T. Murooka, Maud Deruaz, Francesco Marangoni, Vladimir D. Vrbanac, Edward Seung, Ulrich H. von Andrian, Andrew M. Tager, Andrew D. Luster, and Thorsten R. Mempel. HIV-infected T cells are migratory vehicles for viral dissemination. *Nature*, 490(7419):283–287, October 2012.

[56] A G Murray and G A Jackson. Viral dynamics: a model of the effects of size, shape, motion and abundance of single-celled planktonic organisms and other particles. *Mar. Ecol. Prog. Ser.*, 89:103–116, November 1992.

[57] John M Murray, Kristin McBride, Christoph Boesecke, Michelle Bailey, Janaki Amin, Kazuo Suzuki, David Baker, John J Zaunders, Sean Emery, David A Cooper, Kersten K Koelsch, Anthony D Kelleher, and PINT STUDY TEAM. Integrated HIV DNA accumulates prior to treatment while episomal HIV DNA records ongoing transmission afterwards. *AIDS*, 26(5):543–550, March 2012.

[58] Richard E Nettles, Tara L Kieffer, Patty Kwon, Daphne Monie, Yefei Han, Teresa Parsons, Joseph Cofrancesco, Joel E Gallant, Thomas C Quinn, Brooks Jackson, Charles Flexner, Kathryn Carson, Stuart Ray, Deborah Persaud, and Robert F Siliciano. Intermittent HIV-1 viremia (Blips) and drug resistance in patients receiving HAART. *JAMA*, 293(7):817–829, February 2005.

[59] Thomas W North, Joanne Higgins, Jesse D Deere, Timothy L Hayes, Andradi Villalobos, Lourdes Adamson, Barbara L Shacklett, Raymond F Schinazi, and Paul A Luciw. Viral sanctuaries during highly active antiretroviral therapy in a nonhuman primate model for AIDS. *J Virol*, 84(6):2913–2922, March 2010.

[60] MA Nowak and RM May. *Virus Dynamics: Mathematical Principles of Immunology and Virology*. New York, 2000.

[61] J M Orenstein, M Feinberg, C Yoder, L Schrager, J M Mican, D J Schwartzentruber, R T Davey, R E Walker, J Falloon, J A Kovacs, K D Miller, C Fox, J A Metcalf, H Masur, and M A Polis. Lymph node architecture preceding and following 6 months of potent antiviral therapy: follicular hyperplasia persists in parallel with p24 antigen restoration after involution and CD4 cell depletion in an AIDS patient. *AIDS*, 13(16):2219–2229, November 1999.

[62] G Pantaleo, C Graziosi, L Butini, P A Pizzo, S M Schnittman, D P Kotler, and A S Fauci. Lymphoid organs function as major reservoirs for human immunodeficiency virus. *Proc Natl Acad Sci USA*, 88(21):9838–9842, November 1991.

[63] Kristine B Patterson, Heather A Prince, Trenton Stevens, Nicholas J Shaheen, Evan S Dellon, Ryan D Madanick, Steven Jennings, Myron S Cohen, and Angela D M Kashuba. Differential penetration of raltegravir throughout gastrointestinal tissue: implications for eradication and cure. *AIDS*, 27(9):1413–1419, June 2013.

[64] Alan S Perelson and Ruy M Ribeiro. Modeling the within-host dynamics of HIV infection. *BMC Biol.*, 11:96, 2013.

[65] Alan S Perelson and Frederik W Wiegel. Scaling aspects of lymphocyte trafficking. *J Theor Biol*, 257(1):9–16, March 2009.

[66] AS Perelson, P Essunger, and DD Ho. Dynamics of HIV-1 and CD4+ lymphocytes in vivo. *AIDS*, 11 Suppl A:S17–24, 1997.

[67] Mikulas Popovic, Klara Tenner-Racz, Colleen Pelser, Hans-Jürgen Stellbrink, Jan van Lunzen, George Lewis, Vaniambadi S Kalyanaraman, Robert C Gallo, and Paul Racz. Persistence of HIV-1 structural proteins and glycoproteins in lymph nodes of patients under highly active antiretroviral therapy. *Proc Natl Acad Sci USA*, 102(41):14807–14812, October 2005.

[68] Sandrine Reigadas, Marie-Line Andréola, Linda Wittkop, Ophélie Cosnefroy, Guerric Anies, Patricia Recordon-Pinson, Rodolphe Thiébaut, Bernard Masquelier, and Hervé Fleury. Evolution of 2-long terminal repeat (2-LTR) episomal HIV-1 DNA in raltegravir-treated patients and in in vitro infected cells. *J Antimicrob Chemother*, 65(3):434–437, March 2010.

[69] Libin Rong and Alan S Perelson. Modeling HIV persistence, the latent reservoir, and viral blips. *J Theor Biol*, 260(2):308–331, September 2009.

[70] Libin Rong and Alan S Perelson. Modeling latently infected cell activation: viral and latent reservoir persistence, and viral blips in HIV-infected patients on potent therapy. *PLoS Comput Biol*, 5(10):e1000533, October 2009.

[71] Mark Sharkey. Tracking episomal HIV DNA: implications for viral persistence and eradication of HIV. *Curr Opin HIV AIDS*, 8(2):93–99, March 2013.

[72] Mark Sharkey, Dunja Z Babic, Thomas Greenough, Roy Gulick, Daniel R Kuritzkes, and Mario Stevenson. Episomal viral cDNAs identify a reservoir that fuels viral rebound after treatment interruption and that contributes to treatment failure. *PLoS Pathog.*, 7(2):e1001303, February 2011.

[73] Mark Sharkey, Karine Triques, Daniel R Kuritzkes, and Mario Stevenson. In vivo evidence for instability of episomal human immunodeficiency virus type 1 cDNA. *J Virol*, 79(8):5203–5210, April 2005.

[74] Richard D Sloan and Mark A Wainberg. The role of unintegrated DNA in HIV infection. *Retrovirology*, 8:52, 2011.

[75] Caroline Solas, Alain Lafeuillade, Philippe Halfon, Stéphane Chadapaud, Gilles Hittinger, and Bruno Lacarelle. Discrepancies between protease inhibitor concentrations and viral load in reservoirs and sanctuary sites in human immunodeficiency virus-infected patients. *Antimicrob. Agents Chemother.*, 47(1):238–243, January 2003.

[76] M A Swartz. The physiology of the lymphatic system. *Adv. Drug Deliv. Rev.*, 50(1-2):3–20, August 2001.

[77] Melanie A Thompson, Judith A Aberg, Jennifer F Hoy, Amalio Telenti, Constance Benson, Pedro Cahn, Joseph J Eron, Huldrych F Günthard, Scott M Hammer, Peter Reiss, Douglas D Richman, Giuliano Rizzardini, David L Thomas, Donna M Jacobsen, and Paul A Volberding. Antiretroviral treatment of adult HIV infection: 2012 recommendations of the International Antiviral Society-USA panel. *JAMA*, 308(4):387–402, July 2012.

[78] Pål Voltersvik, Leif Bostad, Anne Margarita Dyrhol-Riise, Geir Egil Eide, Bård Ingvald Røsok, Jan Olofsson, and Birgitta Asjö. Cystatin A and HIV-1 p24 antigen expression in tonsillar lymphoid follicles during HIV-1 infection and during highly active antiretroviral therapy. *J Acquir Immune Defic Syndr*, 41(3):277–284, March 2006.

[79] Ulrich H von Andrian and Thorsten R Mempel. Homing and cellular traffic in lymph nodes. *Nat Rev Immunol*, 3(11):867–878, November 2003.

[80] X Wei, S K Ghosh, M E Taylor, V A Johnson, E A Emini, P Deutsch, J D Lifson, S Bonhoeffer, M A Nowak, and B H Hahn. Viral dynamics in human immunodeficiency virus type 1 infection. *Nature*, 373(6510):117–122, January 1995.

[81] J K Wong, M Hezareh, H F Günthard, D V Havlir, C C Ignacio, C A Spina, and D D Richman. Recovery of replication-competent HIV despite prolonged suppression of plasma viremia. *Science*, 278(5341):1291–1295, November 1997.

[82] Weijun Zhu, Yanmei Jiao, Rongyue Lei, Wei Hua, Rui Wang, Yunxia Ji, Zhiying Liu, Feili Wei, Tong Zhang, Xuanlin Shi, Hao Wu, and Linqi Zhang. Rapid turnover of 2-LTR HIV-1 DNA during early stage of highly active antiretroviral therapy. *PLoS ONE*, 6(6):e21081, 2011.

Appendix A

COMPUTATION OF TIME SPENT OF A T CELL IN THE SANCTUARY SITE

We use the following model to represent the probability of transitions between compartments i and j inside the sanctuary site in this way,

$$P_{i,j} = \frac{A_{i,j}}{\sum_k (A_{i,k})}, \tag{A.1}$$

where $A_{i,j}$ represents the surface area between the spherical layers i and j.

Then to compute the time of a T-cell inside the sanctuary we make a stochastic simulation initiating the T-cell in compartment 2. Then, we simulate each transition between compartments using equation A.1 until the T-cell enters to compartment 1. For each transition we normalize each time step by the diffusion rate $\frac{1}{D_{i,j}^{(y)}}$. We repeated the simulation $10,000$ times for diameters from 0.01mm to 1.25mm. The results of the time of T cell spent in sanctuary site for each site size is presented in figure A.1. The average time spent of a T cell according to this model would be 0.7446, 1.4900, 7.4806, and 15.0391 days when the sanctuary site diameter is 0.05, 0.1, 0.5 and 1 mm.

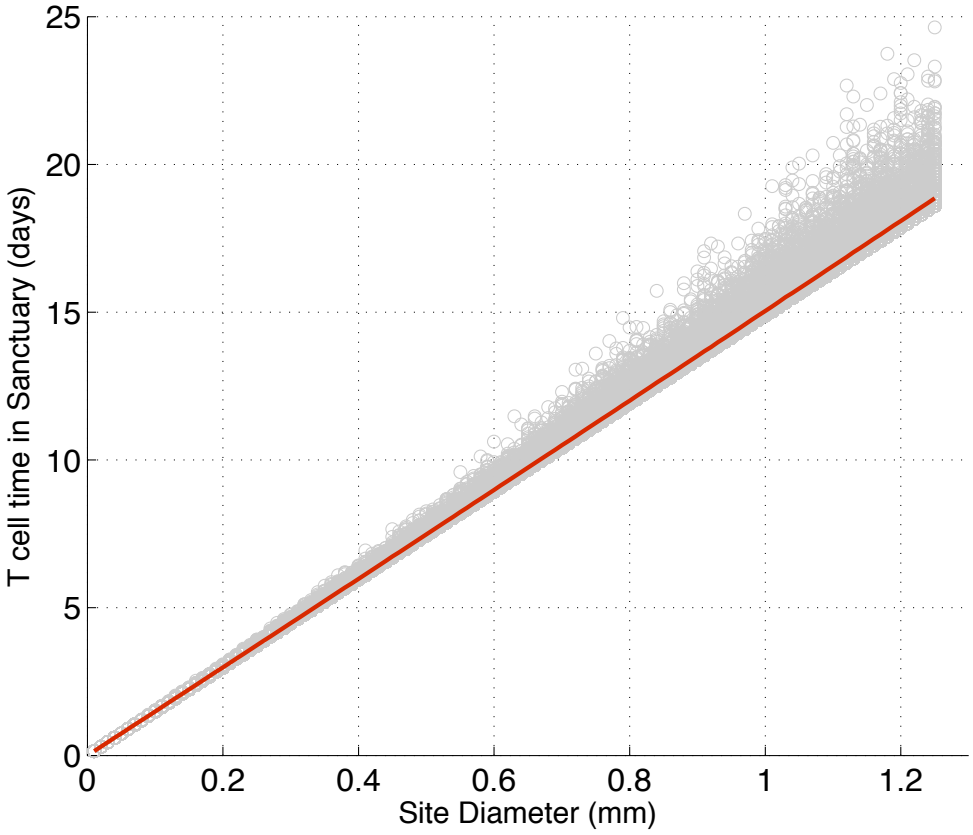

Figure A.1: Median time of T cell spent in sanctuary site vs Sanctuary site size (diameter). In red the median time for each diameter value. In blue, a scatter plot of the possible values of the T cell time in the site for each diameter value.

Appendix B

DISCLAIMER

This study uses data from a previously published study in the Journal of the Royal Society of Interface [47]. Given that the paper has Open Access rights, the use of figures and the 2-LTR patient-measurements, completely contained within the paper, is permitted according to the creative commons license [1].

[1] http://royalsocietypublishing.org/open-access-faqs
http://creativecommons.org/licenses/by/2.5/